Chem Soc Rev

Metal–Insulator–Semiconductor Photoelectrodes for Enhanced Photoelectrochemical Water Splitting

Complete List of Authors:	Ji, Li; Fudan University, State Key Laboratory of ASIC and System, School of Microelectronics Bard, Allen; University of Texas at Austin, Chemistry and Biochemistry; The University of Texas at Austin, Yu, E; The University of Texas at Austin, Department of Electrical and Computer Engineering Wei, Shice; Fudan University, School of Microelectronics Xia, Xuewen; Shanghai University Bi, Shuai; City University of Hong Kong Sun, Qing-Qing; Fudan University, Hu, Shen; Fudan University School of Microelectronics, Hsu, Hsien-Yi; City University of Hong Kong, School of Energy and Environment ; City University of Hong Kong, Department of Materials Science and Engineering Wu, Xuefeng; Fudan University, State Key Laboratory of ASIC and System, School of Microelectronics Zou, Xingli; Shanghai University, Materials Science and Engineering; The University of Texas at Austin, Chemistry Huang, Kai; Xiamen university, Fujian Key Laboratory of Semiconductor Materials and Applications Zhang, David; Fudan University, Microelectronics

SCHOLARONE™
Manuscripts

Metal–Insulator–Semiconductor Photoelectrodes for Enhanced Photoelectrochemical Water Splitting

Shice Wei,[a] Xuewen Xia,[b] Shuai Bi,[c] Shen Hu,[a] Xuefeng Wu,[a] Hsien-Yi HSU,[c] Xingli Zou,[b]* Kai Huang,[d]* David W. Zhang,[a] Qinqing Sun,[a] Allen J. Bard,[e†] Edward T. Yu,[e]* Li Ji[a]*

Photoelectrochemical (PEC) water splitting provides a scalable and integrated platform to harness renewable solar energy for green hydrogen production. The practical implementation of PEC systems hinges on addressing three critical challenges: enhancing energy conversion efficiency, ensuring long-term stability, and achieving economic viability. Metal-insulator-semiconductor (MIS) heterojunction photoelectrodes have gained significant attention over the last decade for their ability to efficiently segregate photogenerated carriers and mitigate corrosion-induced semiconductor degradation. This review discusses the structural composition and interfacial intricacies of MIS photoelectrodes tailored for PEC water splitting. The application of MIS heterostructures across various semiconductor light-absorbing layers, including traditional photovoltaic-grade semiconductors, metal oxides, and emerging materials, is presented first. Subsequently, the review elucidates the reaction mechanisms and respective merits of vacuum and non-vacuum deposition techniques in the fabrication of the insulator layer. In the context of the metal layer, the review extends beyond the conventional scope, not only by introducing metal-based cocatalysts but also by exploring the latest advancements in molecular and single-atom catalysts integrated within MIS photoelectrodes. Furthermore, a systematically summary of carrier-transfer mechanisms and interface design principles of MIS photoelectrodes are presented, which are pivotal for optimizing energy band alignment and enhancing solar-to-chemical conversion efficiency within the PEC system. Finally, this review explores innovative derivative configurations of MIS photoelectrodes, including back-illuminated MIS photoelectrodes, inverted MIS photoelectrodes, tandem MIS photoelectrodes, and monolithically integrated wireless MIS photoelectrodes. These novel architectures address the limitations of traditional MIS structures by effectively coupling different functional modules, minimizing optical and ohmic losses, and mitigating recombination losses.

1. Introduction

The advancement of human civilization is intrinsically linked to its utilization of energy. Despite remarkable progress in the development of electric vehicles, the escalating energy demand, coupled with a consumption pattern predominantly reliant on fossil fuels, continues to present substantial environmental challenges.[1-3] Artificial intelligence (AI) has been advancing rapidly and widely used in various fields in recent years, which has also raised the global energy demand. The computing resources required to develop and run AI models and applications could lead to a significant rise in the share of data centers in global electricity consumption.[4] Thus, in the context of the current discourse on climate change and energy crises, it is imperative to consider the burgeoning energy demands of AI within this broader framework. Developing sustainable, low-carbon energy technologies is crucial to mitigate the environmental impacts associated with the increased energy consumption necessitated by AI.[5,6] Concurrently, the rapid evolution of AI holds the potential to expedite advancements in the field of new energy sources, from material design to systemic performance enhancements, thereby significantly accelerating the development of low-carbon technologies. This dual approach not only addresses the immediate energy requirements of AI but also leverages AI's capabilities to foster innovation in sustainable energy solutions, contributing to a more resilient and environmentally friendly technological landscape. Developing renewable energy sources with high energy density is a pivotal solution to address the ongoing global energy crisis and environmental issues. Solar energy, possessing enormous potential, is delivered to the Earth's surface with an impressive energy magnitude of 1.7×10^5 TW. [7,8] Photovoltaic solar cell system is an important approach to utilizing solar energy, and it has entered a well commercialized stage globally. However, the intermittent and variable characteristics of rapidly growing renewable energy sources, such as solar and wind energy, pose significant

[a.] School of Microelectronics & Jiashan Fudan Institute, Fudan University, Shanghai 200433, China. E-mail: lji@fudan.edu.cn

[b.] State Key Laboratory of Advanced Special Steel & Shanghai Key Laboratory of Advanced Ferrometallurgy & School of Materials Science and Engineering, Shanghai University, Shanghai 200444, China. E-mail: xinglizou@shu.edu.cn

[c.] Department of Chemistry, City University of Hong Kong, 83 Tat Chee Avenue, Kowloon, Hong Kong 999077, China.

[d.] Department of Physics, Xiamen University, Xiamen 361005, China. Email: k_huang@xmu.edu.cn

[e.] Department of Electrical and Computer Engineering, The University of Texas at Austin, Texas 78758, United States. E-mail: ety@ece.utexas.edu

† Dr. Allen J. Bard passed away on Feb 11th, 2024.

challenges to the integration of renewable electric power into the utility grid.[9,10] Photoelectrochemical (PEC) water splitting offers an efficient approach for storing and transporting solar energy in the form of a high-density hydrogen fuel (140 MJ kg^{-1}). Furthermore, hydrogen serves as a key ingredient for synthesis of higher-value chemicals. The current commercial methods for hydrogen production and use were responsible for emission of over 900 million tons of CO_2, approximately 2.4% of total annual global carbon emissions in 2022, while the production of low-emission hydrogen constituted merely around 0.7% of the overall hydrogen production.[11] With the

emergence of novel hydrogen storage materials, such as carbon fibers and porous materials, the green hydrogen produced by renewable energy can be regarded as an excellent future energy option to provide energy to end-users through combustion in engines or electrochemical reactions in fuel cells, where water is the only by-product, thus realizing the change of energy structure from a carbon cycle to an environmentally friendly hydrogen cycle.

Since Honda and Fujishima's seminal demonstration of utilizing light energy in an electrochemical system of water with single crystal TiO_2 as a photoanode,[12] there has been extensive
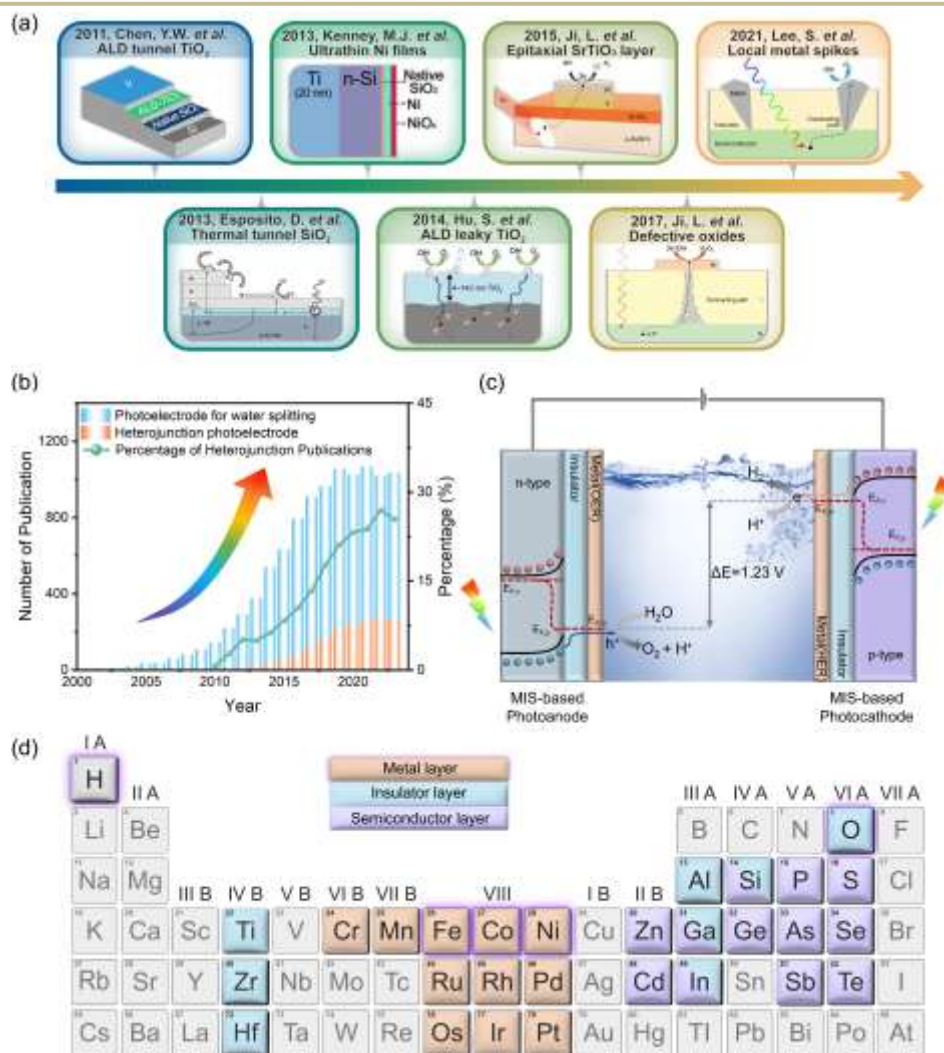

Fig. 1 (a) Brief roadmap of MIS photoelectrodes with different insulator layers and carrier-transfer mechanisms. "ALD tunnel TiO_2", reproduced from ref. 17 with permission from the Springer Nature, copyright 2011. "Thermal tunnel SiO_2", reproduced from ref. 19 with permission from the Springer Nature, copyright 2013. "Ultrathin Ni films", reproduced from ref. 20 with permission from the American Association for the Advancement of Science, copyright 2013. "ALD leaky TiO_2", reproduced from ref. 18 with permission from the American Association for the Advancement of Science, copyright 2014. "Epitaxial $SrTiO_3$ layer", reproduced from ref. 21 with permission from the Springer Nature, copyright 2014. "Defective oxides", reproduced from ref. 22 with permission from the Springer Nature, copyright 2016. "Local metal spikes", reproduced from ref. 23 under the terms of the CC-BY 4.0 license, copyright 2021, The Authors, published by the Springer Nature. (b) Publications related to the topics of "photoelectrode for water splitting" and "heterojunction photoelectrode for water splitting" since 2000 from the Web of Science Core Collection database. (c) Basic configurations and working mechanism of PEC water splitting system with MIS photoanode and photocathode. $E_{F,n}$ and $E_{F,p}$, quasi-Fermi level of semiconductor; $E_{F,m}$, Fermi level of the metal layer. (d) Component elements used to fabricate different functional layers of MIS photoelectrode.

research efforts devoted to the fields of photocatalysis and photoelectrocatalysis for converting solar energy into chemical energy. In a PEC system, photoelectrodes are stimulated by external light whereby photogenerated electrons and holes migrate under an electric field to the photocathode and photoanode surfaces, respectively, to participate in the electrochemical reduction and oxidation reactions. Compared with the photocatalytic system, the PEC system enables the spatial separation of the oxidation and reduction reactions, effectively inhibiting the reversible reactions, enhancing the energy conversion efficiency, and facilitating the separation of reaction products. However, issues such as low efficiency, poor stability, and high manufacturing costs impede its practical application. Techno-economic analyses of the PEC system indicate that achieving multiple quantitative performance metrics is necessary to attain a production cost of less than $1 per kilogram of hydrogen. These include a solar-to-hydrogen (STH) efficiency of the PEC configuration exceeding 10%, a working lifetime of the PEC system more than 10 years, and manufacturing cost per square meter less than $300.[13,14] To overcome these challenges, researchers have focused on developing multi-component systems that integrate different functional material layers into efficient and stable photoelectrodes. Metal-insulator-semiconductor (MIS) structures can enable highly effective strategies to enhance the overall performance of the PEC system with synergistic effects, especially for narrow bandgap semiconductors. In the 1970s, Green first proposed the use of tunnel metal-insulator-semiconductor diodes and explored this structure for developing efficient MIS solar cells.[15,16] In the early stage of the insulator development, most passivation layers utilized metal layers, metal silicide, doped silicon oxide, or oxide semiconductors deposited by chemical vapor deposition. However, due to technological limitations, these passivation layers were prone to a large number of pinholes and defects, leading to reduced photoelectrode transformation efficiency and stability. As depicted in Fig. 1a, advances in thin-film fabrication techniques, including atomic layer deposition (ALD),[17,18] thermal oxidation,[19] electron beam evaporation (EBE),[20] and molecular beam epitaxy (MBE),[21] along with an enhanced understanding of carrier-transport mechanisms,[17-23] have enabled the production of high-quality thin-film photoelectrodes, substantially bolstering the utility of MIS structures in PEC systems. Besides, continuous innovations in materials, such as organic semiconductors[24], molecular catalysts[25] and single-atom catalysts[26], as well as state-of-the-art characterization methods[27], including in-situ and transient photophysical techniques, have elevated both the photoelectrochemical energy conversion efficiency and mechanistic understanding of photoelectrodes. These advancements have contributed to the growing focus on various heterostructure strategies in the domain of PEC water splitting over the past decade (Fig. 1b). Existing literature reviews primarily focus on silicon-based MIS photoelectrodes or treat MIS heterostructures merely as a heterojunction engineering approach[1,28,29].

This review offers an exhaustive survey of strategies developed over the past decade to augment both the efficiency and stability of PEC systems through the incorporation of MIS heterostructures. The focus is on advancements in constituent materials, fabrication methodologies, interfacial regulation strategies, and carrier-transfer mechanisms for MIS photoelectrodes. Initially, the review delves into the triad of core elements crucial for MIS photoelectrode construction: semiconductor layers, insulator layers, and metal-based cocatalyst layers. The discussion primarily encompasses candidate materials, modification approaches, and fabrication processes. Subsequently, a comprehensive dissection of carrier-transfer mechanisms within MIS photoelectrodes is provided, interwoven with discussions on design principles for semiconductor/insulator and insulator/cocatalyst interfaces. Furthermore, this review summarizes innovative derivative configurations of MIS photoelectrodes. By optimizing device structures, enhancing interfacial properties, and improving system integration, these novel MIS photoelectrode designs have the potential to significantly increase the STH efficiency and reduce the overall cost of PEC water splitting systems, bringing this technology closer to industrial-scale implementation and accelerating the transition to a sustainable hydrogen economy. Finally, the review discusses the remaining challenges and provides insight into the prospective directions for MIS-based PEC systems.

2. Overview of metal–insulator–semiconductor photoelectrodes

The metal-semiconductor junction serves as a foundation for contemporary electronics and extends its utility to energy conversion devices.[30,31] The construction of metal-semiconductor heterojunction is a prevalent strategy for suppressing the recombination of photoexcited charge carriers.[32] However, the practical implementation of such devices, particularly in aqueous environments, is compromised by the issues of corrosion damage, oxidation, or other interfacial degradation, which hinder the development of photoelectrochemical systems with exceptional performance.[33] To address these challenges, an additional insulator layer can be introduced to construct an MIS photoelectrode. This approach not only eliminates the detrimental effects of surface states and avoid photoelectrodes failure caused by electrochemical corrosion but also garners significant research interest thank to the availability of facile and cost-effective preparation methods. The basic working mechanism of the MIS-based PEC water splitting system is illustrated in Fig. 1c. PEC water splitting capitalizes on the chemical potential differences between electrons in the electrolyte and those in the photoelectrodes at the solid-liquid junction. N-type semiconductors typically function as photoanodes, while p-type semiconductors serve as photocathodes. In this configuration, photogenerated electrons and holes migrate separately to the electrode surface, propelled by the electric field force within the space charge region.[34] To enhance the efficacy, stability, and feasibility of the

entire system, an integrated design of each component within the MIS photoelectrodes is essential. As shown in Fig. 1d, MIS photoelectrodes typically feature three functional layers: a metal layer comprising metal elements, oxides, and hydroxides (highlighted in orange); an insulator layer typically consisting of wide-bandgap metal oxides (Group IVB and IIIA) and/or SiO_x (highlighted in blue); and a semiconductor layer primarily comprising Group IV elements, as well as III-V and II-VI compound semiconductors (highlighted in purple). The complex interplay of three functional layers within MIS photoelectrodes underpins their growing importance in PEC water splitting. The following sections of this review will provide a comprehensive exploration of the latest advancements, challenges, and opportunities in the field.

3. Semiconductor layer of MIS photoelectrodes

The semiconductor serves as the driving force behind the PEC system, governing the effective conversion of light into chemical energy. The ideal photoabsorber should feature suitable band structures, outstanding electronic and optical properties, durability, and cost-effectiveness. However, optimizing these properties often involves inherent trade-offs. Consequently, extensive research has been directed towards the advancement of novel materials for solar energy harvesting, including traditional Si and III-V compound semiconductors, metal oxides, chalcogenides, nitrides, perovskites, and emerging polymer semiconductors.

3.1 Traditional photovoltaic (PV)-grade semiconductors

Traditional PV-grade semiconductors, such as Si and III–V compounds (GaAs, InP, $GaInP_2$, etc.), exhibit narrow band gaps and excellent charge transport properties, yielding relatively high STH efficiency and photocurrent density for PEC water splitting.[35-37] Silicon, the second most abundant element in the Earth's crust, has a 1.1-1.7 eV bandgap, varying with different crystallization conditions. Its tight lattice structure and small lattice constant (5.43 Å) are associated with strong covalent bonding between atoms (226 kJ mol^{-1}).[37] In addition, silicon can self-heal and anneal defects, such as vacancies and interstitials, through thermal treatments, evidenced by these defects with a high formation energy.[39,40] These unique electronic structures and crystal characteristics contribute to a low intrinsic defect density in silicon, making silicon favourable for photovoltaic applications.[41] However, the efforts to develop efficient and durable silicon-based photoelectrodes encounter several hurdles, including the indirect band gap of crystalline silicon, chemical instability under PEC operating conditions, inadequate light absorption in thin layers, and charge carrier recombination. To overcome these challenges, researchers have primarily focused on maximizing the absorption of energy from the solar spectrum, promoting carrier separation efficiency, accelerating interfacial charge transfer rates, particularly at the electrode and electrolyte interface, and improving electrode stability.[33]

Light absorption, the initial step in the PEC water splitting process, is the primary energy source for the production of photoexcited carriers. The relatively narrow bandgap of silicon enables it a broad absorption spectrum. However, silicon suffers from a reduced light absorption coefficient due to its indirect bandgap. This arises from the less probable phonon-assisted transitions compared to direct bandgap materials.[42] Furthermore, planar silicon-based photoelectrodes exhibit strong light reflection, resulting in a substantial loss of incident photons.[43] Therefore, surface and tandem configuration engineering have been conducted to enhance light harvesting. One of the most common methods for surface engineering is constructing surface textures on photoelectrodes, like wire, pyramid, and pillar arrays, as well as porous structures, which serve to reflect and scatter incident photons through multiple processes between the array structures. Moreover, the surface texturing strategy is capable of augmenting the effective reaction area and promoting the mass transfer and charge transport processes, thereby addressing the challenge of the use of low-purity Si and enhancing light absorption and, potentially, charge carrier collection.[44-46]

Chemical etching is a common top-down approach for the preparation of surface textures on crystalline Si-based photoelectrodes.[46-51] Zhang et al. fabricated a 3D p-Si/$NiCoSe_x$ core/shell nanopillar photocathode for hydrogen production, using p-type silicon substrate and reactive ion etching with a CsCl monolayer mask, bypassing expensive photolithography steps.[47] The nanopillars, averaging 200 nm in diameter and 1 µm in length, offer a greater specific surface area than planar Si, enhancing the diffusion of active substances and accelerating the overall reaction kinetics. A nickel-cobalt selenium shell film with excellent catalytic activity and optical transparency was synthesized through the process of photo-assisted chronoamperometry electrodeposition, resulting in uniform catalyst coverage on the 3D nanopillars and minimizing parasitic light absorption.[52] The p-Si/$NiCoSe_x$ nanopillar photocathode achieved a stable photocurrent density of 37.5 mA cm^{-2} at 0 V (vs. RHE) for solar-driven hydrogen generation. Although the fabrication of silicon micro/nanostructures by dry etching is relatively mature,[53,54] highly active reactive groups can introduce defects near the etched silicon surface, which could promote the recombination of charge carriers and result in lower open circuit voltage and conversion efficiency.[55,56] Metal-assisted chemical etching (MACE) is another chemical etching process that selectively etches silicon by employing metal catalysts. It has been widely studied in recent years due to several advantages: the high controllability of the etching process, relatively simple and cost-effective method that could be carried out without high vacuum equipment, and its ability to achieve high-quality silicon surface textures compared to dry etching.[56-58] As shown in Fig. 2a, Yu et al. successfully fabricated black silicon (b-Si) with a porous surface by the MACE method, which could simultaneously enhance light absorption and increase the electrochemically active surface area.[50] To mitigate problems associated with sluggish oxygen evolution kinetics and low electrochemical stability limits, an MIS photoanode b-Si/TiO_2/Co(OH)$_2$ was constructed via low-temperature atomic layer deposition to form a conformal TiO_2 film, followed by electrodeposition of a Co(OH)$_2$ catalytic film. The resulting

nanostructured Si photoanode exhibited significantly improved performance compared to the planar counterparts, revealing a saturated photocurrent density of 32.3 mA cm^{-2} at 1.48 V *vs.* RHE.

The vapor-liquid-solid (VLS) method is a bottom-up technique for the synthesis of silicon nanowires and other nanostructures. The Lewis group conducted a series of studies on the fabrication of silicon nanostructured photoelectrodes using the VLS method.[59-64] Boettcher *et al.* employed a copper-catalysed VLS process to produce an ordered silicon wire-array as photocathodes, achieving up to 3% energy-conversion

efficiencies in an aqueous methyl viologen^{2+} electrolyte.[59] They further boosted p-Si microwires performance via a radial n$^+$p homojunction, which increased photovoltage by enhancing band bending at the homojunction interface.[60] Nanostructured silicon photoelectrodes tend to degrade over time due to the high reaction surface area, particularly under water oxidation in alkaline electrolytes. The development of stable photoelectrodes is crucial for enabling long-term and continuous solar-driven fuel production, which is essential for practical applications. Shaner *et al.* addressed this by applying a TiO$_2$ protection layer and NiCrO$_x$ catalyst layer to Si microwire
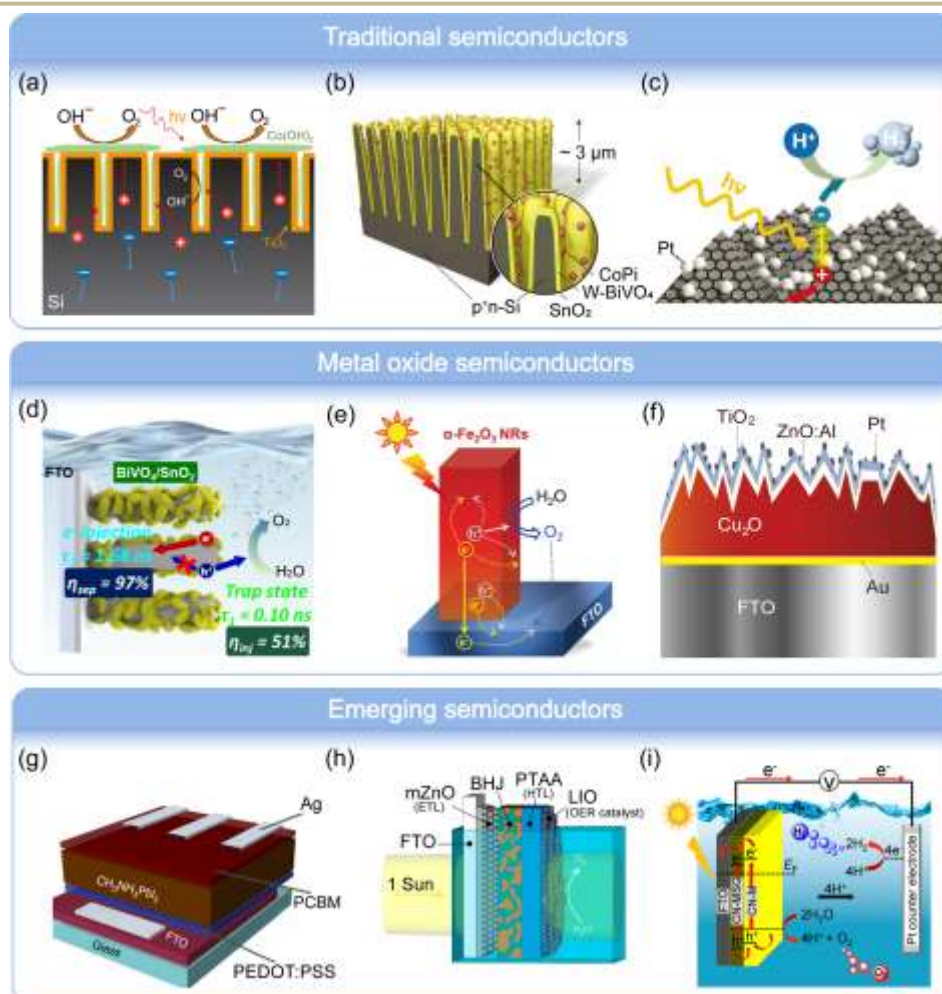

Fig. 2 Schematic illustration of the configuration of different semiconductor materials photoelectrodes. (a) The charge generation and oxygen evolution processes in the MIS photoanode b-Si/TiO$_2$/Co(OH)$_2$. Reproduced from ref. 50 with permission from the Springer Nature, copyright 2017. (b) The integrated tandem photoanode b-Si/SnO$_2$/BiVO$_4$/CoPi. Reproduced from ref. 74 with permission from the John Wiley and Sons, copyright 2017. (c) The 3D pyramid-shaped graphene/p-type silicon Schottky junction photocathode. Reproduced from ref. 48 with permission from the John Wiley and Sons, copyright 2019. (d) Schematics of charge carrier transfer of BiVO$_4$/SnO$_2$ heterostructure photoanode. Reproduced from ref. 96 with permission from the Elsevier, copyright 2021. (e) Schematic illustration of three main photogenerated carrier recombination pathways in hematite photoanodes. Reproduced from ref. 108 with permission from the John Wiley and Sons, copyright 2015. (f) Schematic diagrams of MIS-based Cu$_2$O/Al-ZnO/Ti$_2$O/Pt photocathode structure. Reproduced from ref. 113 with permission from the Springer Nature, copyright 2011. (g) The configuration of the inverted halide perovskite used for photocathode. Reproduced from ref. 123 under the terms of the CC-BY 4.0 license, copyright 2016, The Authors, published by the Springer Nature. (h) The donor–acceptor bulk heterojunction polymer semiconductor photoanode for solar water oxidation. Reproduced from ref. 129 with permission from the Springer Nature, copyright 2021. (i) The dual-layer carbon nitride heterostructure photoanode for PEC water oxidation. Reproduced from ref. 133 with permission from the American Chemical Society, copyright 2020.

arrays, yielding an MIS photoanode that functioned for over 2200 hours without significant degradation in 1.0 M KOH under one Sun illumination.[61] In addition to surface textures, various surface engineering strategies can be employed to enhance the performance and stability of Si-based photoelectrodes, such as surface plasmon resonance,[65-67] modified anti-reflection layers,[21,67] and surface functionalization with chemical groups.[69]

The photovoltage magnitude is directly proportional to the bandgap of the semiconductor material.[70] Silicon-based photoelectrodes encounter challenges in unbiased water splitting, due to the narrow bandgap of single crystal silicon (1.1 eV) and the significant reduction in effective photovoltage, approximately 0.6 eV, caused by free energy losses, kinetic losses, and shunt losses.[70-72] Tandem configurations engineering is a highly effective strategy for addressing the issue of low photovoltage in narrow bandgap photoelectrodes. This approach involves combining a silicon-based absorber layer with another semiconductor material to form a heterojunction, thereby reducing losses due to carrier relaxation and creating an additional built-in potential that promotes efficient generation and separation of charge carriers.[73] Theoretical models of dual-stacked absorber STH efficiency guide the selection of stacked materials with bandgaps around 2 eV, such as metal oxides and metal nitrides, as more optimal when paired with silicon. Chakthranont et al. designed an integrated tandem photoanode b-Si/SnO$_2$/BiVO$_4$/CoPi, as illustrated in Fig. 2b, to address the problem of low photovoltage of a pure Si photoelectrode and high surface defect densities of Si nanostructures.[74] The Si-BiVO$_4$ tandem nanostructures exhibit a synergistic effect by integrating the advantages of each component. Silicon acts as a conductive scaffold, providing excellent carrier transport characteristics, while the wide-bandgap BiVO$_4$ increases the overall photovoltage, resulting in an average STH efficiency of 0.45% without requiring an external bias and precious metals.

Efficient tandem heterojunctions require meticulous attention to atomic-scale interfaces and band alignment. In constructing tandem heterojunction photoelectrodes with bulk materials, surface states and band structures need to be considered, which restricts material selection. The distinctive electronic and structural properties of two-dimensional (2D) materials, distinct from their bulk counterparts, have prompted extensive investigation in electronics and energy fields.[75-77] The ability of 2D materials to form stacks without crystal mismatch and atomic interdiffusion through van der Waals interactions is of considerable interest for creating high-quality tandem heterojunctions with any substrates.[78,79] This approach enables the formation of various heterojunctions, such as Schottky junctions,[48] and p-n junctions,[80] efficiently suppressing charge recombination due to the absence of intrinsic surface states within their energy bandgap. Ultimately, this leads to an excellent tandem heterojunction photoelectrode with high carrier separation efficiency and extended charge lifetime. Ku et al. introduced a 3D pyramid-shaped graphene/p-type silicon Schottky junction photocathode, which demonstrated a significant improvement in light harvesting efficiency and

displayed encouraging performance for PEC hydrogen evolution (Fig. 2c).[48] Ethylene-vinyl acetate, instead of rigid PMMA, was employed to flexibly transfer graphene onto pyramid silicon to achieve intimate contact between graphene and pyramid silicon. The incorporation of graphene/Si Schottky heterojunctions shifted the onset potential positively by 120 mV, indicating improved charge separation efficiency. After Pt nanoparticle photodeposition, the photocathode showed an onset potential of 0.41 V and photocurrent of −32.5 mA cm^{-2} at 0 V (vs. RHE). Furthermore, the chemically inert graphene layer also acted as a protective layer,[78] resulting in the saturated current retaining 70% of its initial value even after 80 h of PEC H$_2$ evolution.

This section outlines key enhancement strategies for improving MIS photoelectrodes made from traditional PV-grade semiconductors, such as surface and tandem nanostructure engineering. At present, fabricating traditional semiconductors typically necessitates intricate purification processes and considerable electrical energy for carbothermal reduction reactions.[81] Therefore, developing eco-friendly and cost-efficient purification techniques holds substantial importance for the practical implementation of photoelectrodes based on traditional PV-grade semiconductors.

3.2 Metal oxide semiconductors

Metal oxides have emerged as promising photoelectrode materials for PEC water splitting due to their tunable optoelectronic properties,[82] earth abundance, low-cost production, and versatile preparation methods.[34] While they suffer from low intrinsic carrier mobility, metal oxides exhibit excellent long-term stability and encouraging efficiency for PEC water splitting. Furthermore, their varied bandgap range further enables diverse options for designing tandem photoelectrodes, advancing high-performance MIS-based PEC systems.

Monoclinic scheelite bismuth vanadate (BiVO$_4$) stands out among metal oxide photoanodes due to its proper band edge position for H$_2$O oxidation, chemical stability, and facile preparation method.[83] The high electronegativity of oxygen in BiVO$_4$ confers resistance to chemical and photo oxidation by reducing the tendency of donating electrons. Its moderate bandgap is important in enabling high PEC water-splitting efficiency. In contrast to TiO$_2$ and WO$_3$ which have wide bandgaps and limited light absorption due to their empty d-orbitals, the valence band (VB) of monoclinic scheelite BiVO$_4$ is primarily composed of the hybridization of Bi 6s and O 2p orbitals, resulting in the upward shift of VB with the contribution of high energy orbitals.[83-85] The theoretical maximum photocurrent density of BiVO$_4$ under Air Mass (AM) 1.5 G illumination (100 mW cm^{-2}) is 7.5 mA cm^{-2}, corresponding to a theoretical limit for solar-to-hydrogen (STH) efficiency of 9.2%.[84] However, bare BiVO$_4$ photoanodes underperform relative to the theoretical limit due to challenges like low charge carrier mobility, high carrier recombination rate, and sluggish kinetics of water oxidation. The electron and hole mobility in BiVO$_4$, with values ranging from 0.02-12 cm^2 V^{-1} s^{-1} and around 2 cm^2 V^{-1} s^{-1}, respectively, are considerably lower than those of

conventional semiconductors, which is attributed to the polaron hopping conduction mechanism that controls charge carrier transport in $BiVO_4$.[86-88] Uemura *et al.* employed transient X-ray absorption fine structure spectroscopy to examine photocarrier transitions in $BiVO_4$, revealing a photoexcited state lifetime of 40 ± 15 ns, derived from a roughly 100 ns relaxation process .[89] The limited carrier mobility and short photocarrier lifetime on the order of nanoseconds result in a relatively short hole diffusion length of approximately 70 nm in $BiVO_4$,[90] which greatly hinders the transport and utilization of photogenerated carriers. Hence, several strategies are typically employed in combination to address these challenges, including nanostructuring,[91] dopant incorporation,[92] heterostructuring,[93] and integration of oxygen evolution cocatalysts.[94] Such multifaceted approaches aim to optimize the photoanodic performance of $BiVO_4$ and bring it progressively closer to its theoretical limit.[95] Fig. 2d illustrates that Yang *et al.* engineered a multicomponent heterostructure photoanode, synthesizing $BiVO_4$ electrochemically and coating it uniformly on host scaffolds of SnO_2 nanorod arrays known for superior carrier transport.[96] This integration created a staggered type II heterostructure that could minimize charge recombination and demonstrate a high carrier separation efficiency of up to 97%. Manipulating the electrochemical deposition time of $BiVO_4$ allows for the design of a hierarchical photoelectrode with nanopores and mesopores, which could facilitate rapid mass transfer while increasing the reaction area.[97] In order to enhance the interfacial hole transfer efficiency, authors incorporated NiFe oxygen evolution cocatalyst into the PEC system. When paired with a perovskite/Si solar cell, this $NiFe/BiVO_4/SnO_2$ photoanode in a PEC-PV tandem cell achieved an operating photocurrent density of 5.90 mA cm^{-2} and a STH efficiency of 7.3% at zero-bias. The stability of $BiVO_4$ during PEC measurements is notably influenced by electrolyte pH. Previous studies have examined $BiVO_4$ photoanodes under neutral conditions, as $BiVO_4$ tends to dissolve when exposed to highly acidic or basic environments.[98] The thermodynamic oxidation and reduction potentials of various semiconductors guide material stability assessments during photocatalytic water splitting.[99] Under extreme electrolyte conditions with pH=0, the calculated oxidation potential of $BiVO_4$ approximates that of water, underscoring the need for stability in harsh environments. MIS-based $BiVO_4$ photoanodes prevent direct contact between $BiVO_4$ and electrolyte while improving the carriers' separation and injection efficiency, thereby mitigating the self-oxidation caused by hole accumulation.[100-102] Qin *et al.* developed an MIS-based $BiVO_4$ device integrated with a 5 nm TiO_2 protection layer and Ni cocatalyst, achieving high stability in alkaline PEC conditions.[103] Incorporating graphene between the TiO_2 and Ni layers improved hole extraction, resulting in over 30 hours of stability in a pH 13 basic electrolyte under extended illumination.

Hematite (α-Fe_2O_3) serves as another promising photoanode candidate owing to its natural abundance, non-toxicity, and stability in alkaline electrolytes. Its 2.1 eV bandgap allows for broader visible light absorption, resulting in a higher theoretical STH efficiency of 15% compared to $BiVO_4$.[104]

However, its limited efficiency of water oxidation is attributed to a short hole diffusion length (2-4 nm) arising from ultrafast recombination of photocarriers and poor minority charge mobility.[105] The rapid carrier recombination process in α-Fe_2O_3 photoelectrodes results in energy loss, which occurs through surface, bulk, and α-Fe_2O_3/substrate interface pathways, as indicated in Fig. 2e.[106-108] Various strategies, such as the construction of nanostructures, doping, surface passivation, and loading a catalyst layer, are researched to inhibit carrier recombination in α-Fe_2O_3 photoelectrodes.[105] Cho *et al.* adopted multiple strategies simultaneously to weaken all three recombination pathways in hematite nanorods photoanode.[108] The strategy involved flame-doping Ti, dense-layer deposition, removing the disorder layer, and electrocatalyst deposition, reducing the onset potential to 0.64 V (*vs.* RHE).

Copper-based semiconductors, specifically copper oxides, have gained attention for their potential as p-type oxides in the PEC hydrogen evolution. These materials possess favourable characteristics for PEC applications, such as photoactivity, abundance of copper, and feasibility of processing through cost-effective and established methods like electrodeposition.[109] Cuprous oxide (Cu_2O) has been widely investigated in photocathodes for PEC water splitting, because of its suitable conductive band position and relative narrow bandgap of 2.0 eV derived from the participation of Cu 3d levels.[110,111] However, its susceptibility to photocorrosion during PEC operation poses a significant challenge. Although the cathodic decomposition reaction of Cu_2O ($E_{(Cu+/Cu)}$=0.47 V *vs* normal hydrogen electrode (NHE)) is thermodynamically more favourable than the reduction reaction of water, various strategies can be adopted to kinetically hinder the photocorrosion rate of Cu_2O.[111,112] Paracchino *et al.* addressed the chemical instability in Cu_2O photocathodes by depositing conformally multiple passivation layers by ALD technology.[113] The photocathode structure, as shown in Fig. 2f, included an Al-doped ZnO buffer layer and a TiO_2 insulator layer to avoid direct contact with the electrolyte and create a staggered type-II band bending for efficient charge carrier separation. The optimized $Cu_2O/Al-ZnO/Ti_2O/Pt$ photocathode achieved a 7.6 mA cm^{-2} photocurrent (at 0 V *vs.* RHE) and sustained stability over an hour, outperforming a bare Cu_2O photocathode, which degraded within a minute. Additionally, long-term light exposure was found to reduce the amorphous TiO_2 protection layer to Ti^{3+} traps, leading to a gradual decline of photocurrent. To combat this, Paracchino *et al.* optimized the growth temperature of TiO_2 and performed post-annealing to promote TiO_2 crystallization. This led to achieving the electron depletion layers at the TiO_2–electrolyte interfaces which effectively suppressed the parasitic side reaction of TiO_2 reduction.[114] As a result, the stability of the Cu_2O photocathode was significantly enhanced, which resulted in the photocurrent remaining at 62% of its initial value even after ten hours of testing. In light of the above-mentioned three exemplary metal oxides, metal oxide semiconductors constitute a diverse class of candidate materials for photoelectrodes. To address certain inherent limitations of metal oxides, such as low carrier mobility, the integration of multiple strategies to construct MIS photoelectrodes offers a promising solution.

ARTICLE

Favourable band alignment of the overall structure and the electrical properties of the protective layer have a significant impact on the charge transfer efficiency and the stability of the MIS photoelectrodes.

3.3 Emerging semiconductors

In recent years, advances in materials science have yielded novel semiconductor light-absorbing layer materials, such as hybrid perovskites, linear polymer semiconductors, and two-dimensional polymers like g-C$_3$N$_4$. These emerging materials offer unique advantages, such as tunable bandgaps, structural diversity, and economical preparation methods. Here, we summarize the key advancements and challenges in applying these emerging semiconductors for PEC water splitting.

Halide organic-inorganic hybrid perovskites have attracted significant attention in the field of solar cells since Miyasaka *et al.* first used them as sensitizers in photovoltaic cells.[115] In the past decade, hybrid perovskite solar cells have undergone rapid development and their energy conversion efficiency has skyrocketed from 14.1% to over 25%.[116-118] This rapid progress can be attributed to their superior optical and electrical properties, such as high absorption coefficient, excellent carrier mobility, and long carrier diffusion lengths. The large-area preparation by solution method, which can be low-cost and scalable, further cements their utility in photovoltaic applications. Hybrid perovskites also show promise in solar fuel generation via PEC systems, but stability remains a hurdle due to the hydrolysis of organic cations, which degrades both the crystal structure and electronic properties.[119,120] Traditional solutions often employ a configuration of perovskite photovoltaic-electrocatalytic (PV-EC) cell, isolating the perovskite from the electrolyte and connecting it to an external electrolyzer.[121] An alternative facile approach is to integrate perovskites with the electrocatalyst on a single photoelectrode, where perovskites are encapsulated by a protection layer, such as metal layers, metal oxides, or carbon-based materials.[122-125] The latter integration strategy, reminiscent of the MIS structure, requires a high-quality encapsulation layer, as perovskites are highly sensitive to moisture. Da *et al.* developed a CH$_3$NH$_3$PbI$_3$-based photoanode with an ultrathin Ni layer, serving dual roles as a passivation layer and an oxidation reaction catalyst.[122] The photocurrent density for the oxidation of Na$_2$S remained consistent at over 2 mA cm^{-2} even after 15 minutes of continuous testing. Quesada *et al.* reported a novel approach to protecting the inverted halide perovskite configuration (as shown in Fig. 2g) by employing Field's metal (InBiSn alloy) to encapsulate it onto the silver electrode.[123] This innovative encapsulation technique is expected to shield the perovskite from the electrolyte and facilitate electron transport for hydrogen production at platinum sites. The InBiSn-encapsulated perovskite photocathode exhibited an average photocurrent density of 6.9±1.8 mA cm^{-2} (at 0 V *vs.* RHE) that could sustain at 80% of its initial value for over 1.5 hours while undergoing testing under chopped light mode. Furthermore, the InBiSn encapsulated layer could be conveniently removed from deteriorated photocathodes and effectively recycled for repeated usage. The straightforward and recyclable benefits of

this approach present a new avenue for fabricating photoelectrodes based on perovskites and other unstable semiconductors.

Polymer semiconductors are increasingly used in various optoelectronic devices, such as organic solar cells,[126] organic light-emitting diodes,[127] and photodetectors.[128] The development of polymer-based photoelectrodes is an attractive approach for developing scalable PEC devices owing to the simplicity and cost-effectiveness of their synthesis in a moderate environment.[24] Besides, polymer semiconductors allow precise tuning of optoelectronic properties and energy band structure through straightforward structural design or post-modifications, which is comparatively simpler than the traditional element doping methods. However, the efficiency of polymer-based devices is constrained by their low charge separation efficiency and mobility, which arise from the low rate of exciton dissociation and the carrier transport mechanism of intramolecular delocalization and intermolecular hopping. To overcome these limitations, Cho *et al.* employed a donor-acceptor bulk heterojunction approach, commonly used in organic solar cells, to enhance the performance of a polymer semiconductor photoanode for solar water oxidation.[129,130] As shown in Fig. 2h, the polymer-based MIS photoanode is composed of bulk heterojunction polymer, an electron transport layer of mesoporous zinc oxide, a hole transport layer of poly(triarylamine), and modified iridium oxide as the water oxidation catalyst.[129] This assembly achieved an excellent photocurrent value up to 2.3 mA cm^{-2} at 1.23 V (*vs.* RHE), with an incident photon-to-current efficiency (IPCE) of greater than 25%. The carrier transport layer facilitates the transfer of photogenerated carriers, reducing the accumulation of carriers at the interface and preventing degradation of the polymer absorber, which could improve the stability of the polymer-based photoanode.

Conventional linear polymer semiconductors possess weak chain interactions, hindering carrier separation and transport between chain segments. However, expanding the structural dimension of conjugated polymers from one-dimensional to two-dimensional enhances the degree of conjugation of π electrons, leading to superior optoelectronic properties. Recently, a new class of two-dimensional conjugated polymers, such as graphitic carbon nitride (g-C$_3$N$_4$) and covalent organic frameworks (COFs),[131,132] has been increasingly utilized in energy conversion and electronic devices. Karjule *et al.* employed graphene as a template to promote the formation of ordered carbon nitride, thereby addressing the issue of rapid carrier recombination.[133] They also fabricated a dual-layer carbon nitride heterostructure through a vapor deposition technique to enhance the carrier separation (Fig. 2i). The majority of emerging two-dimensional conjugated polymers are synthesized using solvothermal methods to get insoluble powder samples that are difficult to be processed as films. Therefore, the preparation of photoelectrode often relies on drop coating or doctor blade methods with polymer suspension solution, both of which yield suboptimal films. It is imperative to develop high-quality thin film preparation techniques to further expand the applications of these novel semiconductors.
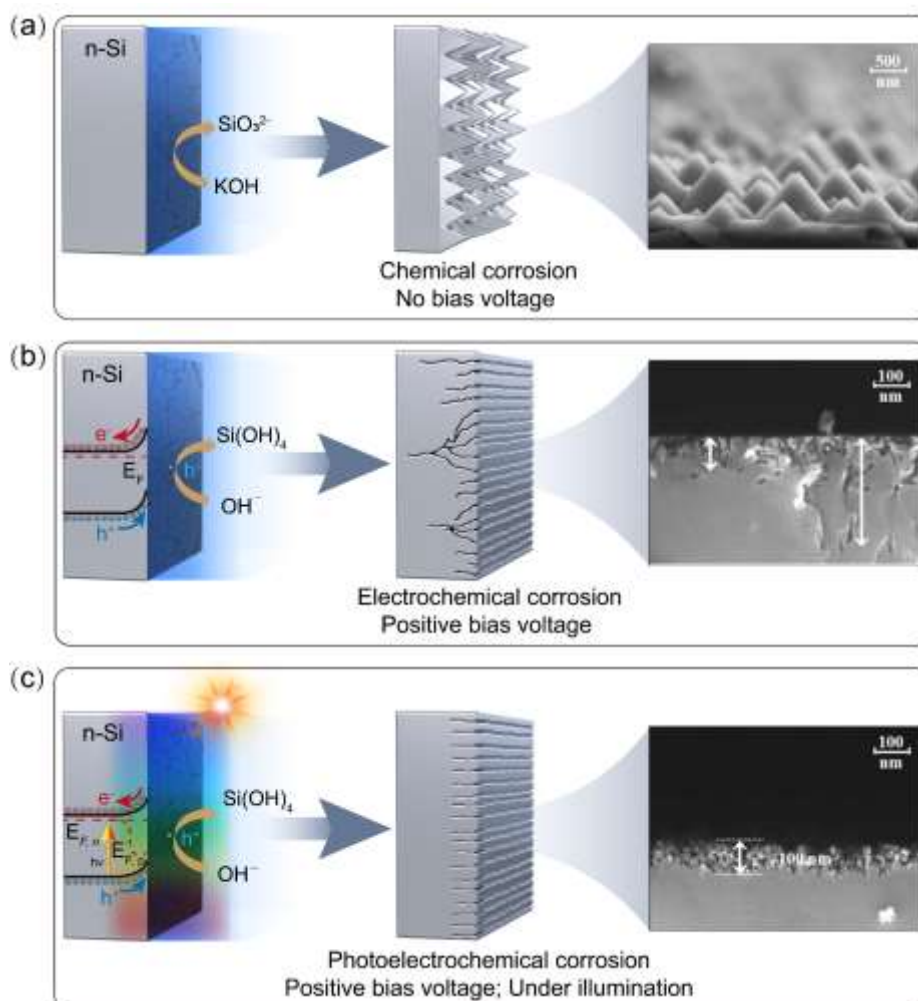
Fig. 3 Schematic illustration of corrosion process of n-Si photoanode for PEC water splitting in KOH electrolyte. (a) Chemical corrosion of silicon reacting with KOH leads to the formation of micro-pyramidal surface morphology. (b) Electrochemical corrosion of anodic current to oxidize electrodes leads to the formation of nanostructured silicon. (c) Photoelectrochemical corrosion of photogenerated holes to oxidize electrodes leads to the formation of nanostructured silicon within the light penetration depth. SEM images are reproduced from ref. 138 with permission from the Royal Society of Chemistry, copyright 2022.

Several advanced techniques have shown promise in the preparation of high-quality 2D conjugated polymer thin films, including interfacial growth, solvothermal in-situ growth, and electrophoretic deposition.[134,135] Despite these developments, significant challenges remain in designing high-performance two-dimensional conjugated polymer devices, from structure design to thin film preparation to device structure design.

Semiconductor light-absorbing materials serve as the linchpin in MIS photoelectrodes, tasked with photon-to-carrier conversion in PEC reactions. This section focuses on semiconductors integrated into MIS photoelectrodes, ranging from traditional PV-grade materials and metal oxides to emerging semiconductors. The overarching development goals for these semiconductor layers are superior electronic and optical properties, stability, and carrier separation efficiency. Advances in high-throughput computational screening and automated experimental platforms are set to expedite the development of high-performance semiconductor materials.

4. Insulator layer of MIS photoelectrodes

4.1 Corrosion mechanisms and protection strategies

As mentioned in the introduction, to achieve large-scale practical implementation of PEC water splitting, the PEC devices need to exhibit an operational life exceeding ten years,[13] which places high demands on the stability of the system. The long-term stability of the PEC system is contingent on the robustness of each component in the system, but photoelectrodes play a critical role in the short-term stability of the system.[112] Therefore, it is imperative to gain a comprehensive understanding of the photoelectrode corrosion mechanisms. Typically, strong acids or bases are commonly employed as electrolytes due to their high ionization and good conductivity, which promote efficient electron transfer and mass transfer to accelerate the reaction kinetics and enhance the PEC performance. However, the corrosive nature of the electrolyte
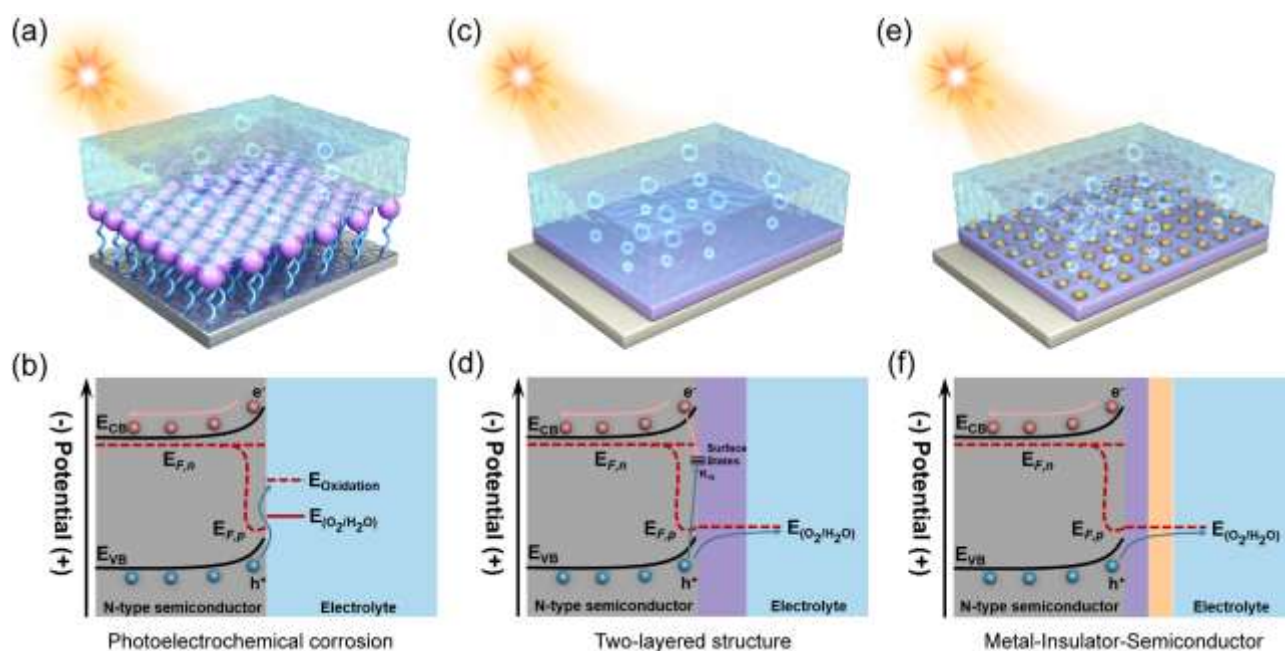
Fig. 4 Schematic illustration of various protection strategies and energy band structures. (a) Surface functionalization with electroactive reagents. (b) Energy band structure of photoelectrochemical corrosion in N-type semiconductor. (c) Two-layered structure protection strategy. (d) Energy band structure of two-layered photoelectrode for PEC oxygen evolution. (e) Three-layered structure protection strategy of metal-insulator-semiconductor configuration. (f) Energy band structure of metal-insulator-semiconductor photoelectrode for PEC oxygen evolution.

can lead to significant electrode degradation and limit the durability of the PEC system, especially for the narrow bandgap semiconductors. The corrosion reaction of the photoelectrode in PEC water splitting is a complex process, which is influenced by factors such as material composition, electrolyte pH, temperature, light intensity, and applied potentials.[136] As illustrated in Fig. 3, taking n-Si photoanode in KOH electrolyte as an example, the overall corrosion process of the photoelectrode can be categorized into three distinct phases: chemical, electrochemical, and photoelectrochemical corrosions. In the chemical corrosion (Fig. 3a), silicon is oxidized to SiO_2, leading to soluble silicate anions and forming a micro-pyramidal surface due to varied atomic densities in different crystal plane orientations.[137] In electrochemical corrosion (Fig. 3b), holes migrate to the electrode surface, driven by the local electric field in the space charge region and the external power. The sluggish kinetics of water oxidation can lead to the accumulation of holes at the electrode surface, ultimately resulting in the degradation of the lattice structure of photoelectrode and consequent corrosion. Photoelectrochemical corrosion follows a similar mechanism to electrochemical corrosion, albeit with a key difference that the corrosion region is limited to the light penetration depth (Fig. 3c).[138]

Various protection strategies have been developed to stabilize photoelectrodes due to the prevalence of corrosion reactions. These electrode protection strategies should be formulated based on two fundamental design principles: (1) selecting electrode materials with inherent thermodynamic stability based on the Pourbaix diagram or isolating electrodes

from direct electrolyte contact to minimize chemical corrosion; and (2) designing appropriate electrode configurations for enhanced carrier separation and transport, thereby fostering the desired redox reactions and reducing carrier recombination and surface accumulation, finally providing kinetic protection instead of corrosion reaction. Surface functionalization with electroactive reagents has emerged as an effective means to create high-quality functional interfaces that can effectively mitigate corrosion reactions and manipulate the interfacial energetic band (Fig. 4a).[139-141] The immobilization of electroactive molecules onto silicon surfaces is commonly achieved through the hydrosilylation reaction, which forms interfacial Si–C covalent bonds. The resulting densely packed monolayers serve as a protective layer that inhibits corrosion reactions, especially when the oxidation potential of the semiconductor is more negative than the water oxidation potential (Fig. 4b). The interfacial electrical properties and stability of the semiconductor-solution junction are largely determined by the properties of the monolayers, particularly the packing density and types of terminal electroactive groups. However, incomplete coverage and molecular chain flexibility present challenges to the formation of a long-term stable PEC system, as they may allow reactive species to degrade the photoelectrodes. The two-layered structure protection strategy is another popular approach to bolstering photoelectrode stability (Fig. 4c). A thin metal or metal oxide layer is deposited on the semiconductor photoelectrode, forming a protective layer against corrosion and degradation in harsh electrolyte environments. In addition to serving as a physical isolation layer to suppress corrosion, the deposited layer can also serve

multiple functions such as constructing a heterostructure with the underlying semiconductor layer to improve carrier separation efficiency and reducing the activation energy of water splitting as a cocatalyst layer. The two-layered strategy has been extensively investigated and reviewed, leading to the development of various derivative strategies including core-shell and host-guest structures.[29,84,142] Nonetheless, the formation of barrier states or defect states in the interface region of the two layers may lead to the Fermi-level pinning effect which could render various tuning strategies ineffective and reduce the built-in voltage (Fig. 4d).[143] The advancement of vacuum thin film preparation technology has facilitated the adoption of MIS photoelectrodes, as a derivative strategy of the two-layered electrode, for PEC water splitting (Fig. 4e). The introduction of an insulator layer can effectively passivate the surface states to solve the Fermi-level pinning problem (Fig. 4f). The MIS approach also decouples protective layer stability from catalytic activity, providing versatility in barrier height adjustment using metals with varied work functions.

4.2 Materials for the insulator layer

The insulator layer is a crucial component in MIS-based photoelectrodes, playing a dual role in protecting the photoelectrodes from corrosive reactions and facilitating efficient transport of minority carriers through the MIS heterojunction. Thus, the material selection and property optimization for the insulator layer are key factors in achieving excellent photoelectrode performance. The ideal insulator layer should meet the following criteria: exceptional thermodynamic and kinetic stability to ensure prolonged working life; optical transparency to minimize parasitic light absorption; and adjustable electronic properties as well as energy band structure to facilitate photogenerated carriers' separation. As illustrated in Fig. 1d, commonly employed insulator layers for MIS photoelectrodes include wide-bandgap metal oxides, such as group IV B metal oxides (e.g., TiO_x, ZrO_x, HfO_x) and group III A metal oxides (e.g., AlO_x, GaO_x, InO_x), as well as SiO_x.[144,145]

SiO_2 is commonly used as an insulator layer in Si-based photoelectrodes due to its favourable thermodynamic stability across a broad range of pH and potentials and the exceptional electronic quality of the Si/SiO_2 interface. However, the spontaneous formation of SiO_2 is often uncontrollable, and its large charge transfer resistance can significantly compromise the performance of silicon-based photoelectrodes. Esposito *et al.* utilized a 2 nm SiO_2 layer as the insulator layer, prepared by rapid thermal oxidation (RTO), improving fill factor and open circuit voltage due to fewer interfacial defects.[19] Furthermore, the superior interface quality suppressed carrier recombination behavior, resulting in an increase in the effective diffusion length of electrons from 12 μm to 82 μm. Despite these promising results, the SiO_2 insulator layer still faces challenges such as lower photocurrent density and instability under strong alkaline conditions.

Alternatively, TiO_2 also serves as a well-studied insulator layer, especially compatible with narrow bandgap semiconductors. TiO_2 is an intrinsically n-type semiconductor due to oxygen vacancies in the TiO_2 lattice, making it suitable as

an insulator protective layer for p-type semiconductors.[146] Its conduction band alignment with many photoabsorber layers promotes efficient electron transport. Moreover, an additional electric field for efficient carrier separation can be constructed by forming a p-n heterojunction with a p-type semiconductor layer. Ros et al. employed fully crystallized TiO_2 to create long-term stable Si-based photocathodes that functioned continuously for 300 hours in 0.5 M H_2SO_4.[147] The intrinsic TiO_2 typically exhibits barrier properties for hole transport due to significant valence band energy offsets between TiO_2 and many traditional semiconductor layers. However, its electronic properties can be engineered to facilitate hole transport, as demonstrated by tunnelling or intermediate band formation mechanisms.[145,148] Chen *et al.* first utilized ALD technology to prepare a pinhole-free TiO_2 insulator layer for MIS photoelectrode.[17] The ALD-grown TiO_2 protected the underlying semiconductor layer from corrosive reactions while also enabling facile hole tunnelling through the ultrathin TiO_2 layer (2 nm), contributing to 8-hour operational stability in 1 M KOH electrolyte. In contrast, photoelectrodes lacking this TiO_2 layer failed within 0.5 hours. This pioneering work underscores the potential of ALD technology for advancing MIS photoelectrode performance.

HfO_2 and ZrO_2, belonging to the same group as titanium, excel as passivation layers in solar cells and gate dielectric due to their high refractive index and high dielectric constants. Furthermore, mature ALD preparation technology, superior passivation effect compared to TiO_2, and excellent corrosion resistance make them suitable as insulator layers in MIS photoelectrodes even in harsh electrolytes.[149-151] However, their wide bandgap (5.0-5.8 eV) results in a larger energy barrier for carrier transport at the semiconductor/insulator interface, potentially reducing the conversion efficiency of PEC system. Quinn et al. utilized ALD technology to deposit highly uniform and thickness-controllable HfO_2 thin films for fabricating $Ni/HfO_2/Si$ MIS photoanodes.[150] The incorporation of high-quality HfO_2 films not only serves as a chemical passivation layer, effectively enhancing the stability of silicon-based photoanodes during water oxidation, but also addresses the issue of metal catalytic layers with a low work function that restrict the photovoltage generated in the photoanode system through field-effect passivation. Similarly, the group III A metal oxides, such as Al_2O_3, Ga_2O_3, and In_2O_3, are increasingly utilized as insulator layers due to their high dielectric constants, excellent stability, and substrate compatibility.[152-154]

Although wide-bandgap metal oxides remain the predominant candidate materials for the insulator layers in MIS photoelectrodes, the preparation of high-quality and pinhole-free metal oxide insulator layers typically necessitates high-vacuum equipment in ultra-clean laboratory, inevitably increasing the manufacturing cost of MIS photoelectrodes. Additionally, under some extreme testing conditions, such as high negative bias or strong ultraviolet irradiation, the robustness of metal oxide protective layers may diminish. Therefore, the investigation of cost-efficient and versatile insulator layers is meaningful. During the 1980s, a surge of interest emerged around conductive polymers such as
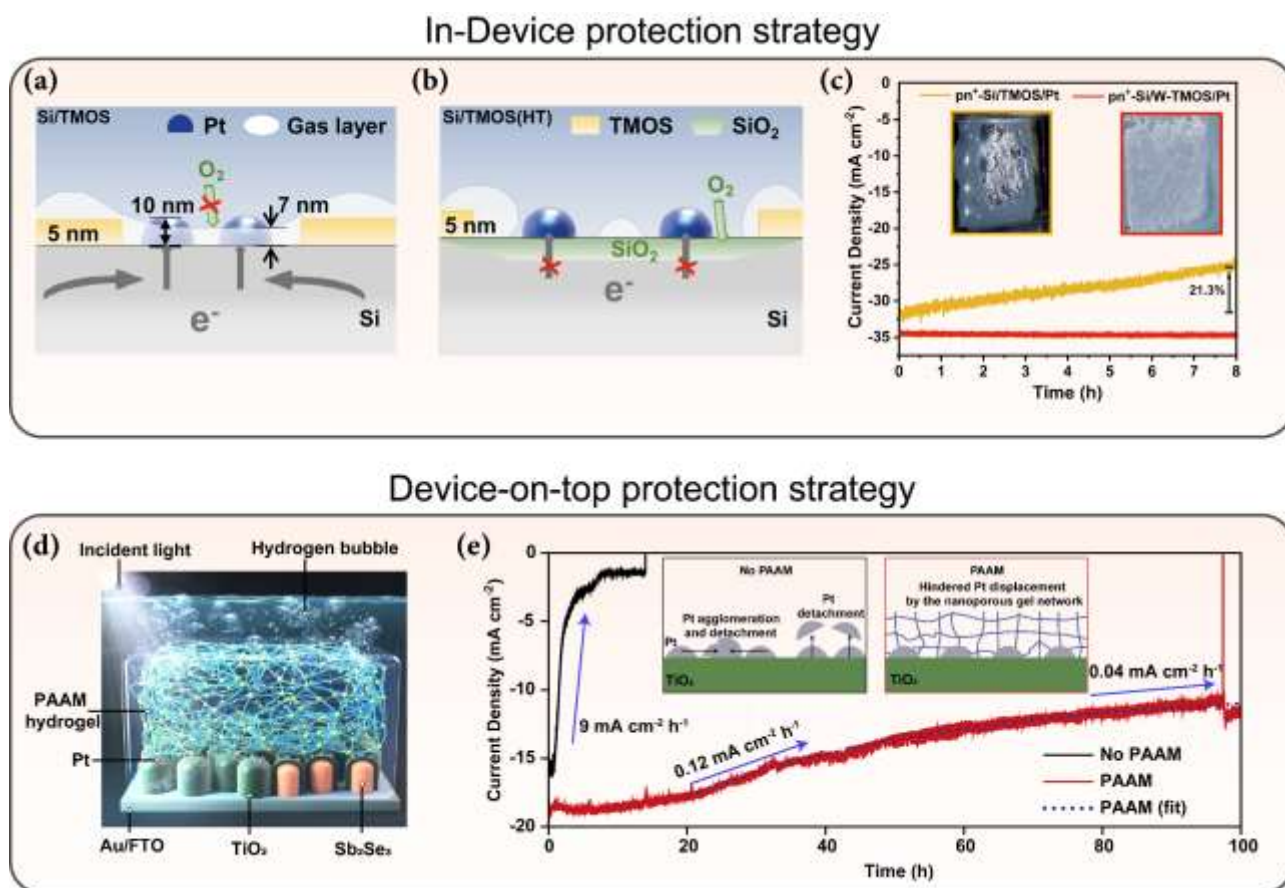
In-Device protection strategy

Device-on-top protection strategy

Fig. 5 Novel organic material-based insulator layers for MIS Photoelectrodes. Schematic illustrations of the protective mechanism of organic protective layers with different pore sizes for (a) Si/TMOS, (b) Si/TMOS (HT); (c) Photocurrent stability test of pn[+]-Si/TMOS/Pt and pn[+]-Si/W-TMOS/Pt at 0 V *vs.* RHE. (Inset: Photograph of the MIS photoelectrode during the stability test.) Reproduced from ref. 162 under the terms of the CC-BY 4.0 license, copyright 2022, The Authors, published by the Springer Nature. (d) Schematic of a PAAM hydrogel-protected MIS photocathode for PEC water splitting; (e) Photocurrent stability test with and without PAAM hydrogel-protected photoelectrode. (Inset: Schematic diagram of the confinement effect of hydrogel nanopore network on Pt particles). Reproduced from ref. 164 with permission from the Springer Nature, copyright 2022.

polypyrrole, polyacetylene, polythiophene, and polyaniline due to their straightforward electrochemical polymerization, which facilitates seamless integration onto substrates.[155-158] However, photoelectrodes encapsulated with these organic films often manifest diminished photocurrent densities. This is attributed to the formation of large gas bubbles that envelop active sites, disrupt interface contact, and potentially cause film delamination.[159,160] Additionally, the accumulation of these bubbles during gas-evolving reactions impedes the effective transfer of photogenerated charges and mass exchange between the photoelectrode and the electrolyte.[161] Consequently, fabricating tunable organic insulator layers for MIS photoelectrodes to mitigate the detrimental effects of bubble formation and ultimately achieve stable and efficient photoelectrochemical conversion reactions remains a significant challenge. The Gong group designed an organosilane (TMOS) insulator layer with tunable pore size and surface wettability to enhance the stability and efficiency of silicon-based MIS photocathodes for water splitting.[162] By controlling the TMOS layer formation temperature, a discontinuous porous structure with pore sizes ranging from 200 nm to 1 μm was

achieved. The pore size played a crucial role in electron transport and ion/gas mass transfer during the hydrogen evolution reaction. An appropriate pore size of ~1 μm formed a thin gas layer within the pores, isolating the corrosive electrolyte from direct contact with the silicon substrate while allowing the Pt cocatalyst to interact with the electrolyte (Fig. 5a). However, when the pore size of TMOS exceeded 5 μm, silicon directly contacted the electrolyte, leading to photocathode corrosion (Fig. 5b). Furthermore, modifying the surface of the hydrophobic TMOS layer with hydrophilic hydroxyl groups tuned the surface wettability of the organic protection layer. The hydrophilic TMOS layer (W-TMOS) facilitated the desorption of hydrogen bubbles generated during the reaction, mitigating photocurrent density decay caused by bubble accumulation (Fig. 5c). The optimized hydrophilic TMOS protection layer exhibited exceptional photoelectrochemical performance, achieving a high photocurrent density of 35 mA cm^{−2} and a STH efficiency of 8% in 1 M HClO$_4$, with excellent stability over 110 hours, comparable to vacuum-deposited pinhole-free metal oxide protection layers. This organic protection layer design concept,

balancing the efficiency and stability of the hydrogen evolution reaction, provides a new approach for developing low-cost and highly efficient MIS photoelectrodes for water splitting. Most protection strategies for MIS photoelectrodes have focused on stabilizing the semiconductor layer against corrosion reactions, the insulator layers discussed previously represent an "in-device" protection approach to maintain the integrity of the light-absorbing semiconductor. However, the metal cocatalyst layers can also be susceptible to photocorrosion and mechanical stresses induced by gas bubble evolution.[163] Delamination and degradation of these cocatalyst layers constitute another key failure mode of MIS photoelectrodes that must be addressed. The Moon group proposed a novel device-on-top protection strategy that utilizes a highly permeable and transparent hydrogel as a protective layer on top of the MIS photoelectrode (Fig. 5d).[164] As shown in Fig. 5e, the hydrogel-protected photoelectrode (PAAM) demonstrated significantly improved stability, maintaining approximately 70% of the initial photocurrent over 100 h, with its photocurrent degradation rate gradually decreasing from 0.12 mA cm^{-2} h^{-1} to a stable 0.04 mA cm^{-2} h^{-1}. The enhanced stability can be attributed to the spatial confinement imposed by the nanopore network of the PAAM hydrogel on the metal cocatalyst, effectively preventing its agglomeration and shedding. Furthermore, the porous structure in the hydrogel provided abundant bubble nucleation sites, reliably manipulating the transmission of bubbles into the electrolyte, which helped avoid the negative impact of mechanical shear stress generated by bubbles.[165,166] This work not only expands the candidate materials for the insulator layer by applying hydrogel but also proposes a new paradigm for MIS photoelectrode protection strategies. The development of novel insulator layer materials, such as organic and hydrogel-based layers, expands the possibilities for designing efficient and stable MIS photoelectrodes for water splitting.

The insulator layers play a vital role in determining the conversion efficiency of MIS photoelectrodes. Single insulator layer strategies struggle to simultaneously meet the following requirements: (1) effective passivation of semiconductor surface defects and suppression of interfacial charge recombination; (2) formation of suitable band alignment with the semiconductor and metal layers to facilitate photogenerated carrier separation and transport; and (3) excellent chemical stability to withstand the harsh acidic or alkaline electrolyte environments. For example, TiO$_2$ exhibits outstanding chemical stability and is widely employed as a passivation protective layer. However, the band alignment between TiO$_2$ and many high-efficiency light-absorbing semiconductors (e.g., Si, Cu$_2$O, Sb$_2$Se$_3$) is suboptimal, limiting photovoltage output.[167-169] To address these challenges and balance various performance indicators, researchers have developed a multilayer insulator synergistic strategy by combining different advantages of two or more insulator materials. These common approaches include: (1) depositing an ultrathin, high-quality passivation layer on the semiconductor layer, followed by a thick TiO$_2$ protective layer.[170] The ultrathin passivation layer effectively passivates interface defects, while
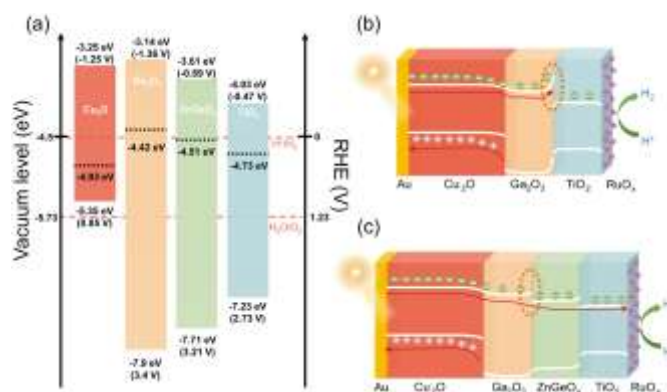

Fig. 6 Multilayer insulator synergistic strategy for MIS Photoelectrodes. (a) Energy diagrams of Cu$_2$O, Ga$_2$O$_3$, ZnGeO$_x$, and TiO$_2$; (b) Schematic diagram of the photogenerated carrier transport behavior in the Cu$_2$O/Ga$_2$O$_3$/TiO$_2$/RuO$_x$ photocathode under illumination; (c) Schematic diagram of the photogenerated carrier transport behavior in the Cu$_2$O/Ga$_2$O$_3$/ZnGeO$_x$/TiO$_2$/RuO$_x$ photocathode under illumination. Reproduced from ref. 171 under the terms of the CC-BY 4.0 license, copyright 2023, The Authors, published by the Springer Nature.

TiO$_2$ provides excellent stability. (2) inserting a buffer layer between the semiconductor and TiO$_2$.[153] This optimizes the band alignment within the MIS photoelectrodes and enhances photovoltage. (3) using an interfacial dipole layer to modulate the band edges of the semiconductor and insulator layers.[167] This reduces the band offset at the semiconductor/TiO$_2$ interface and promotes carrier transport. The Luo group recently demonstrated a significant improvement in the photovoltage of Cu$_2$O photocathodes by employing a multilayer insulator synergistic strategy.[171] This approach involved introducing a dual buffer layer consisting of Ga$_2$O$_3$ and ZnGeO$_x$. By inserting ZnGeO$_x$ as a second n-type buffer layer between Ga$_2$O$_3$ and TiO$_2$, a Ga$_2$O$_3$/ZnGeO$_x$/TiO$_2$ multilayer structure was formed. The band diagram in Fig.6a illustrates that the conduction band position of ZnGeO$_x$ lies between those of Ga$_2$O$_3$ and TiO$_2$, creating an energy level gradient (Fig.6c). This gradient effectively eliminates the potential barrier at the Ga$_2$O$_3$/TiO$_2$ interface (Fig.6b), leading to an optimized band alignment in the Cu$_2$O photocathode. Consequently, the onset potential of the photoelectrode increased from 0.91 V to 1.07 V, resulting in a notable enhancement of the photovoltage. As a single insulating layer struggles to balance surface passivation and carrier transport, the Gong group introduced a bifacial passivation strategy for Si-based MIS photoelectrodes.[172,173] This method employed a dual-layer passivation structure of a-Si for substrate surface passivation and TiO$_2$ for defect passivation at the metal/semiconductor interface. With a-Si/TiO$_2$ bifacial passivation, the minority carrier lifetime of Si dramatically increased from 18 μs to 2360 μs, and the minority carrier diffusion length improved from 148 μm to 1690 μm, leading to superior PEC water splitting performance. The photoanode achieved a 0.85 V vs RHE onset potential and 3.91% O$_2$ conversion efficiency, while the photocathode recorded a 0.62 V vs RHE onset potential and 12.66% H$_2$ conversion efficiency.

This bifacial passivation strategy not only overcomes the shortcomings of single-layer passivation but also ensures efficient carrier transport and excellent surface passivation. The multilayer insulator synergistic strategy provides a new perspective for the selection of insulator layers in MIS photoelectrodes. By conducting band engineering among different layers of the MIS photoelectrodes, efficient and stable PEC water splitting can be achieved. More detailed interfacial regulation strategies will be further discussed in the later section on the carrier-transfer mechanisms of MIS photoelectrodes.

4.3 Deposition technologies of insulator layer

The incorporation of high-quality and pinhole-free insulator layers enhances photoelectrode stability. However, defects like pinholes in the insulator films can facilitate the penetration of electrolyte molecules through grain boundaries, ultimately resulting in corrosion reactions and electrode failure.[174,175] Thin film deposition technologies have evolved to regulate the

quality and electrical properties of insulator layers, accommodating various material characteristics.

Broadly speaking, film deposition technologies include vacuum and non-vacuum methods (Fig. 7). Vacuum deposition technologies, particularly physical vapor deposition (PVD) and chemical vapor deposition (CVD), provide precise control over the film thickness and composition, beneficial for uniform and reproducible insulator layers. PVD employs various external energy sources, such as thermal energy, pulsed laser (PLD), and electron or ion beams, to vaporize target materials, which then condense on semiconductor substrates. Despite the precise control over film growth and stoichiometry offered by techniques like PLD and MBE,[21,176] their high energy consumption and expensive costs limit their applications in preparing the insulator layers for MIS photoelectrodes. Conversely, reactive magnetron sputtering, a more prevalent PVD method, provides a wide material selection (oxides, nitrides) and is adaptable to specific photoelectrode requirements.[177,178] Taking TiO_2 prepared via reactive
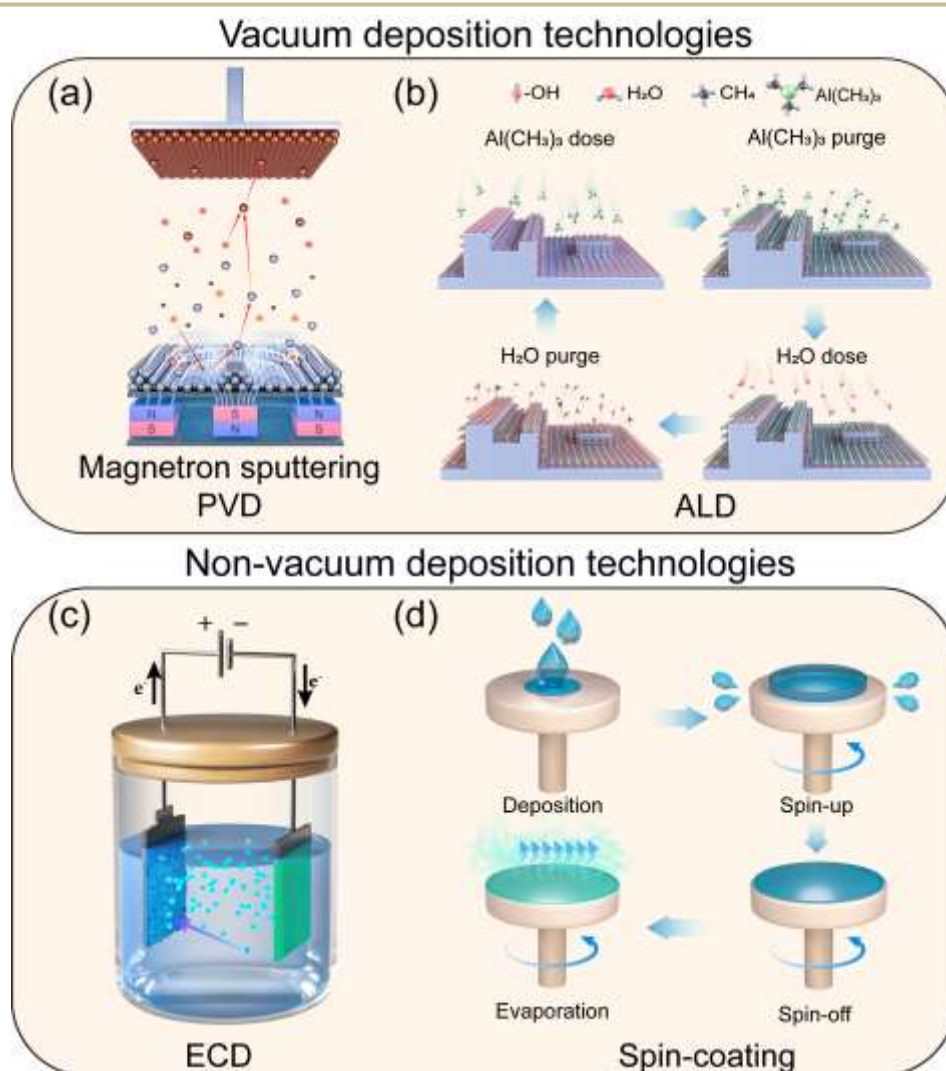

Fig. 7 Schematic diagram of the preparation of insulator layer based on vacuum deposition technologies and non-vacuum deposition technologies. (a) Deposition of TiO_2 films by reactive magnetron sputtering with oxygen. (b) Deposition of conformal Al_2O_3 films by ALD technique on a nanostructured substrate. (c) Electric-field induced electrochemical deposition technique. (d) Spin-coating deposition technique.

magnetron sputtering as an example, Fig. 7a illustrates electron collisions with argon atoms, generating Ar$^+$ ions under the electric field. These ions accelerate towards the cathode Ti target and bombard its surface, sputtering out Ti atoms that react with introduced oxygen to form TiO_2 clusters and subsequently deposit onto the substrate surface. To prevent substrate oxidation, a thin metal Ti interlayer (5-10 nm) is typically sputtered first to serve as both a protective layer and a carrier transport layer.[179] While the sputtered Ti atoms with sufficient energy could move in straight trajectories to ensure strong adhesion to the substrate, excessive atom energy would damage the substrate and introduce interface defects, hindering carrier transport.[180,181] The heavy bombardment of sputtered atoms might even cause intermixing with the substrate material, resulting in unwanted doping effects.[182] Therefore, sputtering conditions should be fine-tuned to avoid these detrimental effects. Bae *et al.* utilized high-power impulse magnetron sputtering (HiPIMS) to deposit TiO_2 thin films as an insulator layer.[183] HiPIMS-grown TiO_2 films displayed superior density and primarily consisted of stable rutile phases compared to those created by conventional DC magnetron sputtering (DCMS). This advantage was attributed to the high degree of ionization of the plasma and high energy distribution of ions under HiPIMS conditions,[184] which increased the diffusivity of TiO_2 clusters on the substrate surface and finally formed stable and high-density (4.15 g cm^{-3} at 400 °C) rutile phases. The quality of TiO_2 films strongly correlated with substrate growth temperature. While higher temperatures enhance crystallite size and film density, they can also cause intermixing between the TiO_2 layer and the Si substrate at temperatures above 500°C, deteriorating photoelectrochemical performance. The optimized HiPIMS-grown MIS photocathode exhibited only a 4% photocurrent degradation rate after a 24-hour photoelectrochemical stability test in 1 M KOH, whereas 20% degradation was observed in the DCMS-grown reference sample. PVD techniques are based on a line-of-sight deposition mechanism, where the source materials transfer directly to the substrate. This often yields non-uniform film and inadequate coverage on textured substrates due to the shadowing effect. Moreover, the film composition is restricted to target elements and reactant gases due to the absence of chemical control during the PVD deposition process.[145]

CVD is another vacuum-based technique for fabricating insulator layers in MIS photoelectrodes. Its ability to produce high-quality films with strong adhesion is especially beneficial for substrates with complex nanostructures. Jeong *et al.* utilized the CVD method to create a conformal TiO_2 protective layer on ZnO nanowires.[185] The resulting protective layer displayed uniform coverage and nanoscale control of TiO_2 thickness (5-50 nm). Thermal CVD also enables the in-situ formation of a protective layer through the self-reaction of the substrate with precursor reactants, such as through the oxidation,[19] sulfidation,[186] or nitridation[187] of the semiconductor layer. The self-reaction strategy utilizes commonly used precursor reactants, including oxygen, sulfur powder, and ammonia, thereby simplifying the preparation process and reducing

manufacturing costs. Direct participation of substrate surface atoms in protective layer formation ensures superior coverage and adhesion compared to deposited layers. Li *et al.* employed a high-temperature CVD technique to in situ fabricate a multifunctional Cu_2S layer on Cu_2O nanowires, enhancing both the PEC performance and photostability of the Cu_2O photocathode.[186] As a commercially recognized method, thermal CVD specializes in depositing high-quality thin films. Typically, the selection of highly reactive gases is critical to achieve optimal film deposition rates while maintaining substrate temperatures minimal. However, introducing multiple reactive precursors concurrently escalates the risk of homogenous gas-phase reactions, resulting in the formation of particulates embedded in the growing thin film.[188] ALD, a sophisticated variant of CVD, is integral in fabricating insulator layers for MIS photoelectrodes. The growth mechanism of the alternating self-limiting surface reaction endows the ALD deposition technique with the following advantages:[189] (1) Precise thickness control at an angstrom level. (2) Exceptional step coverage and conformality, even on complex 3D nanostructured substrates. The gas-phase precursor molecules penetrate all the surfaces of the substrate regardless of its geometry, without requiring line-of-sight access. (3) High-quality and pinhole-free films. Notably, the ALD process is dominated by heterogeneous reactions at the gas-solid interface. Residual precursors and by-products are purged out of the reaction chamber after each cycle, thereby preventing possible gas-phase reactions that could form particles to destroy the uniformity of the films. (4) In situ doping. The inherent flexibility of the ALD technique permits the infusion of dopant atoms by alternating precursor gases during thin film growth. Precise control of the timing and sequence of the precursor gases enables meticulous control over thin film doping, which offers an opportunity to manipulate the electrical conductivity and band gap energetics of the films, facilitating efficient carrier transport by ensuring band alignment throughout the MIS structure. The ALD technique, owing to its desirable properties and the availability of equipment, is increasingly used for fabricating insulator layers in MIS photoelectrodes. Prior to ALD deposition, the substrate undergoes pretreatment procedures, which involves cleaning and surface modification to enhance film quality and uniformity.[190] For instance, in depositing Al_2O_3 thin films (Fig. 7b), a two-step process is employed using metal organic compounds (like trimethylaluminum) and oxidants. The first half-cycle attaches these compounds to the treated substrate surface, forming Al-O bonds, followed by purging away unreacted precursors. The second half-cycle involves hydrolyzing leftover groups to complete the reaction. The combination of two half-cycles constitutes one ALD deposition cycle, which is repeated multiple times to achieve the desired film thickness. As previously mentioned, surface-textured substrates, while improving light absorption and carrier collection, can also increase undesirable charge recombination and accelerate photoelectrochemical corrosion. ALD technique addresses these challenges by uniformly coating nanostructures

with protective layers. Yu *et al.* employed ALD technique to deposit a TiO_2 insulator layer on the surface of black silicon (b-Si), which features densely packed holes with diameters ranging from 25 to 40 nm and 300 nm deep channels.[50] The inherent conformality of ALD ensured that the entirety of the nano-channels was uniformly coated with an 8 nm thick amorphous TiO_2 layer. The b-Si/TiO_2/$Co(OH)_2$ MIS photoanode demonstrated a superior separation efficiency compared to the b-Si/$Co(OH)_2$ photoelectrode, leading to a higher saturate photocurrent. This improvement could be attributed to the ALD-grown TiO_2 layer, which passivates defective surfaces and enhances the minority carrier lifetime in b-Si photoelectrodes. Moreover, the TiO_2 insulator layer protected the b-Si against corrosive reactions, thereby significantly improving its operational stability in air and electrolyte conditions.

The insulator layer of MIS photoelectrodes usually has a wide band gap (> 3 eV) to maintain transparency within the visible wavelength range. However, this design feature often results in significant band offsets at the semiconductor-insulator interface, hindering efficient charge separation and transport.[191] Heteroatom doping enables the fine-tuning of band structure and electrical properties of the insulator layers to suit various substrate materials. The conventional insulator layers composed of metal oxides have conduction band mainly comprised of s or d orbitals of metal elements, while the valence band are typically dominated by oxygen 2p orbitals. Doping with non-metallic elemental anions (N^{3-} or S^{2-}) can elevate the valence band of the insulator layer, while doping with transition metal cations with partially filled d orbitals (Cr^{3+}, Ni^{2+}, or $Mn^{2+/3+}$) can regulate the conduction band position.[192] The ALD technique enables in situ doping during the growth of the insulator layer and allows precise control over doping stoichiometry due to its layer-by-layer growth approach. Shen *et al.* introduced transition metal ions (Cr^{3+} and $Mn^{2+/3+}$) during the TiO_2 ALD growth process to create a tunable intermediate band within the insulator layer.[193] Their approach effectively minimized energy loss arising from a significant band barrier encountered as holes moved between the n-GaP and TiO_2 interface. The researchers elaborately investigated the effects of different transition metals, doping stoichiometry, and the alloying microstructures after post-deposition thermal treatment to fine-tune the intermediate band edge positions. After integrating with IrO_x cocatalysts, the MIS-based GaP photoanode demonstrated an impressive 28% absorbed photon to current efficiency and maintained stable water oxidation performance in neutral electrolytes for over 100 hours. An inherent drawback of ALD is its slow deposition rate, primarily resulting from a less than unity reactive adhesion coefficient and time-consuming dosing and purging process.[188,189] Innovations in ALD methods have emerged to address this limitation. Plasma-enhanced ALD employs highly reactive plasma species as reactants to enhance surface reaction kinetics. Spatial ALD counters the slow deposition rate by segmenting gas flow into separate areas and steadily shuttling the sample holder between them, effectively leveraging space to save time.

Non-vacuum deposition technologies offer an accessible alternative for fabricating protective layers on semiconductor photoelectrodes, especially in less demanding laboratory environments. Among non-vacuum deposition technologies, electrochemical deposition (ECD), droplet-based deposition, and solvothermal deposition are the most commonly utilized methods. As shown in Fig. 7c, ECD utilizes an electric field to direct precursor reactants to the conductive electrode, where redox reactions under specific voltage or current conditions form thin films.[194] Adjusting parameters like electrolyte composition and electrode configuration is crucial for optimizing film properties. However, the ECD technique requires careful management of overpotentials to prevent electrochemical corrosion and structural damage to the electrode. Photoelectrochemical deposition (PED) addresses this issue by using photogenerated carriers to assist in the deposition process, reducing the need for high overpotentials and mitigating corrosion risks.[84] Electrochemical deposition is widely used to prepare polymer protective layers, but the porosity and weak adhesion of these polymers can lead to film detachment, which facilitates the infiltration of solvent molecules into the electrode surface.[155-157] Azarpira et al. have demonstrated a facile electrosynthesis method to develop ultrathin organic protection layers through a two-step process.[195] The initial step involved immersing hydrogen-terminated n-type silicon electrodes in an ethanol/iodine electrolyte under cathodic conditions to achieve surface ethylation of the silicon. Subsequently, RuO_2 particles were transported to the silicon wafer surface via electrophoretic transport and participate in E2-elimination reactions of ethyl iodide, leading to the formation of a polymer network containing sp^2 hybridized carbon atoms. Merging the silicon ethylation with this dense carbon polymer resulted in a durable protective film, which exhibited both ample stability and favourable carrier conduction properties. In addition to the protective layer, the ECD/PED method is commonly used to deposit the cocatalyst layer of MIS photoelectrodes,[180] and even semiconductor layers such as crystalline silicon films through electrodeposition.[196] This all-encompassing PED/ECD approach provides a more economical and energy-conserving alternative to conventional MIS photoelectrode manufacturing, heralding a bright future for cost-effective MIS photoelectrode production.

Droplet-based deposition methods, encompassing drop-casting, spin-coating, and spray-coating, vary mainly in their precursor solution dispersion. These methods offer a straightforward and versatile approach to preparing protection layers for photoelectrodes by depositing precursor solutions onto the substrate. As illustrated in Fig. 7d, spin-coating efficiently spreads the precursor solution over the substrate using centrifugal force. The subsequent post-annealing process allows the excess solvent to evaporate, resulting in uniform and well-adhered films. The characteristics of spin-coated protection layers can be tailored by adjusting the rotating speed, post-annealing temperature, as well as the viscosity and concentration of the precursor solution. Recently, the single source precursor (SSP) approach has emerged as a versatile and

adaptable technique for fabricating protection layers on photoelectrodes. The SSP molecule contains all the necessary elements for the desired material. Decomposing the precursor hydrolytically at a set temperature enables the creation of the desired film through a solitary spin-coating step.[197-199] Sitharaman *et al.* demonstrated the fabrication of a TiO_2 protection layer by spin-coating titanium isopropoxide precursor solution onto $BiVO_4$ and Cu_2O to construct MIS photoelectrodes.[101] The TiO_2 protection layers uniformly covered the photoelectrodes after annealing at 200 °C for an hour. Lai *et al.* employed a heterobimetallic polyoxotitanate precursor to synthesize metal-doped TiO_2 films through a spin-coating SSP approach under ambient conditions.[199] The Ni-doped and Co-doped TiO_2 layers served as bifunctional coatings, acting as electrocatalysts for water splitting and protecting the semiconductor electrode from corrosion. The p-Si/TiNi photocathode was connected to a $BiVO_4$/TiCo photoanode to form a PEC tandem cell, which achieved a benchmark AB-STH efficiency of 0.59%.

The insulator layer in MIS photoelectrodes mainly serves dual roles of mitigating semiconductor layer corrosion and passivating surface states. This section delves into the corrosion mechanisms of photoelectrodes, evaluates candidate materials for insulator layers, and characterizes diverse film deposition technologies. The inclusion of an insulator layer expands the number of heterojunction interfaces, necessitating specialized interfacial regulation strategies to optimize carrier migration and separation. These strategies will be comprehensively addressed in the following section titled "Carrier-Transfer Mechanisms of MIS Photoelectrodes".

5. Metal-based cocatalysts of MIS photoelectrodes

5.1 Traditional metal-based cocatalysts

The photocurrent density (*J*) is a crucial indicator, gauging the capability of a photoelectrode to transform absorbed photons into electrical current, for assessing photoelectrode performance. The efficiency of the PEC water-splitting reaction depends on three key processes: light absorption, carrier separation, and interfacial carrier injection from the electrode to the electrolyte. Consequently, the photocurrent density of
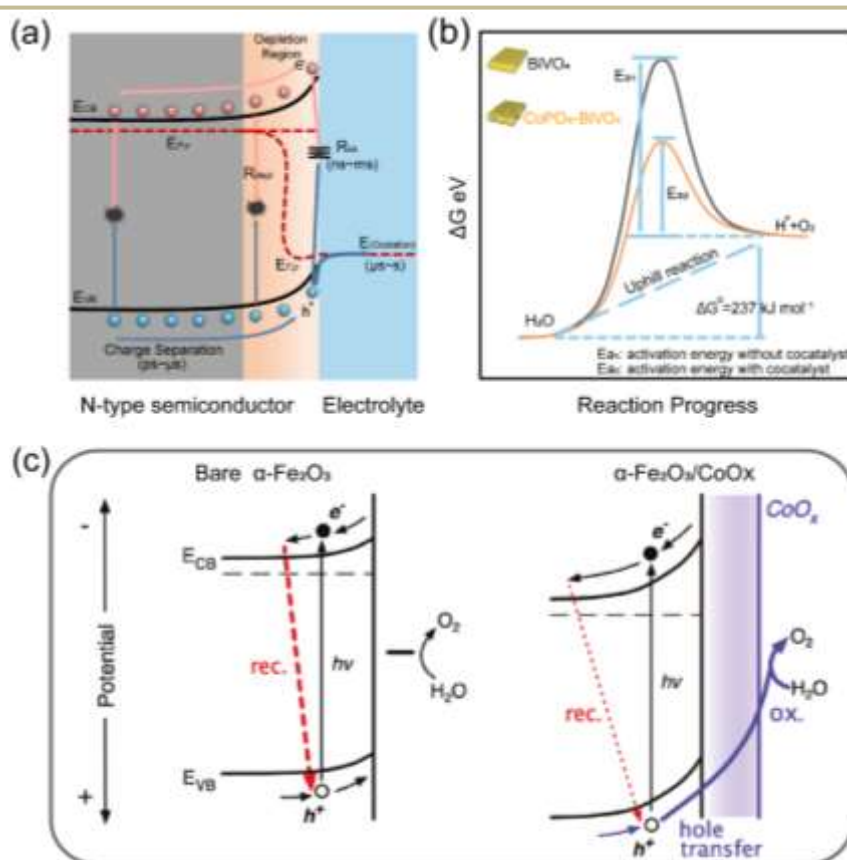

Fig. 8 Explanation of sluggish redox kinetics on semiconductors. (a) Carrier transport and main recombination paths of photogenerated carriers with corresponding timescales for an n-type semiconductor photoelectrochemical cell without external processes of photogenerated carriers include bulk phase carrier recombination (R_{bulk}), depletion region recombination (R_{depl}), and surface state carrier recombination (R_{ss}). (b) Schematic diagram of the change path of Gibbs free energy in water oxidation reaction with and without cocatalyst. Reproduced from ref. 204 with permission from the American Chemical Society, copyright 2012. (c) Schematic diagrams illustrating that addingcobalt phosphate onto the photoanode effectively suppresses carrier recombination. Reproduced from ref. 206 with permission from the American Chemical Society, copyright 2011.
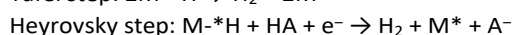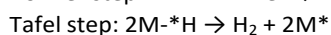
the PEC water-splitting reaction can be mathematically expressed as the following equation:

$$J = J_{max} \times \eta_{absorption} \times \eta_{seperation} \times \eta_{injection}$$

where J_{max} is determined by the energy band structure of the semiconductor electrode, representing the maximum achievable photocurrent when all incident photons with energies exceeding the band gap contribute to the current generation.[142] The light absorption efficiency ($\eta_{absorption}$) and charge separation efficiency ($\eta_{seperation}$) are shaped by the intrinsic semiconductor properties, including carrier lifetime and transport properties, absorption coefficient, thickness, and surface morphology. As previously mentioned, surface and interface engineering are prevalent tactics to bolster these efficiencies. The interfacial carrier injection efficiency ($\eta_{injection}$) quantifies the proportion of photogenerated carriers engaging in the desired water-splitting reactions. The interfacial redox reactions, marked by intricate chemical interactions between the photoelectrode and the electrolyte, are crucial processes within the PEC system. While solar cells have advanced to commercialization, PEC systems are still under exploration and refinement. The sluggish redox kinetics of the water-splitting reaction on most semiconductors stem from the rapid recombination of photogenerated carriers and the substantial activation energy required. Consequently, a significant bias is essential to initiate the desired redox reactions. The integration of cocatalysts into photoelectrodes has been proven effective in mitigating surface recombination and boosting the kinetic rate. Prior to engaging in the PEC redox reaction at the photoelectrode surface, photogenerated carriers undergo recombination processes in the bulk phase, depletion region, and surface states (Fig. 8a).[200,201] These recombination processes significantly diminish bias. The recombination the efficiency of photogenerated carriers. Time-resolved spectroscopic techniques, capable of monitoring reaction processes on the femtosecond time scale, grant researchers invaluable insights into the dynamics of photogenerated carriers and the mechanisms of PEC redox reactions.[202] As depicted in Fig. 8a, the oxidation reaction time varies from milliseconds to seconds,[202,203] considerably longer than the carrier recombination processes, which underscores the inadequate intrinsic conversion performance of semiconductors. As shown in Fig. 8b, the water splitting reaction exhibits a thermodynamic uphill process, necessitating overcoming a thermodynamic standard molar Gibbs free energy of 237 kJ mol^{-1}, as well as the kinetic activation energy. The CoPO$_x$/BiVO$_4$ photoanode exhibited a photocurrent density approximately 4.3 times higher than that of a pristine BiVO$_4$ electrode.[204] This enhancement can be attributed to the cocatalyst's role in reducing the water oxidation activation energy. The Durant group employed transient absorption spectroscopy to demonstrate that the introduction of cobalt phosphate effectively suppressed carrier recombination.[205,206] The coupling cobalt phosphate cocatalyst with the photoanode created an intimate heterojunction, promoting increased band bending for efficient electron-hole separation (Fig. 8c).

Electrons are depleted in the space charge region, while holes migrate to catalytic sites for water oxidation reaction.

Considering the timescale of carrier kinetics, the interfacial redox reaction is the rate-determining step in PEC water splitting. As previously highlighted, metal-based cocatalysts in MIS-based photoelectrodes offer reaction sites with lower activation energy which expedites the carrier injection process and subsequently reduces overpotential. However, the working mechanism of cocatalysts still remains controversial. A comprehensive understanding of the redox reaction mechanisms is essential for developing a new theoretical and experimental framework for the design of high-performance cocatalysts.[207] As depicted in Fig. 9, PEC water splitting involves two half-reactions: water reduction in the hydrogen evolution reaction (HER) and water oxidation in the oxygen evolution reaction (OER). The HER is a two-electron transfer reaction that takes place through either the Volmer-Tafel or the Volmer-Heyrovsky mechanism (Fig. 9a):

Volmer step: HA + M* + e$^-$ → M-*H + A$^-$

Tafel step: 2M-*H → H$_2$ + 2M*

Heyrovsky step: M-*H + HA + e$^-$ → H$_2$ + M* + A$^-$

The asterisk (*) indicates a binding site on the metal-based cocatalyst surface, while the A$^-$ species vary with the pH of the electrolyte, namely H$_2$O in acidic electrolyte and OH$^-$ in alkaline electrolyte.[208] The initial step entails the adsorption and reduction of HA, known as the Volmer reaction, leading to the formation of a chemisorbed hydrogen intermediate on the metal-based cocatalysts (M-*H). Subsequently, the evolution of H$_2$ can occur through two distinct reaction pathways, contingent upon the coverage of M-*H species.[209] High M-*H surface coverage would encourage the combination of two adjacent M-*H which results in producing H$_2$, referred to as the Tafel reaction. On the other hand, with low M-*H surface coverage, the adsorbed M-*H undergoes the Heyrovsky reaction, interacting with another HA molecule and an electron to yield H$_2$. The HER mechanism and rate-determining steps are governed by the free energy of hydrogen adsorption (ΔG_{H*}). The Tafel slope is commonly employed to assess the HER mechanism.[210] A positive ΔG_{H*} suggests weak hydrogen binding at the catalytic site, pointing to the Vollmer adsorption as the rate-determining step (Tafel slope~116 mV dec^{-1}). Conversely, a negative ΔG_{H*} indicates intermediate products occupying or potentially poisoning the reaction sites. In such cases, the rate-determining step becomes the Heyrovsky (~38 mV dec^{-1})/Tafel (~29 mV dec^{-1}) desorption process. Therefore, an optimal cocatalyst for HER should possess a ΔG_{H*} close to zero, balancing between activating the catalytic site and efficiently releasing molecular hydrogen. Nørskov et al. employed density functional theory to calculate ΔG_{H*} on various metal-based HER cocatalysts.[211] When plotting the experimentally measured HER current density against the calculated ΔG_{H*} values, a volcano-shaped curve (Fig. 9b) emerges which establishes a straightforward framework for comparing the HER performance across cocatalysts.[207]

Platinum-group metals (PGMs, such as Pt, Rh, Ir, and Pd) occupy the upper region of the HER volcano plot, exhibiting
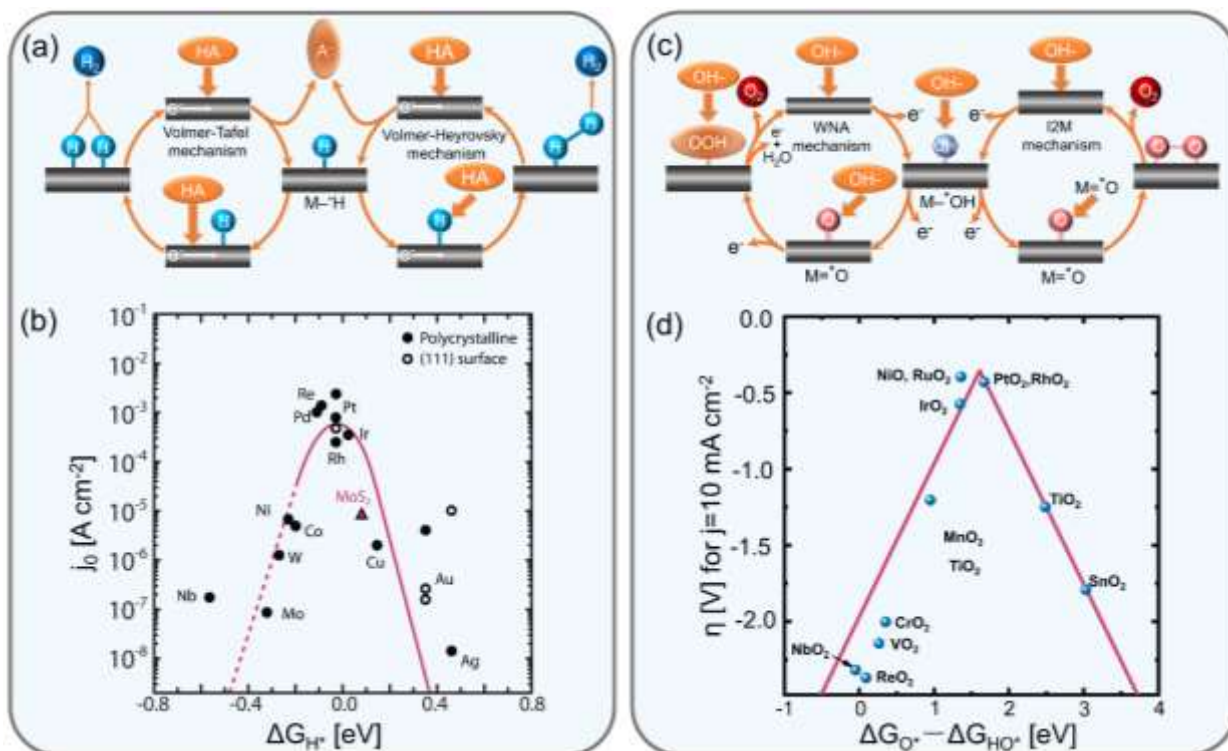
Fig. 9 Schematic diagram of the mechanism pathways of HER and OER reactions on metal-based catalysts and volcano plots of the common metal-based catalysts for HER and OER reactions. (a) Volmer-Tafel mechanism based on chemical desorption and Volmer-Heyrovsky mechanism based on electrochemical desorption. The A[-] species depends on the pH of the electrolyte. In an acidic solution, it corresponds to H_2O, whereas in an alkaline solution, it represents OH^{-}. (b) HER volcano plot depicting a function of the calculated free energy for hydrogen adsorption (ΔG_{H*}) and experimentally measured current density (j_0) for metals and MoS_2. Reproduced from ref. 207 with permission from the American Association for the Advancement of Science, copyright 2017. (c) WNA mechanism for single-site water oxidation and I2M mechanism for two-site coupling interaction in an alkaline electrolyte. (d) OER volcano plot depicting a function of the calculated free energy of ($\Delta G_{O*}-\Delta G_{HO*}$) and negative value of experimentally measured overpotential (η) for metal oxide catalysts. Reproduced from ref. 231 with permission from the John Wiley and Sons, copyright 2011.

nearly thermo-neutral ΔG_{H*} values and excellent HER performance (Fig. 9b). These noble metals are commonly employed as cocatalysts in MIS-based photoelectrodes and serve as benchmarks for evaluating other novel HER cocatalysts' performance.[19,212-214] However, their scarcity and high cost constrain their widespread application. Implementing micro-nano structures could enhance the utilization efficiency of cocatalysts while reducing the demand for cocatalyst loading. Dasgupta et al. achieved uniform deposition of Pt nanoparticles along p-Si/TiO₂ nanowires using ALD techniques.[215] By adjusting the ALD cycles, they controlled nanoparticle sizes between 0.5-3 nm, offering a cost-efficient alternative. Furthermore, nanostructure size significantly affects photogenerated carrier transfer kinetics and photoelectrode light absorption. Ji et al. employed a cost-effective and maskless submicron-scale structured nanosphere lithography technique to examine the impact of cocatalyst size on photoelectrode performance.[21] The process flow of nanosphere lithography, as illustrated in Fig. 10a, comprised three key steps. Firstly, a monolayer of 200 nm polystyrene nanospheres was transferred onto a p-Si/SrTiO₃ substrate using the Langmuir-Blodgett method. Next, titanium

and platinum were sequentially deposited. Finally, the nanospheres were removed from the substrate, resulting in the nanostructured bimetallic layer. According to the working mechanism in Fig. 10b, photogenerated electrons transfer efficiently to the bimetallic layer for water reduction required to occur within a distance shorter than the sum of depletion width (W_{dep}) and minority carrier diffusion length (L_{diff}).[19] Nanostructured cocatalyst dimensions, namely diameter and spacing, affect electron travel distance to the nearest metal catalyst. In samples with larger dimensions of 100 μm/200 μm and 400 μm/500 μm, electrons scattering and recombination hindered the transfer efficiency, resulting in a low fill factor (Fig. 10c). Conversely, the 0.05 μm/0.1μm sample exhibited an impressive applied-bias photon-to-current efficiency of 4.9% for water reduction. This notable efficiency could be attributed to shorter electron transfer distances to the adjacent cocatalysts, which are less than the W_{dep}.

Efficient and earth-abundant non-noble metal cocatalysts hold paramount importance for large-scale PEC systems. Numerous transition-metal-based materials, such as metals, alloys, oxides, hydroxides, chalcogenides, and phosphides, have
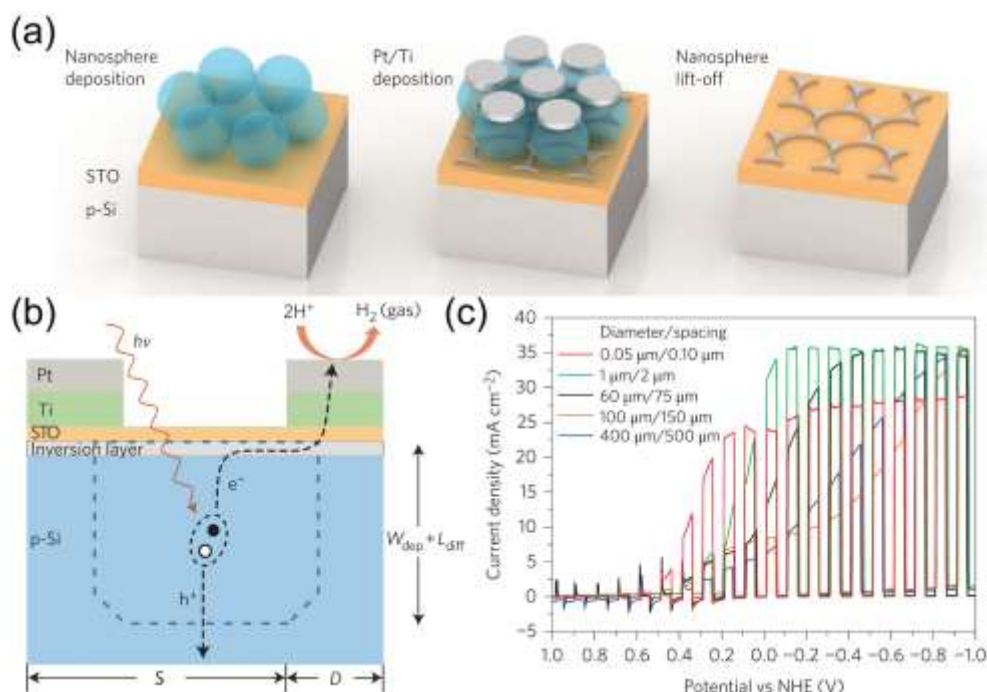
Fig. 10 Nanostructured noble metal cocatalysts in MIS-based photocathode for HER. (a) Schematic diagram of nanosphere lithography process. The sequential steps of nanosphere deposition, Ti/Pt bilayer metal deposition, and nanosphere lift-off from left to right. (b) Schematic diagram of the working mechanism of the p-Si/SrTiO$_3$/Ti/Pt photocathode. (c) LSV plots of p-Si/SrTiO$_3$/Ti/Pt photocathodes with various cocatalyst feature sizes. Reproduced from ref. 21 with permission from the Springer Nature, copyright 2014.

been investigated to replace noble metals where Mo, Ni, Co-based cocatalysts have demonstrated high performance for HER.[216,217] Nickel metal occupies a favourable position on the volcano plot (Fig. 9b) with an appropriate ΔG_{H*}, making it a promising HER cocatalyst. Ni-based alloys provide an avenue to increase the surface area of cocatalysts while simultaneously adjusting their electronic structure by the hypohyper-d-electronic interactive effect. Raj and Vasu investigated a series of Ni-based binary alloy electrocatalysts for HER, and found that Ni-Mo alloys excel in HER, achieving an overpotential of roughly 0.18 V over a 1500-hour electrolysis period.[218] Highfield *et al.* proposed a synergistic model to explain the working mechanism of Ni-Mo alloys, in which the Ni atom acted as a proton reduction center to dominate the Volmer step and the Mo atom facilitated the subsequent molecular hydrogen desorption step due to the stronger H-binding on Mo atom.[219] The H-trapping capability of Mo not only safeguarded the alloy against severe deactivation but also manifested the intrinsic electrocatalytic activity of Ni. The Lewis group initially integrated Ni and Ni-Mo alloys with p-Si microwire photoelectrodes, demonstrating light-to-H$_2$ efficiencies ranging from 0.2% to 0.4%.[62] Despite the relatively low photovoltage observed in the photoelectrode with Ni-Mo alloy cocatalyst due to an inefficient "pinch-off" effect, Warren *et al.* addressed this limitation by implementing a buried pn$^+$ junction in the semiconductor substrate.[64] Lin *et al.* employed the Ni-Mo alloy cocatalyst in an amorphous silicon-based MIS photocathode featuring a p-i-n homojunction.[220] The linear sweep voltammetry (LSV) curves in Fig. 11a revealed that

the onset potential of a-Si/TiO$_2$/Ni-Mo photocathode is only 60 mV lower than that of the Pt-based counterpart. Furthermore, the a-Si/TiO$_2$/Ni-Mo photocathode exhibited a comparable current density of approximately 11 mA cm^{-2} at 0 V *vs.* RHE. Most HER electrocatalysts exhibit lower activity in alkaline electrolytes compared to acidic media due to the inefficient water dissociation step.[221,222] Furthermore, metal-based cocatalysts employed in strong alkaline solutions may undergo hydroxylation reactions, resulting in dissolution and detrimental effects on electrode stability.[223] However, alkaline systems facilitate the thermodynamically and kinetically demanding water oxidation reactions. Therefore, optimizing PEC water-splitting efficiency and cost demands further study of metal-based HER cocatalysts in alkaline environments. Digdaya *et al.* assessed a TiO$_2$-protected amorphous silicon carbide photocathode with Ni-Mo alloy catalysts in 1 M KOH.[224] As revealed by the cyclic voltammetry (CV) curves in Fig. 11b, the a-SiC/TiO$_2$ photoelectrode without cocatalysts demonstrated a noticeable hysteresis onset potential (0.2 V *vs.* RHE) attributed to sluggish reaction kinetics on the TiO$_2$ surface, while the incorporation of Ni-Mo cocatalyst resulted in a substantial positive shift of the onset potential to 0.8 V *vs.* RHE. However, incomplete Ni-Mo nanoparticles coverage, obtained through electrochemical deposition, reduced the number of active catalytic sites. To address this issue, a thin Ni film was pre-deposited on the a-Si/TiO$_2$ photocathode, increasing active HER sites and enhancing electron transfer. This resulted in a steeper CV curve slope and a boosted photocurrent density to
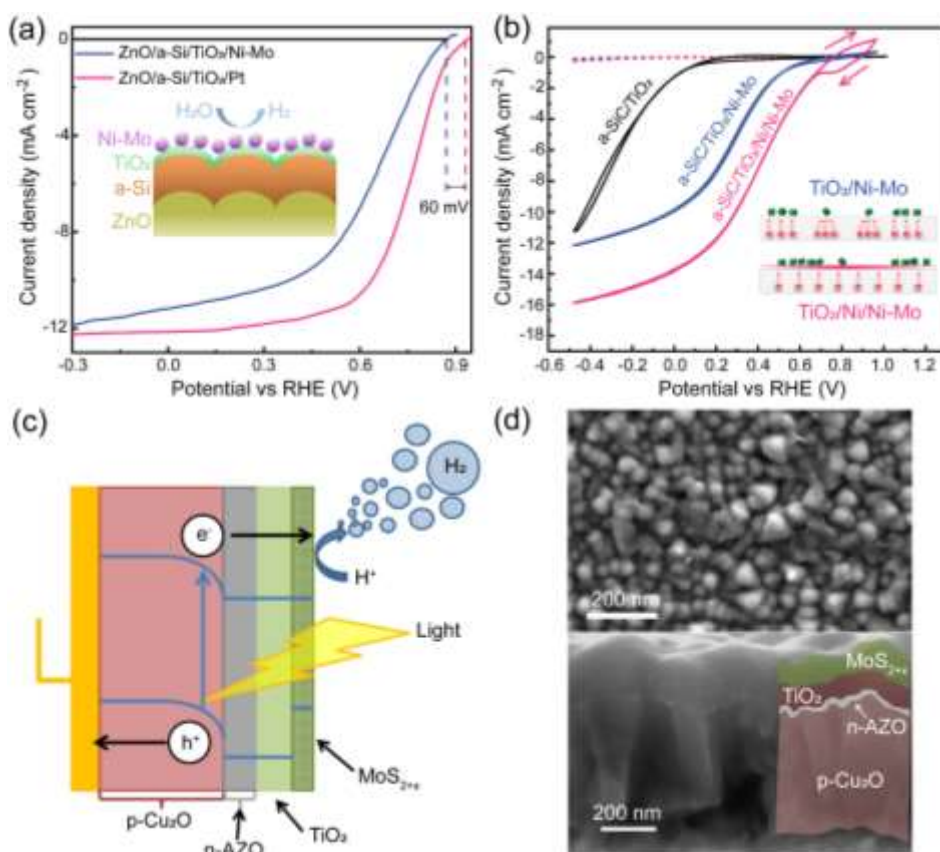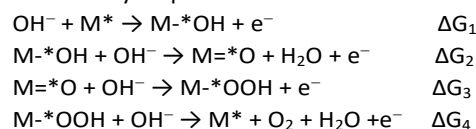
Fig. 11 Earth-abundant transition-metal-based cocatalysts in MIS photocathode for HER. (a) LSV plots of amorphous Si MIS-based photocathodes with Ni–Mo or Pt catalyst. Reproduced from ref. 220 with permission from the American Chemical Society, copyright 2013. (b) CV curves of a-SiC/TiO$_2$, a-SiC/TiO$_2$/Ni–Mo and a-SiC/TiO$_2$/Ni/Ni–Mo in a 1 M KOH electrolyte. The inset image elucidated the role of the Ni layer in facilitating the transfer of photogenerated carriers to the Ni-Mo cocatalysts. Reproduced from ref. 224 with permission from the Royal Society of Chemistry, copyright 2016. (c) Schematic structure of the p-Cu$_2$O/n-AZO/TiO$_2$/MoS$_{2+x}$ MIS photocathode. The combination of n-AZO and p-Cu$_2$O formed a photovoltaic p-n junction, leading to an enhanced photogenerated voltage. The TiO$_2$ layer safeguarded the buried p-Cu$_2$O/n-AZO junction from exposure to the aqueous environment; (d) Surface and cross-section SEM images of p-Cu$_2$O/n-AZO/TiO$_2$/MoS$_{2+x}$ MIS photocathode. Reproduced from ref. 227 with permission from the Springer Nature, copyright 2014.

14 mA cm^{-2} at 0 V *vs.* RHE. Exceptional properties of 2D materials, like graphene, have garnered extensive research attention in the past two decades. Among these materials, 2D layered transition metal chalcogenides, such as MoS$_2$, have emerged as prominent electrocatalysts for HER. Nørskov et al. computationally analysed the ΔG_{H*} of MoS$_2$, revealing that the Mo edge sites, not the basal plane, were electrochemically avtive for HER with ΔG_{H*} values (0.08 eV, Fig. 9b) comparable to PGM-based catalysts.[225] Chorkendorff et al. further employed scanning tunneling microscopy (STM) and electrochemical tests to establish a linear relationship between MoS$_2$ catalytic activity and its edge perimeter length.[226] Hence, the development of MoS$_2$ cocatalysts with a significant proportion of exposed edge sites enhanced catalytic performance. As an illustration, amorphous MoS$_2$ demonstrated exceptional HER catalytic activity owing to its substantial surface area.[207] Morales-Guio et al. employed the facile PED technique to deposit amorphous MoS$_{2+x}$ as cocatalysts (Fig. 11c).[227] SEM images (Fig.11d) revealed a 50–100 nm thick, conformal MoS$_{2+x}$ layer on the p-Cu$_2$O MIS photocathode. The conformal MoS$_{2+x}$ cocatalysts

facilitated photogenerated electron extraction, achieving high photocurrents reaching up to 5.7 mA cm^{-2} at 0 V *vs.* RHE This study highlights the promise of utilizing earth-abundant photoabsorber materials and cocatalysts in MIS photoelectrodes for efficient water splitting.

The OER, a complex 4-electron transfer process, exhibits a higher overpotential than HER and encompasses the transition of multiple intermediate species. Experimental and theoretical evidence identifies two distinct macroscopic reaction mechanisms to elucidate the fundamental process of the initial formation of molecular oxygen (Fig. 9c).[228] Alkaline conditions, beneficial for OER kinetics and catalyst stability, are usually chosen for mechanism investigation. The first mechanism involves the nucleophilic attack of water or hydroxide ions (WNA) on metal-oxo intermediates (M=*O), comprising four elementary steps and shown as follows:

$$OH^- + M^* \rightarrow M\text{-}^*OH + e^- \qquad \Delta G_1$$
$$M\text{-}^*OH + OH^- \rightarrow M=^*O + H_2O + e^- \qquad \Delta G_2$$
$$M=^*O + OH^- \rightarrow M\text{-}^*OOH + e^- \qquad \Delta G_3$$
$$M\text{-}^*OOH + OH^- \rightarrow M^* + O_2 + H_2O + e^- \qquad \Delta G_4$$

In these equations, the asterisk (*) represents a binding site of the metal-based cocatalysts. The OH⁻ ions adsorb onto the cocatalyst sites and subsequently undergo deprotonation to generate O* species which then react with H_2O to form HOO* intermediates. Finally, the HOO* intermediates decompose to release oxygen. The theoretical overpotential of OER is primarily determined by either the oxidation of HO* (ΔG_2) or the nucleophilic attack of O* (ΔG_3). Studies on diverse OER electrocatalysts reveal that two crucial intermediate adsorption free energies, ΔG_{HO*} and ΔG_{HOO*}, demonstrate a linear correlation ($\Delta G_{HOO*} = \Delta G_{HO*} + 3.2 \pm 0.2$ eV).[229,230] Therefore, the difference ($\Delta G_{O*} - \Delta G_{HO*}$) serves as a descriptor to assess the overpotential of the majority of OER catalysts. Experimental overpotentials at 10 mA cm⁻² of conventional metal oxide OER catalysts align closely with the theoretical overpotential volcano curve (Fig. 9d).[231] The second mechanism involves the coupling interaction of two metal-oxo radicals (I2M), leading to the formation of an O-O radical.[228] The I2M mechanism is more complex, where the free energy changes of oxygen-containing intermediates determine the specific reaction pathway. Detailed explanations of the I2M mechanism exist in other OER-related review papers and will not be covered in this review.[228,230,232] Under high-potential anodic oxidation, elemental metal surfaces tend to be oxidized to form metal oxides that are commonly employed as OER electrocatalysts. As depicted in Fig. 9d, catalysts with $\Delta G_{O*} - \Delta G_{HO*}$ values around 1.6 eV peak on the OER volcano plot. Notably, noble metal oxides, such as RuO_2, IrO_2, RhO_2 and PtO_2, exhibit exceptional OER activity with theoretical overpotentials as low as 0.37 V (1.6 − 1.23 V). McIntyre et al. fabricated a n-Si MIS photoanode coated with a 3 nm-thick Ir OER cocatalyst layer (Fig. 12a).[17] The photoelectrode integrated with an iridium metal layer demonstrated elevated current density and a more pronounced redox reaction waveform, signifying that the inclusion of a noble metal cocatalyst expedited carrier transfer process (Fig. 12b). As illustrated in Fig. 12c, the $n-Si/TiO_2/Ir$ photoanode exhibited excellent solvent tolerance from strong acid to strong alkali conditions. A photovoltage of ~550 mV was calculated for the $n-Si/TiO_2/Ir$ photoanode by comparing its overpotential under illumination with that of p^+-Si photoanodes in the dark (Fig. 12d). Subsequently, the McIntyre group employed ALD to synthesize noble metal oxide alloys (TiO_2–RuO_2 and TiO_2–IrO_x) as metal-based cocatalysts.[233,234] The utilization of high work function noble alloy cocatalysts resulted in the formation of a favourable Schottky contact with n-Si, achieving photovoltages exceeding 600 mV.

The high cost and scarcity of noble metal oxides have prompted the exploration of alternative OER cocatalysts. Transition-metal-based OER catalysts, like nickel-, iron- and cobalt-based oxides, hydroxides, and oxyhydroxides, have
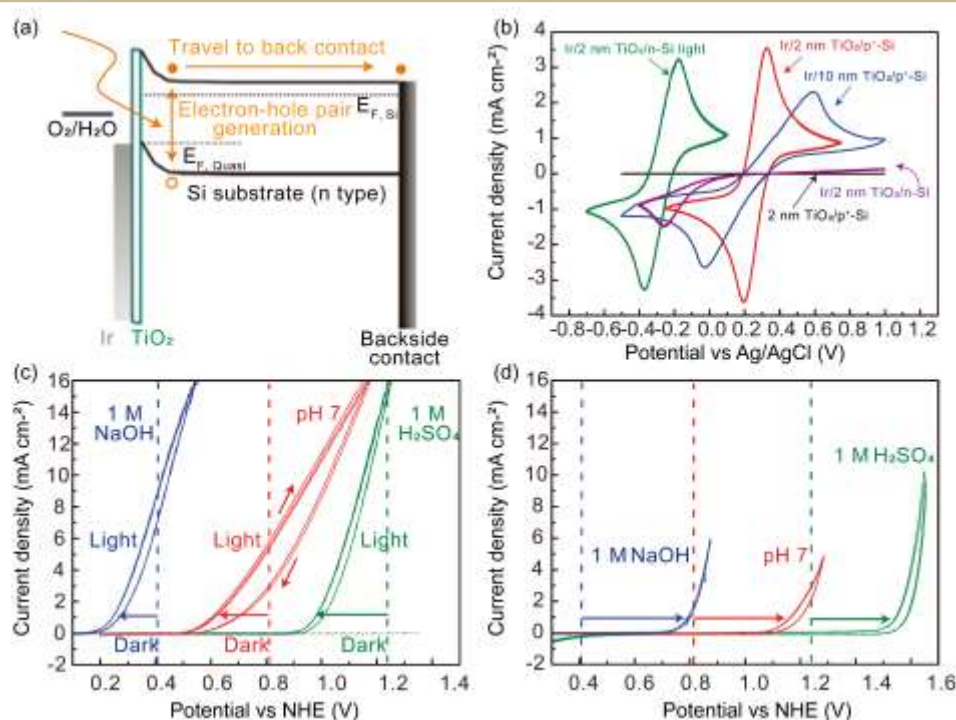

Fig. 12 Noble metal cocatalysts in MIS-based photoanode for OER. (a) Energy band diagram of the $Ir/TiO_2/SiO_2/n-Si$ photoanode. (b) CV curves in ferri/ferrocyanide solution of 2 nm TiO_2/p^+-Si (black line, in the dark), $Ir/2$ nm TiO_2/p^+-Si (red line, in the dark), $Ir/10$ nm TiO_2/p^+-Si (blue line, in the dark), $Ir/2$ nm $TiO_2/n-Si$ (violet line, in the dark), and $Ir/2$ nm $TiO_2/n-Si$ (green line, under 1 sun illumination). (c) LSV plots of $Ir/TiO_2/n-Si$ measured with (lines) and without (dots) simulated solar irradiation at 1 sun (AM1.5G) in acidic (1M H_2SO_4), neutral (1M phosphate-buffered, pH 7) and basic (1M NaOH) solutions. (d) LSV plots of $Ir/TiO_2/p^+-Si$ measured in the dark for acidic, neutral, and basic solutions. The dashed vertical lines in (c) and (d) indicated the thermodynamic redox potential for water oxidation at the corresponding pH values. Reproduced from ref. 17 with permission from the Springer Nature, copyright 2011.

emerged as highly promising cocatalysts for MIS photoelectrodes due to their cost-effectiveness and outstanding performance. Specifically, Michael *et al.* deposited a 2 nm nickel layer onto n-Si for both surface corrosion protection and OER cocatalyst.[20] The n-Si/SiO$_2$/Ni/NiO$_x$ photoanode achieved a ~500 mV photovoltage and showed 80-hour stability in continuous PEC water oxidation. However, direct metal-semiconductor contact and defect-rich n-Si/SiO$_x$ interfaces contribute to charge recombination, further limiting photovoltage due to Fermi-level pinning.[143] The Gong group. effectively resolved the challenges associated with spontaneous metal layer activation and unfavourable interface contact.[235] This was accomplished through implementing a high-quality Al$_2$O$_3$ tunneling layer using the ALD technique to suppress the charge recombination, and using the PED technique to controllably load highly active nickel oxyhydroxides (NiOOH) as a cocatalyst. Generally, metal layers are uniformly deposited by vacuum deposition technologies, resulting in what is termed a homogeneous MIS photoelectrode. The performance of the homogeneous MIS electrode is highly dependent on the thickness of the metal layer, as it directly impacts both the light absorption capability and the effective barrier height.[20] Inhomogeneous MIS photoelectrodes featuring metal nanoparticles as cocatalysts have garnered significant attention. Fabricated using the ECD or PED technique, these inhomogeneous electrodes capitalize on the pinch-off effect, establishing a new paradigm for MIS photoelectrodes.[236] Oh et al. provided valuable insights into the high performance of inhomogeneous MIS photoelectrodes operating in the pinch-off regime which enhanced photovoltage through metal-free regions with larger barrier height, while the metal-semiconductor junction facilitated low resistance pathways for photogenerated minority carriers participating in water splitting.[237] Their work revealed that photoelectrochemical activation of Ni nanoparticles through electrochemical cycling transformed a portion of Ni^0 nanoparticles into redox-active Ni(OH)$_2$ and the catalytically-active phase NiOOH, boosting electrocatalytic performance at the cocatalyst/electrolyte interface. Lee et al. optimized NiO$_x$/Ni nanoparticles coverage using pulsed electrochemical deposition followed by thermal annealing treatment that addressed the shading effect and increasing saturation photocurrent density.[238] The previous studies demonstrated that using Ni as a cocatalyst at high pH boosts photoanode performance through spontaneous activation of anodic oxidation. However, accurately discerning the influence of individual parameters on energy conversion performance remains challenging. Loget et al. presented a scalable electrodissolution method to prepare highly active inhomogeneous MIS photoanodes. The Si/SiO$_x$/Ni MIS photoanodes were initially deposited and subsequently modified with a redox-active Ni-Prussian blue derivative (NiFePB, Fig. 13a) by electrochemically oxidizing the Ni layer in a K$_3$Fe(CN)$_6$ electrolyte.[239] This modification increased layer transmittance and improved light penetration through the Ni film, which correlated with the number of electrochemical cycles. The inhomogeneous junction of Si/SiO$_x$/Ni/NiFePB

allowed for a precise performance evaluation, eliminating the influence of Ni oxidation. In the CV curves with KOH electrolyte, a quasi-reversible redox wave appeared at 1.07 V (*vs.* RHE) for n-Si under illumination and 1.37 V (*vs.* RHE) for p$^+$-Si in darkness, which is attributed to the NiOOH/Ni(OH)$_2$ redox couple in alkaline solutions. The inset image in Fig. 13b revealed that NiFePB reacted with KOH, forming Ni(OH)$_2$ and electrochemically converting to dense NiOOH cocatalysts at the anodic potentials. Furthermore, the authors introduced the urea oxidation reaction (UOR) to enhance the utility of PEC systems. The Si/SiO$_x$/Ni/NiFePB photoelectrode outperformed in the UOR compared to the OER, which achieved a 0.28 V potential gain at a 10 mA cm^{-2} current density and higher current densities at 1.23 V *vs.* RHE (Fig. 13b and c). This research presents novel prospects for PEC systems capable of utilizing urea-contaminated water to generate hydrogen. The incorporation of iron into nickel compounds is an effective method to enhance OER electrochemical performance.[216] Yu et al. first employed a facile electrodeposition technique to deposit discrete NiFe alloy islands on the np$^+$-Si surface (Fig. 13d).[240] The NiFe alloy/electrolyte interface exhibited lower charge transfer resistance and higher hole injection efficiency compared to the single metal (Ni or Fe)/electrolyte interface. Over long-term OER test, NiFe alloy underwent structural and compositional changes, likely attributed to the conversion of Ni and Fe into catalytically-active NiOOH/Ni(OH)$_2$, Fe$_2$O$_3$/FeOOH or NiFe-layered double hydroxide (LDH).[149,240,241] Guo et al. developed a high-performance MIS photoanode by integrating a NiFe-LDH nanosheet array with a polycrystalline silicon substrate. The hydrophilic nature and layered structure of NiFe-LDH enhanced water molecule adsorption and expedited gas molecule release.[242] Lee et al. investigated the catalytic effects of different NiFe alloy compositions on MIS photoanodes for PEC water oxidation using the EBE technique.[243] By controlling the Ni/Fe ratio, the n-Si/SiO$_x$/Ni$_{0.5}$Fe$_{0.5}$ photoanode demonstrated the lowest onset potential of 1.02 V *vs.* RHE and a high photovoltage of 530 mV (Fig. 13e). The n-Si/SiO$_x$/Ni$_{0.5}$Fe$_{0.5}$ photoanodes modified with Ni(OH)$_2$ cocatalysts cut the onset potential by 220 mV and boosted the fill factor by about 8% (Fig. 13f).

Cobalt-based compounds have also been widely studied as OER electrocatalysts. Our earlier analysis shows that metal cocatalysts dynamically transform during PEC water oxidation, shifting from surface-confined to volume-dominated catalysis in amorphous forms, thereby elevating OER turnover frequency.[244] However, these disordered cocatalysts are prone to cracking and delamination from the electrode surface which could damage those sensitive semiconductor substrates. The Sharp group utilized a plasma-enhanced ALD technique to fabricate biphasic films consisting of catalytically active Co(OH)$_2$ over compact nanocrystalline Co$_3$O$_4$ spinel layers.[245] This dual-phase design notably boosts catalytic activity while preserving the substrate. Deposition temperature significantly affects cobalt oxide film composition. As shown in Fig. 13g, XPS analysis revealed that the film deposited at 300 °C predominantly consisted of Co$_3$O$_4$, whereas the film deposited
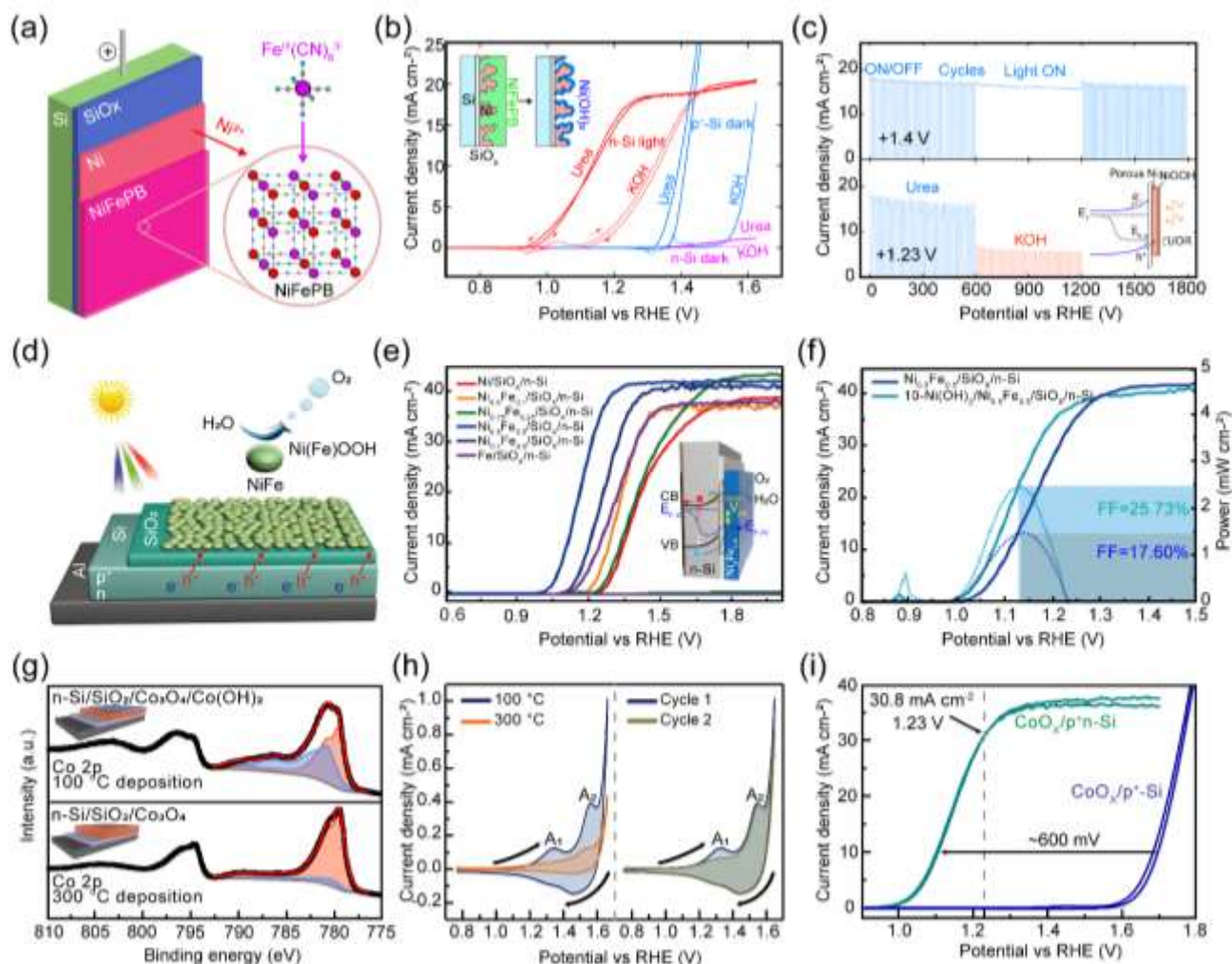
Fig. 13 Earth-abundant transition-metal-based cocatalysts in MIS-based photoanode for OER. (a) Schematic structure of the Si/SiOx/Ni/NiFePB MIS photoanode. The redox-active NiFePB was prepared by electrochemically oxidizing the Ni layer in a $K_3Fe(CN)_6$ electrolyte; (b) CV curves of n-Si/SiOx/Ni/NiFePB (red) under illumination, p$^+$-Si/SiOx/Ni/NiFePB (blue) in the dark, and n-Si/SiOx/Ni/NiFePB (pink) in the dark with the electrolyte of 1M KOH and 0.33M urea + 1 M KOH; (c) Current density *vs* time plots for UOR on Si/SiOx/Ni/NiFePB recorded at 1.40 V (top) and 1.23 V(down) while the electrolyte was replaced at 600 s by 1M KOH. Reproduced from ref. 239 under the terms of the CC-BY 4.0 license, copyright 2019, The Authors, published by the Springer Nature. (d) Schematic structure of the np$^+$-Si/SiOx/NiFe MIS photoanode. Reproduced from ref. 240 with permission from the John Wiley and Sons, copyright 2017. (e) LSV curves of the n-Si/SiOx/Ni$_x$Fe$_{1-x}$ photoanodes.; (f) LSV curves of the n-Si/ SiOx/Ni$_{0.5}$Fe$_{0.5}$ photoanodes with and without additional Ni(OH)$_2$ cocatalysts. Reproduced from ref. 243 with permission from the Elsevier, copyright 2022. (g) XPS analysis of Co 2p for CoO$_x$ films deposited at 100 °C (top) and 300 °C (down); (h) CV curves of CoO$_x$ films deposited at 100 °C and 300 °C (left) and comparison of first and second CV curve of CoO$_x$ films deposited at 100 °C (right); (i) LSV plots of p$^+$n-Si/SiOx/Co$_3$O$_4$/Co(OH)$_2$ under illumination and p$^+$n-Si/SiOx/Co$_3$O$_4$/Co(OH)$_2$ in the dark. Reproduced from ref. 245 with permission from the Springer Nature, copyright 2016.

at 100 °C exhibited a Co(OH)$_2$ surface layer. These variations in surface composition exerted a profound influence on the catalytic mechanisms. The redox transitions of Co^{3+} to Co^{4+} provided the highest activity sites for OER. Two distinct anodic peaks were observed for the film deposited at 100 °C, corresponding to the oxidation reactions of Co^{2+} to Co^{3+} (A$_1$) and Co^{3+} to Co^{4+} (A$_2$), respectively (Fig. 13h). When comparing the first and second CV curves, a reduced magnitude of A$_1$ suggested that the transformation of Co(OH)$_2$ to CoO(OH) was predominantly an irreversible reaction. The film deposited at

300 °C exhibited significantly lower redox activity, consistent with the surface-confined catalytic properties of bulk Co$_3$O$_4$. Biphasic Co$_3$O$_4$/Co(OH)$_2$ films enabled a volume-active structure which allowed the transformation of Co(OH)$_2$ into highly active catalytic sites. When the highly active Co$_3$O$_4$/Co(OH)$_2$ cocatalysts were integrated onto a p$^+$n-Si substrate, the resultant MIS photoanode achieved 37.5 mA cm^{-2} photocurrent density and a 600 mV photovoltage (Fig. 13i).

5.2 Molecular cocatalysts

The aforementioned cocatalysts are predominantly composed of bulk-phase materials. While these bulk cocatalysts offer advantages such as ease of preparation, high catalytic activity, and seamless integration into the electrode, their metal atom utilization is inefficient due to interface reactions and ambiguous catalytic center evolution, which presents a significant challenge to unravelling MIS photoelectrode reaction mechanisms. Natural photosynthesis, the most extensive and enduring solar-chemical fuel conversion system, has greatly inspired the advancement of artificial photosynthesis. This inspiration stems from the delicate coordination observed within natural photosynthesis, where internal enzyme-catalyzed reaction centers, light-absorbing pigment molecules, and redox-active cofactors interact harmoniously. Mimicking this complex operational mechanism is challenging due to the unique electrolyte conditions for living organisms. However, a unique opportunity exists in synergistically combining visible-light-absorbing semiconductors with human-engineered molecular catalysts inspired by active sites of enzymes.[246] Molecular catalysts typically consist of a metal center as the active site, along with organic ligands that establish the appropriate coordination environments to modulate the electronic structure.[247] Their distinct structures offer advantages including: (1) enhanced intrinsic activity of individual active sites; (2) efficient metal-atom economy; (3) a well-defined structure aiding mechanism studies; and (4) abundant ligand tunability.[25,247] Despite significant progress in developing efficient molecular catalysts,[248] achieving the efficient heterogeneous integration of molecular catalysts with semiconductor light-absorbing layers remains a major challenge. This integration is crucial for addressing low interfacial electron transport efficiency and poor stability associated with molecular catalysts. Typical methods employed to immobilize molecular catalysts on semiconductor substrates mainly include non-covalent bond interaction (physical adsorption, π-π stacking, entrapment) and covalent bonding. Compared to non-covalent bond immobilization, covalent bond assembly offers more robust immobilization and better orientation control of molecular catalysts on the electrode surface, promoting interfacial charge transfer and overall PEC system stability.[249] For non-metal oxide semiconductor substrates, surface functionalization is often necessary for achieving covalent interaction with the anchor groups on the molecular catalysts.[250] Incomplete surface functionalization can impact the subsequent heterogeneous integration of molecular catalysts. Depositing metal oxide layers on the semiconductor surface enables stable covalent connection through the coordination reaction between the hydroxyl groups on the metal oxides and the anchor groups, which makes the molecular cocatalysts perfectly fit with the MIS photoelectrodes. As shown in Fig. 14a, the Turner group employed ALD-TiO$_2$ deposition on the p-GaInP$_2$ substrate to facilitate the grafting of Co-based molecular cocatalysts with carboxylic acid anchor groups.[251] During prolonged PEC operation, the carboxylate linkage on the TiO$_2$ surface would undergo hydrolysis under alkaline conditions, detaching the bound molecular catalyst from the photoelectrode surface.

Additionally, the cyclic operating voltage range could induce changes in the structure and redox properties of the molecular catalyst. To enhance the long-term stability of MIS photoelectrodes with molecular catalysts, an additional 10-cycle overlayer of ALD-TiO$_2$ (~0.4 nm) was deposited onto the surface of the immobilized Co-based molecular catalysts. The Co-modified photocathode demonstrated a remarkable improvement in PEC performance compared to the untreated electrode. Under illumination, the photoelectrode modified with the Co-based molecular catalyst (E3) exhibited a more positive onset potential and faster reaction kinetics than those of the bare p-GaInP$_2$ photoelectrode (E1) and TiO$_2$-coated photoelectrode (E2). These observations indicated that the Co-based molecular catalyst effectively reduced the kinetic barrier and enhanced the activity for PEC water reduction (Fig. 14b). In contrast, the performance of the p-GaInP$_2$ electrode modified with non- covalently linked molecular catalysts (dash line) closely resembled that of TiO$_2$-coated photoelectrodes (E2), suggesting the benefit of covalent bonding for enhanced charge transfer. Although active site multiplication can boost photoelectrode activity, inherent planarity of commercial semiconductor substrates and the conformality of ALD deposition techniques would restrict the loading capacity of molecular catalysts. In Fig. 14c, the Reisner group employed a cost-effective slot-coating technique to introduce a mediator layer of mesoporous titanium dioxide (meso-TiO$_2$).[252] The meso-TiO$_2$ layer served two key functions: (1) acting as an electron-selective layer to enhance photogenerated charge transfer to the active center of the molecular catalyst and suppress back electron transfer, and (2) increasing the loading capacity of the molecular catalyst due to its porous three-dimensional structure and hydrophilic characteristics. The photoelectrode incorporating NiP and CoP^3 molecular catalysts significantly outperformed the catalyst-free counterpart in photocurrent density (Fig. 14d). Furthermore, the method facilitated hydrogenase integration with p-Si, establishing a versatile platform for hybrid MIS-based PEC systems. In natural photosynthetic systems, the spatially directed transport of photogenerated carriers through the multi-step electron transfer process involving molecular cofactors effectively minimizes carriers recombination,[246] providing insights for efficient hybrid PEC system design. In Fig. 14e, the Meyer group employed the electron-deficient perylene-diimide derivative (PDI) as an electron transfer mediator that converted photoexcited state after illumination and formed a heterojunction with a nanostructured p-Si substrate.[253] This enabled the efficient transfer of photogenerated electrons from the conductive band of p-Si to nickel-based molecular catalysts (NiCt). The p-Si/Ti/TiO$_2$/-PDI'-NiCt photocathode demonstrated increased photocurrents at applied potentials below −0.3 V *vs.* NHE (red dashed line, Fig. 14f), owing to the effective catalysis of water reduction by the NiCt. However, flat p-Si-based electrodes with the same components displayed remarkably low photocurrents, underlining the need for greater catalyst loading. The authors also investigated a tandem cell configuration based on fully molecular catalysts for solar-driven

water splitting, which combined the photocathode with a dye-sensitized SnO₂/TiO₂/-
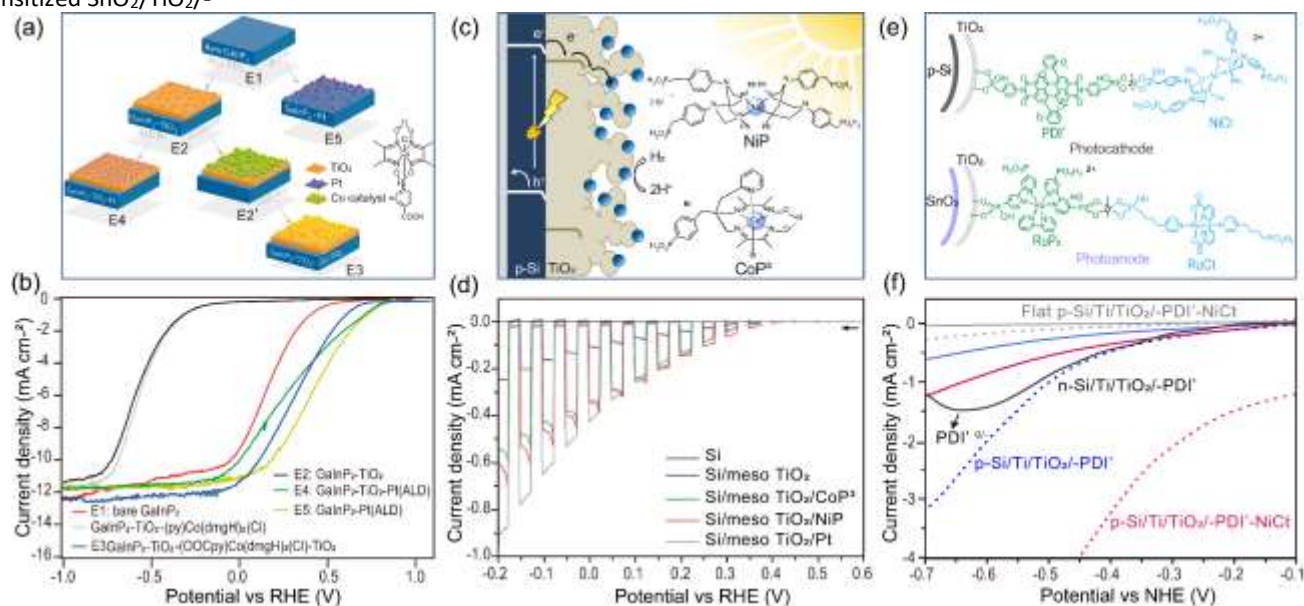

Fig. 14 Molecular cocatalysts for MIS-based photoelectrodes. (a) Schematic diagram of the p-GaInP₂ photoelectrode modified with Co-based molecular cocatalysts preparation process; (b) LSV curves of MIS-based photoelectrode with the target cobalt molecular catalyst (E3) and other comparative photoelectrodes. Reproduced from ref. 251 with permission from the Springer Nature, copyright 2015. (c) Schematic diagram of Si/mesoTiO₂/ NiP or CoP³ photocathode; (d) LSV curves of Si, Si/ mesoTiO₂, and Si/mesoTiO₂/ CoP³ or NiP or Pt. Reproduced from ref. 252 under the terms of the CC-BY 3.0 license, copyright 2017, The Authors, published by the Royal Society of Chemistry. (e) Structure of the p-Si/Ti/TiO₂/PDI'-NiCt photocathode and a dye-sensitized SnO₂/TiO₂/-RuP₂-RuCt photoanode; (f) LSV curves of p-Si/Ti/TiO₂/-PDI' (blue), n-Si/Ti/TiO₂/-PDI' (black), p-Si/Ti/TiO₂/-PDI-NiCt (red) and flat p-Si/Ti/TiO₂/-PDI'-NiCt (gray) under dark (solid line) or illumination (dashed line). Reproduced from ref. 253 with permission from the American Chemical Society, copyright 2019.

RuP₂-RuCt photoanode (Fig. 14e). In addition to molecular catalysts, Yang and Reisner have proposed the integration of enzymes and more complex living cells with synthetic materials to develop semi-artificial photosynthetic systems, which represents a closer step towards mimicking natural photosynthesis.[254] While the construction of efficient and stable semi-artificial photosynthesis systems remains a great challenge, it expands the range of available cocatalysts for the development of MIS photoelectrodes.

5.3 Single-atom cocatalysts

The number and intrinsic activity of active sites are two macroscopic parameters that impact the overall catalytic activity of cocatalysts. A promising approach to enhancing both parameters simultaneously is by reducing the size of cocatalysts. In Fig. 15a, the progressive reduction in the size of metal-based catalysts is illustrated, spanning from metal particles (> 8 nm), metal nanoparticles (2-8 nm), metal nanoclusters (2-30 atoms), atomically dispersed metal catalysts (ADMCs), single-site heterogeneous catalysts (SSHCs), and single-atom catalysts (SACs). Atomically dispersed metal catalysts mainly include ADMCs, SSHCs, and SACs. For detailed definitions and distinctions among these catalyst types, we refer readers to relevant review literature.[26,255,256] As depicted in Fig. 15b, reducing metal particle size elevates the unsaturated coordination environment and boosts surface free energy and specific activity, enhancing interactions with reactants and

substrates.[257] The ultimate outcome of reducing the size of metal particles is the formation of SACs where isolated metal atoms are dispersed on suitable supports without any interaction among themselves, leading to nearly 100% atomic utilization. Since their initial conceptualization by Zhang et al. in 2011, SACs have been extensively investigated in the field of heterogeneous catalysis.

In the realm of photocatalytic reactions, SACs with distinct geometric and electronic properties confer advantages to improve activity and selectivity. These benefits stem from enhanced light-harvesting capabilities through modifications of the energy band structure of semiconductor substrates, more favourable adsorption of reactants, efficient charge transfer through strong interactions between metal atoms and supported substrates, as well as more active sites for surface reactions (Fig. 15c).[26,258] However, the high surface energy of single-metal atoms makes them susceptible to migration and aggregation into nanoparticles, particularly under harsh electrolyte conditions during long-term operation. Similar to molecular catalysts which rely on organic ligands to create a coordination environment for stabilizing metal atomic centers, SACs achieve a stable dispersion of single-metal atoms through strong coupling interactions with anchoring supports. Currently, powder-form SACs synthesized through pyrolysis or wet chemical methods are widely used in electrocatalysis and photocatalysis.[255] However, there have been relatively few

studies on the utilization of SACs anchored onto semiconductor substrates to develop heterogeneously integrated photoelectrodes for PEC energy conversion.[259-261] This
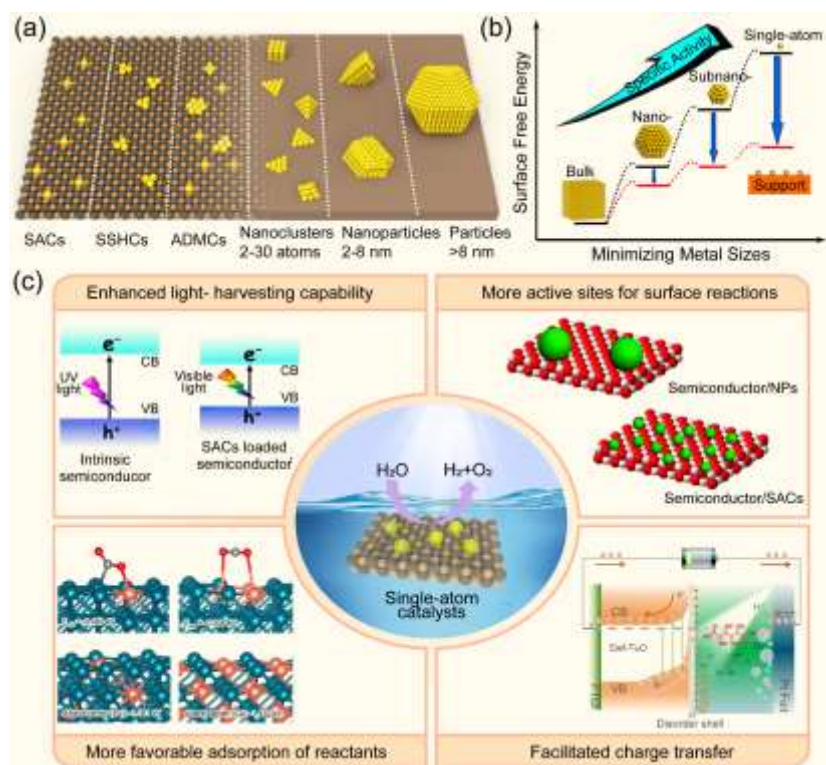

Fig. 15 (a) Schematic illustration of cocatalysts with different sizes including single-atom catalysts (SACs), single-site heterogeneous catalysts (SSHCs), and atomically dispersed metal catalysts (ADMCs), metal nanoclusters, metal nanoparticles and metal particles. Reproduced from ref. 256 with permission from the John Wiley and Sons, copyright 2019. (b) Schematic illustration of the alterations in surface free energy and specific activity per metal atom as a function of metal particle size, along with the influence of the support on the stabilization of single atoms. Reproduced from ref. 257 with permission from the American Chemical Society, copyright 2013. (c) Schematic illustration of the diverse roles of SACs in photocatalytic reactions, including their contributions to enhanced light-harvesting capabilities, improved adsorption of reactants, facilitated charge transfer, and the provision of more active sites for surface reactions. Reproduced from ref. 26 with permission from the American Chemical Society, copyright 2020; ref. 261 under the terms of the CC-BY 4.0 license, copyright 2023, The Authors, published by the Springer Nature; ref. 262 with permission from the American Chemical Society, copyright 2017.

limitation primarily arises from the scarcity of suitable single-atom surface anchoring sites on traditional semiconductor substrates, which restricts the loading capacity of single-metal atoms.[255] Jun et al. employed the ALD technique to disperse Ir single atoms (SAs) uniformly on a NiO/Ni mediator layer, where the Ni sites in the NiO lattice matrix were substituted by Ir atoms.[263] This led to the formation of thermodynamically more stable Ir SAs/NiO/Ni SACs, due to strong covalent bonding in the lattice matrix. The NiO/Ni mediator layer served as a bridge between the Ir SAs and the n-Si light-absorbing layer, enabling the construction of an efficient MIS photoanode for water oxidation. Fig. 16a presents the aberration-corrected high-angle annular dark field scanning transmission electron microscopy (HAADF-STEM)) images, clearly demonstrating Ir SAs homogeneously dispersed on the NiO thin film, with no evidence of aggregated nanoclusters or nanoparticles. In Fig. 16b, the Ir SAs/NiO/Ni/ZrO$_2$/n-Si photoanode demonstrated a significant improvement in photoelectrochemical performance,

as evidenced by an onset potential of 0.97 V (*vs.* RHE) and a current density of 27.7 mA cm^{-2} at 1.23 V (*vs.* RHE). This notable enhancement can be attributed to the characteristics of Ir SAs that minimize charge recombination and facilitate catalytic surface reactions. Charge transfer dynamics between single-metal atoms and the semiconductor support are crucial for optimizing PEC conversion efficiency. As depicted in Fig. 16c, the photoanode containing Ir SAs exhibited significantly higher charge transfer efficiency compared to the photoanode with Ir film and Ir nanoclusters. This affirmed that Ir SAs enhanced the separation and transfer efficiency of photogenerated carriers. DFT calculations explored the reaction mechanism of Ir SAs/NiO/Ni SACs (Fig. 16d), identifying isolated Ir atoms as the active catalytic centers that effectively lower the thermodynamic energy barrier of the potential-determining step (O* to OOH*, η= 0.621 V). In Fig. 16e, a localized polarization phenomenon between Ir single atoms and OH intermediates was observed in Ir SAs/NiO/Ni SACs, which

facilitated the efficient hole transport to the surface reactants. This innovative approach perfectly integrates single-atom cocatalysts with silicon-based substrates, delivering high-

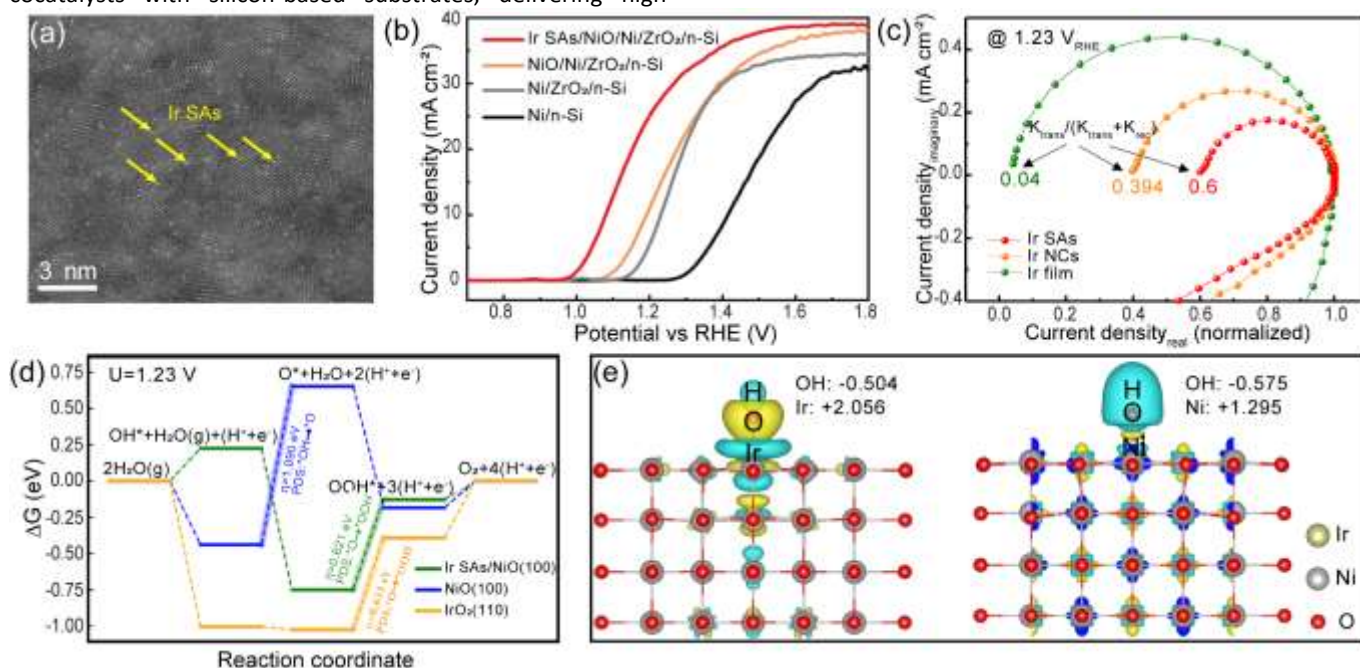performing MIS photoelectrodes and expanding the cocatalyst options for MIS-based systems.

Fig. 16 Single-atom cocatalysts for MIS-based photoelectrodes. (a) HAADF-STEM image of Ir SAs/NiO thin-film catalyst. (b) LSV curves of the following photoanodes: Ni/n-Si, Ni/ZrO$_2$/n-Si, NiO/Ni/ZrO$_2$/n-Si, and Ir SAs/NiO/Ni/ZrO$_2$/n-Si. (c) Nyquist plots of Ir SAs, Ir NCs, and Ir film at an applied potential of 1.23 V *vs.* RHE. (d) Free energy diagrams for OER on Ir SAs/NiO (100), NiO (100), and IrO$_2$ (110) at an applied potential of 1.23 V *vs.* RHE. (e) Charge density redistribution diagrams of Ir SAs/NiO and NiO during OER. Reproduced from ref. 263 under the terms of the CC-BY 4.0 license, copyright 2023, The Authors, published by the Springer Nature.

A pure semiconductor light-absorbing layer usually exhibits sluggish redox kinetics for the PEC conversion reaction. Incorporating a metal-based cocatalyst layer can lower the redox reaction barrier and promote the accumulation of photogenerated carriers. This section reviews the use of various cocatalysts in MIS photoelectrodes, covering categories like noble metals, earth-abundant transition metals, molecular catalysts, and single-atom catalysts. However, the introduction of continuous metal layers or nanoparticles can also induce parasitic light absorption, compromising the light absorption efficiency of semiconductor layers. Resolving this trade-off between light absorption and catalytic activity stands as an important research direction in metal-based cocatalyst design.

6. Carrier-transfer mechanisms of MIS photoelectrodes

In the preceding section, we provided a comprehensive overview of the three components comprising the MIS photoelectrodes, encompassing the materials, corrosion mechanism, thin film fabrication technologies, and catalytic mechanism. While the light-absorbing semiconductor layer, protective insulator layer, and metal-based cocatalyst layer may individually exhibit remarkable properties, the misalignment of energy levels among these components can result in energy loss

during charge transport across the interface and significantly diminished overall solar conversion efficiency. It is crucial to recognize that the interfaces between the various material components play a critical role in determining the overall system performance. These interfaces often act as bottlenecks for energy transfer, limiting the rate and efficiency of the energy conversion process. The inclusion of insulator and metal-based cocatalyst layers introduces additional interfaces, namely the semiconductor/insulator and insulator/cocatalyst interfaces that affect the efficiency of photogenerated charge separation. Therefore, a thorough comprehension of the charge-transfer mechanism in MIS photoelectrodes enables the meticulous design of these interfaces to guarantee energy compatibility throughout the entire system, thereby maximizing the solar-to-chemical conversion efficiency.[144,264] As discussed in the insulator layer section, the majority of materials used for this layer possess wide band gaps and low electrical conductivity. These characteristics pose challenges to the efficient carrier transport across the semiconductor/insulator layer interface. Consequently, extensive research focuses on fine-tuning the energy band structure and electrical properties of the insulator layer to optimize the energy level alignment across the semiconductor/insulator interface. Taking into account the characteristics of the insulator layer and the energy band regulation strategy, Fig. 17 illustrates the four prevalent carrier-transfer mechanisms of MIS photoelectrodes where

photogenerated carriers transport via the tunnelling effect of the ultrathin insulator layer (Fig. 17a), the conduction/valence band of the insulator layer (Fig. 17b), the constructed defect

states or intermediate band within the bandgap of insulator layer (Fig. 17c), and the embedded conduction pathways within
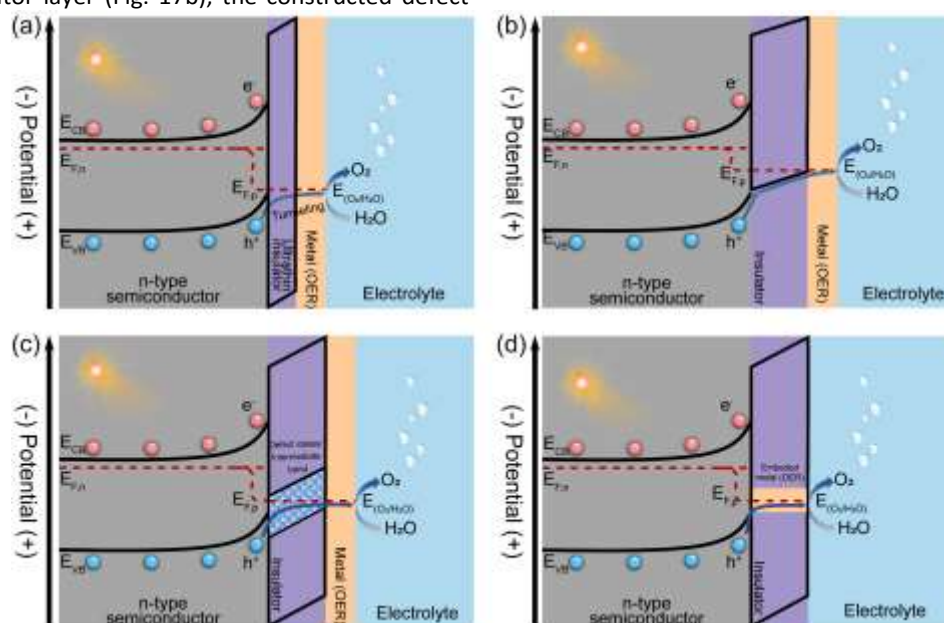

Fig. 17 Schematic illustration of band diagrams showing carrier-transfer mechanisms of MIS-based photoelectrodes with n-type semiconductors. (a) Photogenerated holes tunnel through an ultrathin insulator layer usually with a thickness less than 3 nm. (b) Photogenerated holes transport across the insulator layer via its valence band. (c) Photogenerated holes transport across the insulator layer via defect states or intermediate bands. (d) Photogenerated holes transport across the insulator layer via embedded metal conduction paths.

the insulator layer (Fig. 17d). Furthermore, the work function, coverage, and morphology of metal-based cocatalysts significantly influence the carrier transport at both the insulator/cocatalyst interface and the photoelectrode/electrolyte interface. This section concentrates on elucidating the carrier-transfer mechanisms and energy band regulation strategies in MIS photoelectrodes.

6.1 Carrier-transfer based on the tunnelling effect

The insulator protective layer, characterized by its wide bandgap, allows for light transmission and enhances stability. However, it compromises conductivity due to the lack of internal electronic states for charge transport and energy alignment.[264] Constraining the thickness of the insulator protective layer to below 3 nm allows the direct tunnelling of carriers through the insulator layer (Fig. 17a). This approach effectively circumvents the issue of energy band incompatibility between the insulator layer and semiconductor layer. Advanced ALD technique enables the fabrication of pinhole-free ultrathin tunnelling protective layers, accelerating their development in MIS photoelectrodes.[17] The tunnelling insulator layer thickness and the quality of the semiconductor/insulator interface are crucial parameters in optimizing the MIS photoelectrode performance. The Linic group combined modelling and experiments to investigate how ultrathin insulators affect MIS photoelectrode performance.[150,265] They fabricated Ni/HfO$_2$/n-Si MIS photoanodes, adjusting the HfO$_2$ thickness via the ALD cycle count. The introduction of the HfO$_2$ protective layer led to a remarkable enhancement in photovoltage, peaking at 479 mV

for the 2.1 nm HfO$_2$ layer, but diminishing for thicker HfO$_2$ layers. To elucidate these findings, authors developed a tunnelling probability model and demonstrated that the 2.1 nm thick HfO$_2$ insulator layer resulted in an intermediate tunnelling probability which could limit the large electron flux to suppress charge carrier recombination rates, thereby obtaining the optimized photovoltage. Although optimizing the insulator thickness improved photovoltage, it still fell short of the theoretical upper limit, known as the flat-band potential (V_{fb}). This discrepancy indicates the presence of additional losses that could not be mitigated solely by optimizing the insulator thickness. Hemmerling et al. formulated a photovoltage expression for MIS systems based on tunneling mechanics.[144,265] Their analysis revealed that besides insulator thickness, the ideality factor (n), the barrier height (ϕ_b), and the photocurrent (J_{ph}) also affect photovoltage. In an ideal MIS system (n=1), as shown in Fig. 18a, the insulator had no impact on the ϕ_b, enabling the exponential reduction of the reverse saturation current density (J_s). However, in a non-ideal state (n > 1), the combined charge from the space charge region of the semiconductor and the defect states at the semiconductor/insulator interface induced an insulator voltage drop (V_i), leading to a diminished ϕ_b. The Linic group further explored this by fabricating an Ir/HfO$_2$/n-Si MIS-based system to examine how these parameters (n and ϕb) influence photovoltage. The thickness of the HfO$_2$ layer did not affect the V_{fb}, which remained around 630 mV across all photoelectrodes. However, the highest measured photovoltage was only 480 mV,

about 150 mV below V_{fb} (Fig. 18b). The ideality factor for each sample was determined by evaluating the open-circuit voltage at various light intensities (Fig. 18c). There were significant

nonidealities and lower ϕ_b in the practical MIS photoelectrodes which could lead to increase the electron-hole recombination
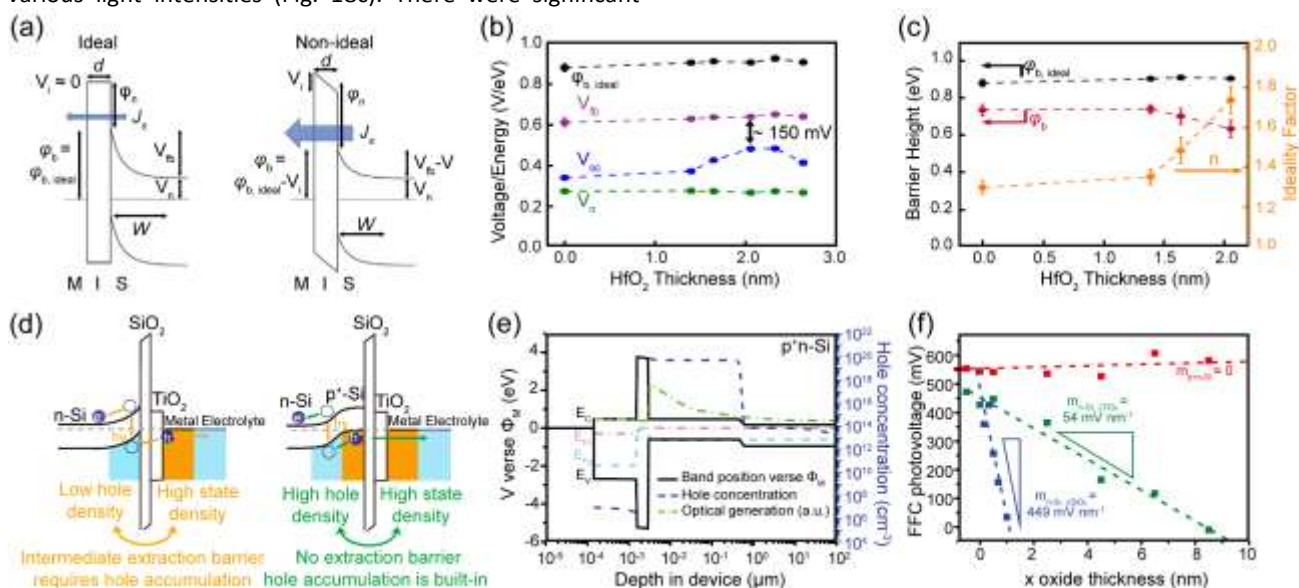

Fig. 18 (a) Energy band diagrams at equilibrium in the dark for an ideal MIS system (n = 1, left) and a nonideal MIS system (n > 1, right). Reproduced from ref. 265 with permission from the John Wiley and Sons, copyright 2020. (b) $\phi_{b,ideal}$, V_{fb}, V_{oc}, and V_n for Ir/HfO$_2$/n-Si photoelectrodes with varied HfO$_2$ thickness; (c) $\phi_{b,ideal}$, ϕ_b, and n for Ir/HfO$_2$/n-Si photoelectrodes with varied HfO$_2$ thickness. Reproduced from ref. 144 with permission from the American Chemical Society, copyright 2021. (d) Energy band diagrams of MIS-based photoanodes featuring n-Si (left) and p$^+$n-Si (right) semiconductor layers, highlighting the extraction barrier imposed by the insulator layer; (e) Simulated band diagrams of MIS-based photoanodes with p$^+$n buried junction; (f) FFC photovoltages for the (x + 1.5) nm TiO$_2$/~1.3 nm SiO$_2$/p$^+$nSi (red squares), (x + 1.5) nm TiO$_2$/~1.3 nm SiO$_2$/nSi (green squares), and 1.5 nm TiO$_2$/(x + 1.3) nm SiO$_2$/nSi (blue squares) samples plotted as a function of increasing oxide insulator thickness. Reproduced from ref. 170 with permission from the Springer Nature, copyright 2015.

probabilities. While an optimized ultrathin insulator layer can effectively regulate carrier flux and facilitate electron-hole separation, the introduction of additional interface states in the MIS system diminishes the intrinsic barrier height between the semiconductor and cocatalyst. The Linic group conducted a comprehensively quantitative analysis of photovoltage losses in MIS systems, which offered valuable insights for designing efficient and stable MIS photoelectrodes by optimizing the insulator layer thickness, enhancing light absorption, mitigating nonidealities, and exploring the incorporation of diverse insulator layers to enhance carrier selectivity.[144,150,265] The McIntyre research group reported that the insulator layer created a charge extraction barrier causing photovoltage losses.[170] They effectively mitigated this influence by incorporating a heavily doped surface buried layer to increase the minority carrier density at the semiconductor/insulator interface and achieved a remarkable photovoltage of 630 mV. As shown in Fig. 18d, while metal-based cocatalysts enhanced the state density and facilitated carrier transfer from the semiconductor to the electrolyte, efficient minority carrier extraction necessitated moderate carrier accumulation at the semiconductor/insulator interface. Incorporating a p$^+$ layer on the semiconductor surface ensured a high concentration of holes, maintaining an inversion layer for minority carriers and filling interface states to prevent carrier recombination. The simulated band diagram demonstrated that the buried junction

p$^+$n-Si substrates exhibited a high hole density of ~5×10^{19} cm^{-3} at the interface and a junction depth under 1 μm (Fig. 18e). Photovoltage proved independent of insulator layer thickness in MIS photoelectrodes with a p$^+$n buried junction (Fig. 18f).

In addition to regulating the semiconductor/insulator interface, selecting metal-based cocatalysts with appropriate work functions is key for optimizing the insulator/cocatalyst interface and forming a Schottky junction with the semiconductor layer. Simultaneously, addressing the Fermi-level pinning phenomenon at these interfaces should also be a key focus. In n-type semiconductor photoanodes, metal-based cocatalysts with high work functions are preferred. This promotes the formation of an inversion layer on the semiconductor surface, establishing a barrier height capable of repelling majority carriers and facilitating the selective minority carrier transfer, which is essential for high photovoltage. Similarly, for p-type semiconductor photocathodes, metal-based cocatalysts with low work functions are typically preferred. Digdaya et al. incorporated Al$_2$O$_3$ as an effective passivation layer in combination with SiO$_x$ as the tunneling insulator layers.[152] This approach mitigated the Fermi-level pinning effect and raised the barrier height to improve photovoltage. Furthermore, the authors employed bimetallic layers of Pt/Ni where the Pt layer with a high work function formed Schottky junctions and the Ni layer with high catalytic activity facilitated water oxidation. As illustrated in the energy

band diagram of n-Si/SiO$_{x,RCA}$/Al$_2$O$_3$/Pt/Ni (Fig. 19a), the Ni layer underwent transformation into NiO$_x$/Ni(OH)$_2$ during an 18-hour aging process in KOH, resulting in a higher work function range of 5.2-5.6 eV. Despite a 2 nm Pt layer partially shielding of the
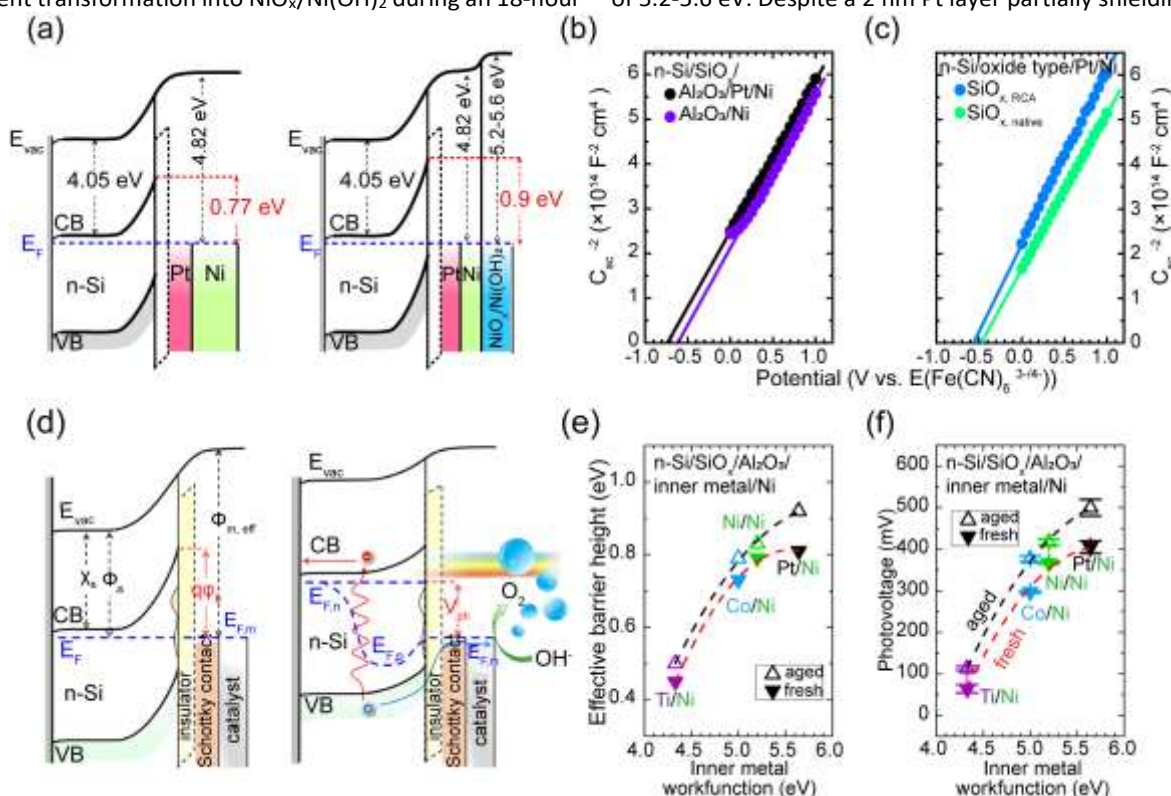

Fig. 19 (a) Energy band diagrams of the fresh n-Si/SiO$_{x,RCA}$/Al$_2$O$_3$/Pt/Ni photoelectrode (left) and that after an 18-hour aging process in KOH (right); (b) Mott–Schottky plots of n-Si/SiO$_{x,RCA}$/Al$_2$O$_3$/Pt (2 nm)/Ni (4 nm) and n-Si/SiO$_{x,RCA}$/Al$_2$O$_3$/Ni (6 nm); (c) Mott–Schottky plots of n-Si/SiO$_{x,RCA}$/Pt/Ni and n-Si/SiO$_{x,native}$/Pt/Ni. Reproduced from ref. 152 under the terms of the CC-BY 4.0 license, copyright 2017, The Authors, published by the Springer Nature. (d) Energy band diagram of MIS-based photoanodes in the dark and under illumination; (e) Effective barrier height as a function of the inner metal work function of n-Si/SiO$_x$/Al$_2$O$_3$/'inner metal'/Ni photoanodes; (f) Photovoltage as a function of the inner metal work function of n-Si/SiO$_x$/Al$_2$O$_3$/'inner metal'/Ni photoanodes. Reproduced from ref. 266 under the terms of the CC-BY 4.0 license, copyright 2018, The Authors, published by the American Chemical Society.

charge on the Si interface, the work function alteration the outer metal layer raised the barrier height from 0.77 eV to 0.9 eV, which in turn contributed to enhancing the photovoltage from 400 mV to 490 mV. The Mott-Schottky diagram of the MIS photoelectrode with Pt/Ni bimetallic and Ni single layers shows a flat band potential shift from −0.6 to −0.73 V versus Fe(CN)$_6^{3-/4-}$ (Fig. 19b). This emphasized the work function of the inner metal in determining the effective barrier height. Without the Al$_2$O$_3$ insulator layer, photovoltages dropped to 310 mV and 230 mV for SiO$_{x/RCA}$ and SiO$_{x/native}$ photoelectrodes, respectively. Despite the high work function of the inner Pt layer, the n-Si/SiO$_x$/Pt/Ni photoanode exhibited a relatively low photovoltage, which could be attributed to the strong Fermi-level pinning at the Si/SiO$_x$ interface. Notably, the Fermi-level pinning worsened with SiO$_{x/native}$ compared to SiO$_{x/RCA}$, as indicated by a lower barrier height in n-Si/SiO$_{x/native}$/Pt/Ni photoelectrode (Fig. 19c). Subsequently, Digdaya *et al.* examined the effect of varying bimetallic layer work functions on the Schottky barrier height in the MIS junction.[266] Fig. 19d illustrates that the Schottky barrier in the MIS structure arises from the work function difference between the metal (Φ_m) and

the semiconductor (Φ_s). However, interface states modify the effective work function of the metal ($\Phi_{m,eff}$) in the MIS structure compared to its value in vacuum. When exposed to light, the quasi-Fermi energy level of holes near the interface shifts upward due to carrier recombination, contributing to the photovoltage loss. As shown in Fig. 19e, varying the work function of the inner metal modulates the effective barrier height of MIS photoanodes. The photovoltage of n-Si/SiO$_x$/Al$_2$O$_3$/'inner metal'/Ni photoanodes correlated positively with the increment of the inner metal work function. The aforementioned experimental findings underscore the importance of regulating metal work functions in enhancing MIS photoelectrode performance.

6.2 Carrier-transfer through the conduction/valence band

While employing ultrathin insulator layers demonstrates broad applicability and effective protection for MIS photoelectrodes, precise control of the layer thickness at the subnanometer scale is imperative to preserve efficient charge carrier tunnelling. As the insulator layer thickness increases, the probability of minority carriers transporting highly resistive oxide layers

decreases exponentially due to scattering effects, impairing photoelectrode performance.[267]. Alternatively, the ultrathin insulator layer may suffer from manufacturing defects, such as pinholes, which can compromise the long-term stability of the photoelectrodes. Hence, investigating the thicker insulator layers and exploring new novel carrier transport mechanisms are essential for developing efficient and stable MIS photoelectrodes. The Chorkendorff group successfully deposited a 100 nm thick TiO_2 insulator layer via sputtering and observed that the introduction of this thick TiO_2 protective layer did not compromise the overpotential and photovoltage.[268,269] Subsequent energy band diagram analyses, utilizing the

Fe(II)/Fe(III) redox couple, suggested that this effect was due to the TiO_2 conduction band aligning with the hydrogen evolution potential, thereby facilitating photogenerated electron transport. This investigation elucidated a novel carrier transport mechanism through the conduction band of the insulator layer, addressing the conductivity issue in thick insulator layers for MIS photoelectrodes (Fig. 20a). Compared to tunnelling mechanism, carrier transport through the energy band of the insulator layer exhibits selective carrier type properties. Owing to the specific electronic structure of wide-bandgap oxide materials, they typically exhibit n-type semiconductor
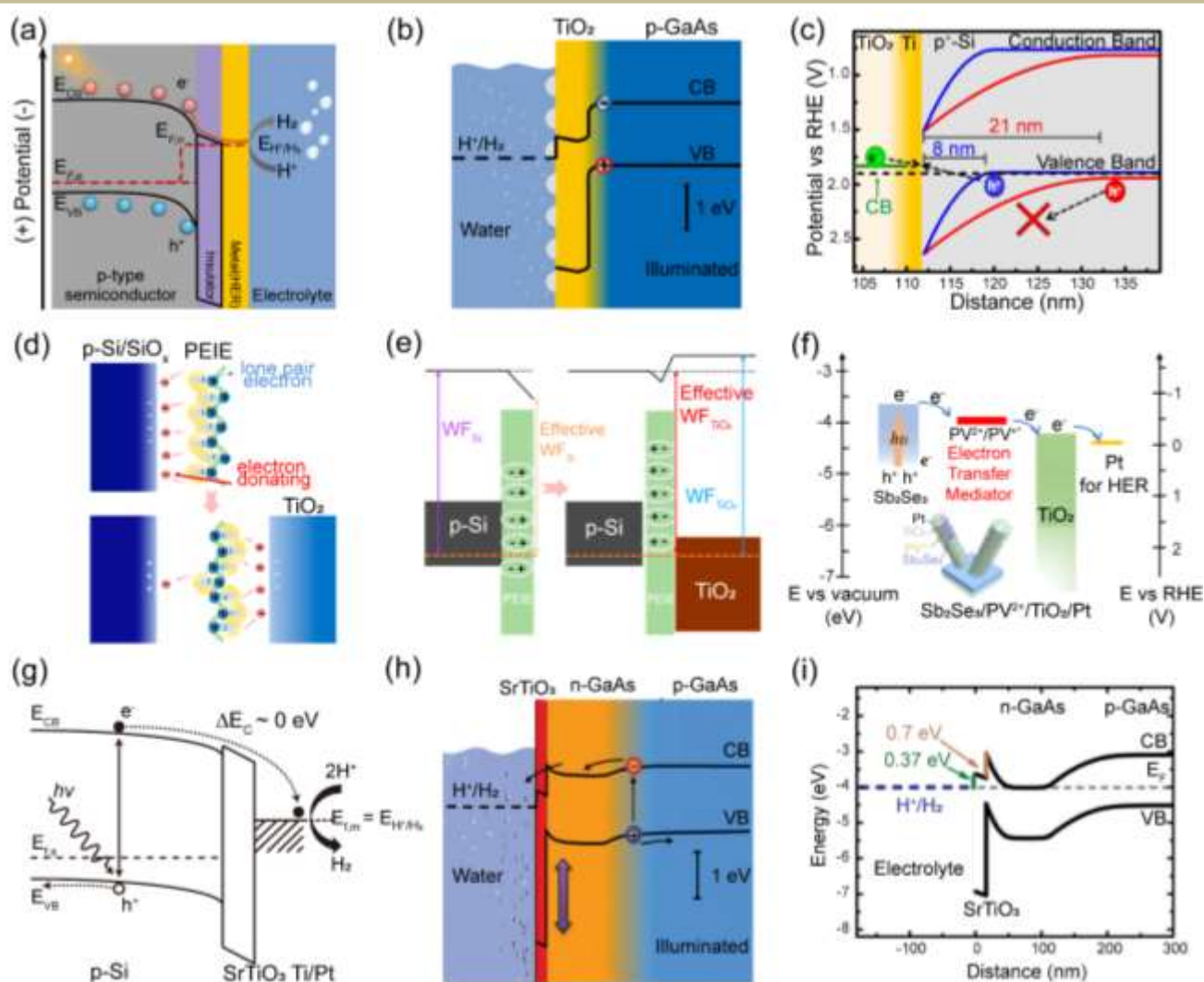

Fig. 20 (a) Schematic illustration of band diagrams showing conduction band-based carrier transport mechanism of MIS-based photocathode. (b) Energy band diagrams of p-GaAs/TiO_2/Pt photocathode under illumination. Reproduced from ref. 274 with permission from the John Wiley and Sons, copyright 2020. (c) Energy band Diagrams of an np+-Si/5 nm Ti/100 nm TiO_2/Pt Film photoelectrode under illumination. Reproduced from ref. 146 with permission from the American Chemical Society, copyright 2015. (d) Schematic illustration of the dipole reorientation strategy mechanism; (e) Energy level diagram of p-Si/PEIE (left) and p-Si/PEIE/TiO_2 (right). Reproduced from ref. 281 with permission from the American Chemical Society, copyright 2022. (f) Energy band diagrams of the Sb_2Se_3/PV^{2+}/TiO_2/Pt photocathode. The inset image is the schematic structure of the Sb_2Se_3/PV^{2+}/TiO_2/Pt photocathode. Reproduced from ref. 283 under the terms of the CC-BY 4.0 license, copyright 2022, The Authors, published by the Elsevier. (g) Energy band diagrams of p-Si/$SrTiO_3$/Ti/Pt photocathode. Reproduced from ref. 21 with permission from the Springer Nature, copyright 2014. (h) Schematic structure of the np-GaAs/$SrTiO_3$ photocathode under illumination; (i) Energy band diagrams

ARTICLE

characteristics and high electron mobility. However, achieving p-type doping and high hole mobility in these materials is challenging. The challenge arises from the valence band maximum of oxides, predominantly composed of anisotropic and localized oxygen 2p orbitals, leading to a narrower valence band dispersion and more negative valence band level.[270,271] This localization increases the effective mass of holes, resulting in reduced hole mobility, while the large valence band offset between the semiconductor layer and the insulator layer also hinders the effective transport of holes. Additionally, oxides tend to form anion vacancy defects acting as electron donors, which can annihilate holes.[272] Consequently, the energy band-based transport mechanism is more suitable for MIS photocathodes, particularly in undoped oxide protective layers. Campet et al. observed that for undoped SrTiO₃ layers thicker than 2 nm, the n-GaAs/SrTiO₃ heterojunction showed negligible photocurrent response.[273]

GaAs exhibits exceptional carrier mobility and a narrow band gap, rendering it highly suitable for utilization as the semiconductor layer in MIS photoelectrodes. However, its practical application is limited by a narrow stability window. Cao et al. employed ALD to deposit a thick TiO_2 (26 nm) protective layer onto the GaAs surface, enhancing its overall protection.[274] As depicted in Fig. 20b, the characteristic type II band alignment between p-GaAs and n-type TiO_2 offered a reliable pathway for efficient carrier transport. The GaAs photoelectrode with a thin TiO_2 (3 nm) protective layer suffered a steep photocurrent drop to 25% of its initial value within 10 hours due to surface oxidation. In contrast, the photoelectrode with a thick TiO_2 protective layer experienced a 19.8% photocurrent reduction after continuous operation for 60 hours. These results demonstrated a thick insulator layer significantly improved the corrosion resistance of the semiconductor layer. Copper-based metal oxides, known as p-type semiconductors, offer adjustable band gaps and favorable band edge potentials, while also being environmentally friendly.[111] Among them, Cu_2O has been demonstrated as a highly effective photocathode. Nonetheless, its application in PEC water splitting is hindered by chemical instability that Cu_2O tends to reduce to Cu when exposed to light and bias in the electrolyte. Depositing an n-type semiconductor protective layer on the Cu_2O surface addresses its stability issues and forms a p-n heterojunction which could enhance the transport of minority carriers. TiO_2, a widely researched n-type semiconductor, is a favored protective layer for Cu_2O. Nonetheless, its inherent sluggish reaction kinetics and the substantial conduction band offsets with Cu_2O result in the Cu_2O/TiO_2 heterojunction photocathode exhibiting low photocurrent and photovoltage.[168,275] Paracchino et al. revealed that a solitary TiO_2 layer failed to sustain the long-term stability of Cu_2O, leading to a complete depletion of its photocurrent within just 20 minutes.[113] To enhance this, a highly efficient Cu_2O-based MIS photocathode was developed by integrating Al-doped ZnO, known for its high electron mobility, as an intermediary protective buffer layer between Cu_2O and TiO_2. Although the photocurrent has been greatly improved (7.6 mA

cm⁻² at 0 V *vs.* RHE), the onset potential remains suboptimal (~0.5 V *vs.* RHE). The difference in the quasi-Fermi levels between holes in Cu_2O and electrons in the n-type oxide layer constrains the achievable photogenerated voltage of a Cu_2O-based heterojunction devices.[276] Hence, the choice of a suitable n-type protective layer that can augment the Fermi-level difference is pivotal for attaining enhanced photovoltaic performance. Dai et al. introduced ZnS as a buffer layer to increase the photovoltage of Cu_2O-based photocathode to 0.72 V.[277] Drawing inspiration from the design of Cu_2O-based heterojunction solar cells, Li et al. chose Ga_2O_3 as a buffer protective layer, owing to its electron affinity akin to that of Cu_2O.[153] This selection diminished the discontinuity in the conduction band at the Ga_2O_3/Cu_2O interface which mitigated interfacial carrier recombination and enhanced the onset potential to 1.02 V (*vs.* RHE). Pan et al. employed a similar strategy to construct an all Earth-abundant Cu_2O nanowire photocathode ($Cu_2O/Ga_2O_3/TiO_2/NiMo$), exhibiting a photocurrent density of 10 mA cm⁻² (0 V *vs.* RHE) and a photovoltage of 1.0 V.[278] Hence, judiciously selecting the buffer layer is key to achieving optimal energy band alignment within multi-layered heterostructures, thereby enhancing the overall efficiency of the photoelectrode. As previously discussed, the energy band-based carrier transport mechanism is predominantly utilized in MIS photocathodes due to the scarcity of p-type semiconductors. Nevertheless, given the critical need to develop effective photoanode protection strategies, broadening the use of thick insulator layers in MIS photoanodes is of significant importance. Mei et al. showcased the utilization of intrinsically doped n-type TiO_2 films as the insulator layer in MIS photoanodes.[146] As illustrated in Fig. 20c, the alignment of the conduction band of TiO_2 with the valence band of the silicon semiconductor layer facilitated the transport of electrons generated from the water oxidation reaction. These electrons traversed the conduction band of TiO_2 to the Si/TiO_2 interface, where they recombine with photogenerated holes from silicon. This study presents a novel approach for the advancement of thick insulator layers in MIS photoanodes.

Optimal energy band alignment at the heterojunction interfaces is key for improving MIS photoelectrodes the conduction/valence band carrier transport mechanism. Various strategies for band alignment engineering, including interface modifications and the incorporation of functional intermediary layers, have been employed to finely tune the energy band alignment between semiconductor light-absorbing layers and insulator protective layers.[27] The incorporation of a dipole interlayer is a critical interfacial engineering strategy that has shown great success in solar cells.[279,280] This creates an internal electrostatic field, significantly shifting the electronic band structure at these interfaces and effectively modulating carrier transport. The Tilley group implemented a tunable phosphoric acid (PA) molecular dipole layer at the Si/TiO_2 interface to deliberately adjust band positions, boosting the photovoltage in MIS photoelectrodes.[167] Through a combination of DFT calculations and XPS characterization, the authors

demonstrated a difference in the electron-withdrawing/donating nature of phosphate shifting the vacuum energy level downward and enhancing band bending in the semiconductor. The dipole effect amplified with the PA dipole layer thickness, but inherent resistance in PA layers capped its impact, leading to a maximum 200 mV rise in photovoltage at a 2 nm thickness. The effectiveness of the dipole strategy is not only influenced by the thickness of the dipole layer but also by the thickness of adjacent layers. Yun *et al.* introduced a dipole reorientation strategy that involved manipulating the thickness of the TiO_2 layer, which significantly enhanced the flexibility and adaptability of the dipole strategy.[281] The dipole polymer (PEIE), containing amino groups, favored interaction with TiO_2 due to its higher dielectric constant compared to Si and SiO_2, causing a notable redirection of the net dipole moment (Fig. 20d). The interaction of amine groups with lone pair electrons and TiO_2 induced the negative charges on the TiO_2 surface which raised its band edge and increased band bending relative to the silicon substrate (Fig. 20e). Inspired by the efficient Z-Scheme electron transport chain in natural photosynthesis, which achieves nearly 100% quantum efficiency due to the synergistical working between PS II and PS I,[282] inserting an electron transport intermediary layer between the semiconductor layer and the thick insulation layer offers a way to modulate the interface band alignment. The Sun group employed a viologen-containing polymer layer (PV^{2+}) as an electron transfer mediator to address the significant conduction band offsets at the Sb_2Se_3/TiO_2 junction.[283] The viologen group (V^{2+}) exhibited exceptional electrochemical redox properties, capturing photogenerated electrons to form cationic radicals ($V^{+\cdot}$), which could be readily reoxidized to V^{2+} at a defined potential, facilitating electron injection into the TiO_2 conduction band and enabling efficient carrier transport. As depicted in Fig. 20f, the ideal conduction band offset (~0.2 eV) replaced the significant electron transport barrier (~0.48 eV) present at the Sb_2Se_3/TiO_2 junction after the introduction of the PV^{2+} electron transport mediator, facilitating the smooth transfer of photogenerated electrons to the Pt cocatalyst layer.

Strontium titanate, $SrTiO_3$ (STO), is another alternative thick insulator layer for traditional PV-grade semiconductors. Due to the minimal conduction band offset between Si and STO, photogenerated electrons can efficiently transport through the conduction band of STO. Ji *et al.* employed MBE to deposit an epitaxial STO insulator layer on the surface of p-Si where the resulting STO layer exhibited excellent crystallinity and atomic smoothness.[21] Meanwhile, a minor lattice mismatch of −1.7% between STO and Si reduced interface state density. This high-quality electrical interface, coupled with the nearly zero conduction band offset between STO and the Si substrate (Fig. 20g), facilitated efficient electron transfer and minimized carrier recombination at the Si/STO interface. Consequently, the p-Si/STO/Ti/Pt MIS photocathode achieved a high photocurrent density of 35 mA cm^{-2} and an applied bias photon-to-current efficiency (ABPE) of 4.9%. As illustrated in Fig. 20h, Kornblum *et al.* applied a similar approach to epitaxially growing a 16 nm single-crystal STO as an insulator layer on np-GaAs substrates, leading to a high-performing GaAs-based

photocathode with 100% Faradaic efficiency for hydrogen evolution and an IPCE over 50%.[284] Unlike the significant valence band offsets at the GaAs/STO interface, the conductive band alignment facilitated the efficient photogenerated electrons transfer. Additionally, the conduction band edge of STO exceeded the HER energy level by 0.37 eV, thereby providing a more substantial thermodynamic driving force for the HER process (Fig. 20i).

6.3 Carrier-transfer through the constructed defect states or intermediate band

The carrier-transfer mechanism through the intrinsic conduction/valence band of the insulator layer necessitates the precise selection of insulator materials that exhibit suitable energy band alignment with the semiconductor layer. This requirement significantly restricts the choice and application of insulator materials, particularly when it comes to the scarcity of thick insulator layers that possess favourable hole conductivity for the protection of n-type semiconductor photoanodes.[285] Consequently, the development of a more versatile carrier-transfer mechanism is of paramount importance for enabling the widespread utilization of thick insulator layers in MIS photoelectrodes. Hu and Lewis *et al.* utilized the ALD method to deposit TiO_2 layers of varying thickness (4-143 nm) on n-Si.[18] Surprisingly, these photoanodes exhibited comparable performance under 1.25-Sun solar illumination, yielding a photocurrent of 34.7 ± 1.7 mA cm^{-2}, regardless of the TiO_2 thickness. The researchers attributed this phenomenon to the presence of electric defects within the TiO_2 films, which arose from disordered structures or impurities introduced during the ALD process, as verified by XPS valence-band spectra. These electric defects imparted high hole conductivity in TiO_2 films, enabling efficient photogenerated holes transfer through the defect states (Fig. 17c). The Lewis group demonstrated efficient and stable performance with GaAs and GaP-based photoelectrodes protected by these "leaky" TiO_2 films. This highlighted the scalability of this method and offered a promising protective strategy for semiconductor materials with suitable band structures yet inherently unstable, such as II–VIs, III–Vs, or metal oxides,[286-288] in PEC water splitting systems. Subsequently, The Lewis research group conducted an in-depth investigation into the carrier-transfer mechanism of the leaky TiO_2 films using electron paramagnetic resonance (EPR) and photoelectron spectroscopic characterization methods.[289] EPR spectra confirmed Ti^{3+} states in ALD-grown TiO_2, correlating positively with film conductivity. The formation of Ti^{3+} states was attributed to transferring the excess electrons of oxygen vacancy defects to adjacent Ti atoms, previously evidenced by STM characterization.[290] Moreover, temperature-dependent conductivity of MIS-based solid-state devices incorporating leaky TiO_2 films followed Arrhenius behavior, supporting the hypothesis that the carrier-transfer mechanism mainly involved polaron hopping between Ti^{3+} and adjacent Ti^{4+} sites, rather than through the conduction or valence bands.

Further insights into the electrical behavior and energy band structure of diverse heterojunction interfaces incorporating the leaky TiO_2 films could enhance MIS photoelectrode

ARTICLE

performance and broaden the applicability of the leaky TiO_2 protective layers. Hu et al. conducted comprehensive characterizations of the energy band alignment of the semiconductor/leaky TiO_2 heterojunction interface using XPS and ultraviolet photoelectron spectroscopy (UPS).[291] Their efforts resulted in a detailed energetics map for the heterojunction interface (Fig. 21a-c), enabling a thorough analysis of the impact of semiconductor doping concentration and type on the energy band structure. The SiO_x 2p core-level binding energy of the silicon oxide layer at the interface of the three semiconductors (n-Si, n^+-Si, and p^+-Si)/TiO_2 exhibited significant shifts before and after TiO_2 deposition. This change was likely due to a reduction in the chemical shift of Si^{4+} 2p, linked to the formation of a $Si_xTi_yO_2$ mixed oxide layer. As shown in Fig. 21a and 19b, both n-Si and n^+-Si experienced upward band bending as ALD deposition proceeded, indicating the formation of an electrically rectifying junction between the semiconductor layer and TiO_2 films. The band bending in highly doped n^+-Si (0.11 eV) is smaller compared to that in n-Si (0.40 eV). In contrast, no energy band bending was observed in the p^+-Si substrate and the Fermi levels of Si and TiO_2 achieved equilibrium (Fig. 21c), resulting in an ohmic tunnel junction.

Furthermore, the interfacial conductivity of the MIS photoelectrodes is also influenced and controlled by the heterojunction interfaces between the leaky TiO_2 and metal layers. Lichterman et al. employed ambient-pressure XPS to directly investigate the semiconductor/liquid junction and demonstrated that the deposition of Ni on the leaky TiO_2 surface altered the electrical behavior of the solid/liquid junction from rectifying to ohmic, thereby effectively eliminating the energy barrier for carrier transport.[292] Nunez et al. investigated how metals with different work functions affected the electrical properties of p^+-Si/leaky TiO_2/metal photoelectrodes. They observed that the contact resistance increased with the metal work function.[289] Furthermore, the current densities of devices with high metal work functions (φ $>$ 4.7 eV) were found to be less than or equal to 10% of that of devices with low metal work functions. Notably, the p^+-Si/leaky TiO_2/Ni ($φ_{Ni}$ = 5.1 eV) was an exception whose J-V characteristic behavior exhibited similarity to that of devices with low metal work functions. Richter et al. observed similar trends when further investigating the interaction between metal layers and amorphous leaky TiO_2 films.[293] At the TiO_2/Ni interface (Fig. 21d), modest work function differences resulted in a slight
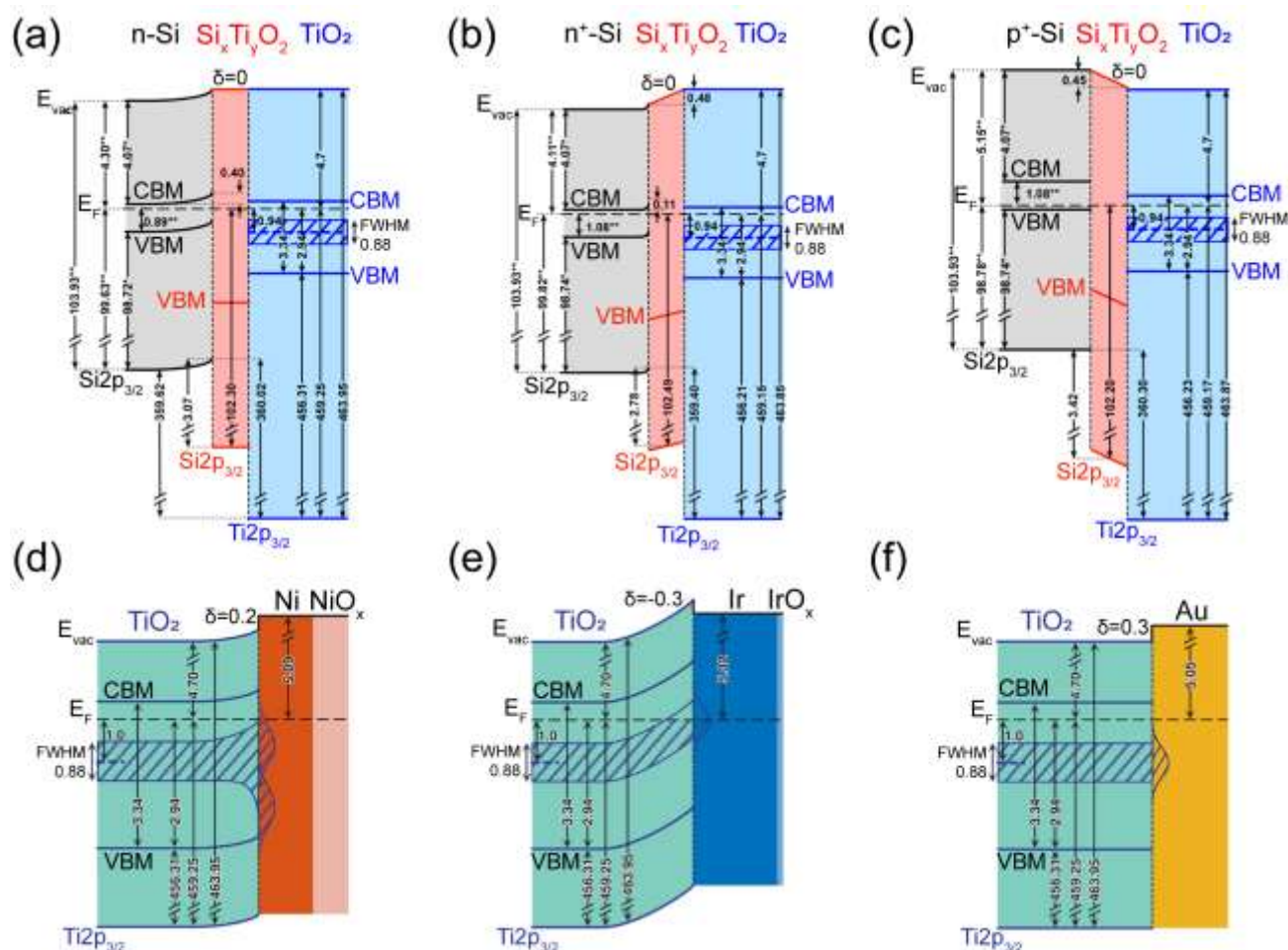

Fig. 21 (a-c) Energy band diagrams of the heterojunction interfaces between three different semiconductor substrates and the leaky TiO_2, from left to right: (a) n-Si/TiO_2, (b) n^+-Si/ TiO_2, and (c) p^+-Si/TiO_2. Reproduced from ref. 291 with permission from the American Chemical Society, copyright 2016. (d-f) Energy band diagrams of the heterojunction interfaces between the leaky TiO_2

and three metal layers with different work functions, from left to right: (d) $TiO_2/Ni/NiO_x$, (e) $TiO_2/Ir/IrO_x$, and (f) TiO_2/Au. Reproduced from ref. 293 with permission from the American Chemical Society, copyright 2021.

upward band bending, that could facilitate the efficient hole transfer. Furthermore, the interaction between TiO_2 and Ni also introduced a second defect state, increasing defect state density and creating a quasi-metallic ohmic contact at the leaky TiO_2/Ni junction. Conversely, at the leaky TiO_2/Ir heterojunction interface (Fig. 21e), a notable upward bending of defect bands occurred due to the significant work function difference between the two materials. Electrons occupying the defect states above the Fermi level underwent depletion to cause the transformation of Ti^{3+} to Ti^{4+}. As a result, the concentration of Ti^{3+} at the interface diminished which could hinder efficient carrier transport. For Au with non-catalytic activity and high work function, the defect band at the TiO_2/Au interface remained in a flat band state, which hindered carrier transport due to insufficient driving electric fields (Fig. 21f).

While prior discussions chiefly addressed the effects of heterojunction interfaces with amorphous leaky TiO_2 on MIS photoelectrode performance, modifying the material properties and electrical characteristics of TiO_2 films through preparation or post-treatment methods also critically impacts photogenerated carrier transport. McDowell et al. explored the impact of post-thermal annealing treatment on the properties of the thick TiO_2 protective layer and photoelectrode performance.[294] Annealing below 500 °C resulted in the transformation of the amorphous TiO_2 films into polycrystalline anatase structures. The polycrystalline samples displayed J-V characteristics comparable to the photoelectrodes with amorphous TiO_2 films, suggesting effective carrier transport even in crystalline structures. Furthermore, annealing the photoelectrodes in a reducing forming gas atmosphere significantly boosted photovoltage, attributed to enhanced band bending and fewer defect recombination centers in polycrystalline TiO_2 layers.[295] The photoelectrode performance declined when annealing exceeded 600°C, mainly due to the emergence of the rutile phase reducing the conductivity of TiO_2 films. Additionally, the increased thickness of the SiO_x interface layer introduced greater tunneling resistance, further hindering charge transport. Zheng et al. introduced a facile method for fabricating crystalline TiO_2 films featuring a gradient of oxygen vacancies. This innovation enabled MIS photocathodes to achieve both a high current density (35.3 mA cm^{-2}) and
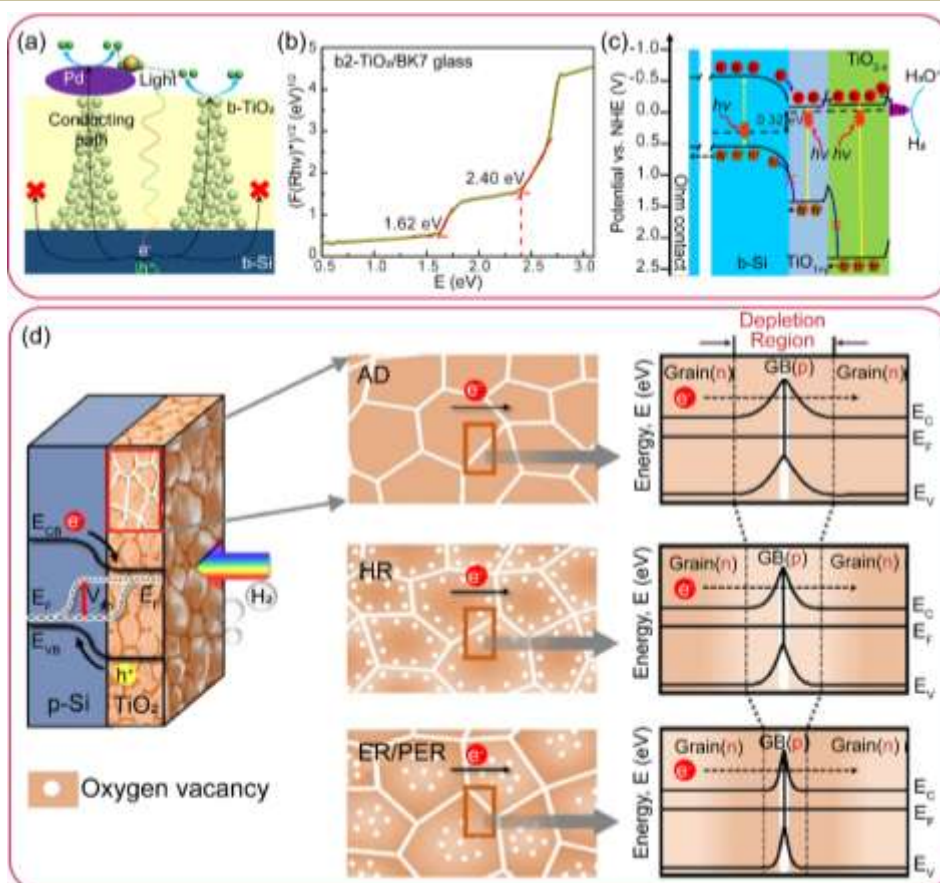

Fig 22 (a) Schematic structure of the b-Si/black TiO_2/Pd photocathode; (b) Energy band diagrams of the b-Si/black TiO_2/Pd photocathode; (c) The optical absorption coefficient as a function of the incident photon energy for b2-TiO_2/BK7 glass. Reproduced from ref. 214 under the terms of the CC-BY 4.0 license, copyright 2018, The Authors, published by the Springer Nature. (d) Schematic structure of the p-Si/TiO_2 photocathode (left). Schematic model of oxygen vacancies spatial distribution (middle) and potential-energy diagram (right) of the as-deposited crystalline TiO_2 (AD) and that treated with three different reduction methods,

ARTICLE

including hydrogen reduction (HR), electrochemical reduction (ER), and photoelectrochemical reduction (PER). Reproduced from ref. 297 with permission from the John Wiley and Sons, copyright 2020.

remarkable stability (>100 hours) in 1.0 M NaOH.[214] The gradient oxygen defects acted as conductive channels to facilitate the carriers' transport through the TiO_2 layer (Fig. 22a). As shown in Fig. 22b, the diffuse reflectance absorption spectrum of crystalline TiO_2 revealed the presence of two distinct absorption bandgaps (1.62 eV and 2.40 eV), indicating the existence of two Ti:O stoichiometric compositions in the TiO_2 film (TiO_{1+y} and TiO_{2-x}). The energy band diagram of the photoelectrode (Fig. 22c) illustrated that photogenerated electrons efficiently traversed the crystalline TiO_2 layer, whereas holes encountered a significant potential barrier for hindering their transport through the TiO_2 layer. Although the crystalline TiO_2 protective layer offers versatile means to adjust the interface energy properties of MIS photoelectrodes, it can introduce grain boundaries (GBs), resulting in the generation of excessive recombination centers.[296] The Gong group implemented a controlled spatial distribution of oxygen vacancies in crystalline TiO_2 to enhance carrier transport and minimize carrier recombination at GBs.[297] Three reduction approaches, including hydrogen reduction (HR), electrochemical reduction (ER), and photoelectrochemical reduction (PER), could be used to create varied oxygen vacancy distributions in the crystalline TiO_2. The rapid adsorption of H_2 molecules along GBs led to the distribution of oxygen vacancies mainly along GBs in TiO_2-HR samples. On the other hand, ER/PER processes were governed by the reduction current, favoring occurrence in grain domains with lower resistivity, which resulted in the distribution of oxygen vacancies in the grains (Fig. 22d). The distinct electronic structure between GBs and grains resulted in the free electrons in the grains being trapped by the localized energy states at GBs, forming an n-p-n tunnelling junction for the carrier transfer. In contrast to oxygen vacancies distributed along the GBs, the presence of oxygen vacancies inside the grains (TiO_2-ER/PER) could decrease the thickness of the depletion region, thereby facilitating electron tunnelling across GBs (Fig. 22d).

The leaky TiO_2 protection layer, relying on defect states for carrier transport, addresses the inherent trade-off between stability, transparency, and conductivity of the insulator layer,[264] which broadens the application of thick insulator layers in MIS photoelectrodes. Previous research data indicates that the defect states in ALD-grown leaky TiO_2 exhibit similar characteristic energy level structures.[291-294] Specifically, the defect band width ranges from approximately 0.83 to 0.88 eV and the defect energy level center situates approximately 1 eV below the Fermi level of the leaky TiO_2.[289] The energy level structures of the intrinsic defect states are limitedly regulated by altering the concentration of oxygen vacancies, posing challenges in jointly optimizing energetic alignment at both semiconductor/leaky TiO_2 and leaky TiO_2/metal interfaces. For the semiconductor/leaky TiO_2 interface, ensuring proximity between the conduction/valence band of the semiconductor layer and the defect states of leaky TiO_2 is vital to minimize energy conversion losses. While the leaky TiO_2 has found extensive application in silicon-based photoelectrodes, its application is constrained in semiconductors with deep valence bands energy levels due to the large energy level misalignment. For the leaky TiO_2/metal interface, the influence of metal work function on the energy band bending of the defect states should
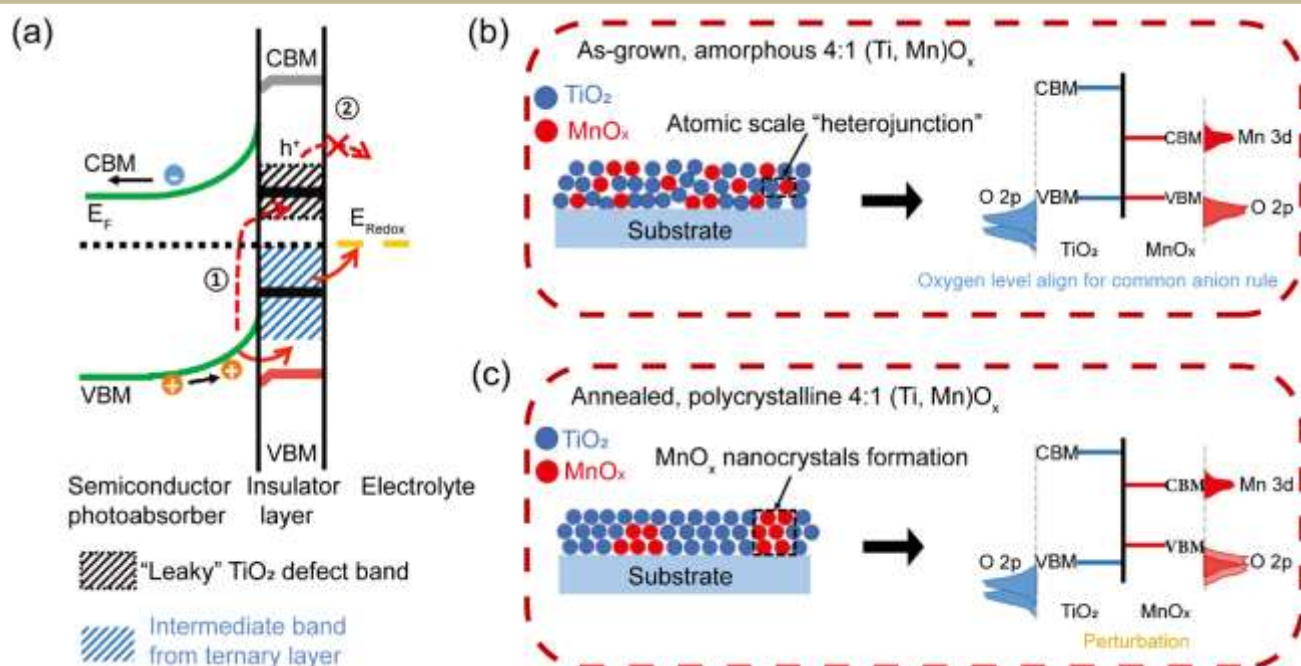

Fig. 23 (a) Schematic diagram of comparing the carrier-transfer mechanism through the defect states or intermediate band of TiO_2 films. (b) Schematic diagram of the microstructure of the as-grown (Ti, Mn)O_x film and the relative positions of energy levels in the atomic scale heterojunction. (c) Schematic diagram of the microstructure of the annealed (Ti, Mn)O_x film and the relative positions

of energy levels in the TiO_2/MnO_x nanoclusters bulk heterojunction. Reproduced from ref. 193 with permission from the John Wiley and Sons, copyright 2022.

be considered. As previously discussed, the leaky TiO_2/high-work-function metals interface tends to exhibit lower electrical conductivity, resulting in the restricted usage of high-work-function metals with commendable catalytic activities and stability, such as Ir.[289,293] Hence, advancing insulator layers featuring tunable defect state energy levels are essential for compatibility with various semiconductors and metal cocatalysts, expanding the scope of the thick insulator strategy in MIS photoelectrodes. In 1989, Camp *et al.* introduced cation valence bands into the $SrTiO_3$ insulator layer by Ce^{3+} doping, facilitating photogenerated hole transport through the n-$GaAs/SrTiO_3$ heterojunction. As a common strategy for modifying semiconductor materials, doping engineering remains an effective method for adjusting the defect states of the insulator layer.[298] The Hu group recently introduced a continuously tunable intermediate band (IB) into TiO_2 films through in-situ doping of metal cations (Mn^{2+}, Mn^{3+}, and Cr^{3+}) using ALD.[193] This approach allowed for precise tuning of the IB by varying the type and ratio of doping elements to realize the energetic alignment at both n-GaP/TiO_2 and TiO_2/IrO_x interfaces (Fig. 23a). The distinctive features of ALD allowed for the atomic dispersion of metal cations within TiO_2 films. For Mn-doped TiO_2 films (Fig. 23b), Mn atoms intricately interacted with adjacent Ti atoms through shared bridging oxygen to form an atomic heterojunction comprised of Mn-O-Ti units. The O 2p energy levels of the heterojunction aligned harmoniously and the IB of TiO_2 primarily consisted of Mn 3d orbitals. The annealing treatment could tune the position of the IB by changing the microstructure of the TiO_2 films. As illustrated in Fig. 23c, the microstructure of Mn-doped TiO_2 films varied from an amorphous structure with atomically dispersed Mn ions to a polycrystalline structure enriched with MnO_x nanoclusters. This transition established a TiO_2/MnO_x bulk heterojunction and led to an upward shift in the IB. This method offers a versatile approach for customizing the protective layer in MIS photoelectrodes, allowing for adjustable interface energy with various semiconductor light-absorbing layers, including silicon-based and III-V semiconductors. Such adaptability significantly broadens the practical applications of MIS photoelectrodes in PEC energy conversion.

6.4 Carrier-transfer through the embedded conduction pathways

Photoelectrode design faces a trade-off between stability and efficiency. The incorporation of an insulator layer undoubtedly enhances the stability of the PEC system but complicates photoelectrode design aimed at efficient carrier transport. Drawing upon the local metal contact process used in the current mainstream solar cell technology of the passivated emitter and rear cells (PERC),[299] a novel MIS photoelectrode configuration integrates conductive pathways within the thick insulator layer. The embedded conduction pathways facilitate efficient photogenerated carriers transport to the metal cocatalyst layer, while simplifying the MIS photoelectrode design by eliminating concerns over insulator layer thickness

and energy band alignment. As illustrated in Fig. 24, the top-down preparation methods employed for fabricating embedded conduction pathways in MIS photoelectrodes primarily involve the lithographic process, (photo)electrochemical process, and metal thin-film reaction process. Lithography, often used to define rear contact geometries in PERC, is also fully compatible with the fabrication of embedded conduction pathways in MIS photoelectrodes. Seo et al. utilized electron beam stepper lithography to etch cross-shaped through holes in the SiO_2 layer (Fig. 24a), followed by chemically depositing Ag into these through holes to create an embedded conduction pathway.[300] These Ag channels not only expedited electron extraction from p-Si but also improved MoS_x cocatalyst adhesion. Considering cost-effectiveness in commercial production, exploring non-lithographic methods for embedded conduction pathways is crucial. Silicon electrochemistry is widely used in device fabrication, especially for creating nanostructures.[301] A novel nanoemitter solar cell structure emerges from the self-organized formation of nanopores within the thick silicon oxide during current oscillations in fluoride-containing electrolytes.[302-304] As shown in Fig. 24b, the self-organized electrochemical process provides a facile alternative to create nanopores in oxides, which are then metal-filled through electrodeposition. The Al-SiO_2-Si MIS structure has been extensively employed in early silicon-based semiconductor devices. However, its reliability is compromised under extreme conditions like high temperatures, leading to device failure.[305] Studies identify that Al reduces the SiO_2 film at elevated temperatures, forming Al spikes that penetrate the insulating layer.[306] Nevertheless, Ho *et al.* ingeniously repurposed this Al/SiO_2 thin film reaction interaction, previously a failure mode, into a novel technique for crafting localized rear contacts in solar cells.[307,308] This cost-effective and facile technique utilized Al spikes to selectively reduce localized areas of the SiO_2 passivation layer at high temperatures (300-577 °C), resulting in the formation of ohmic contacts on the backside of the solar cell. Recently, the Yu group demonstrated a cost-effective and scalable approach for creating embedded conduction pathways via the metal/insulator thin-film reaction process.[23] As depicted in Fig. 24c, a 90 nm SiO_2 layer was first deposited onto n-Si surfaces to improve photoelectrode stability. Subsequently, the Al/SiO_2 thin-film reaction was employed to create vias within the SiO_2 layer, followed by electrochemically depositing Ni to finalize the conductive channels. The three top-down techniques for preparing embedded conduction pathways primarily rely on etching and electrochemical deposition processes. These processes may introduce chemical contaminants and pinholes in the conductive channels, leading to carrier recombination and compromising photoelectrode stability. Oh et al. observed localized silicon dissolution under the edge of the embedded conductive channel after a 24-hour stability test, likely attributed to the electrolyte penetrating into the silicon substrate through the gap between the insulator layer and the metal channel.[309] Although extending the embedded metal

channels onto the SiO₂ layer could resolve the issue of electrolyte penetration, the fabrication of photoelectrode required two photolithography processes, resulting in increased
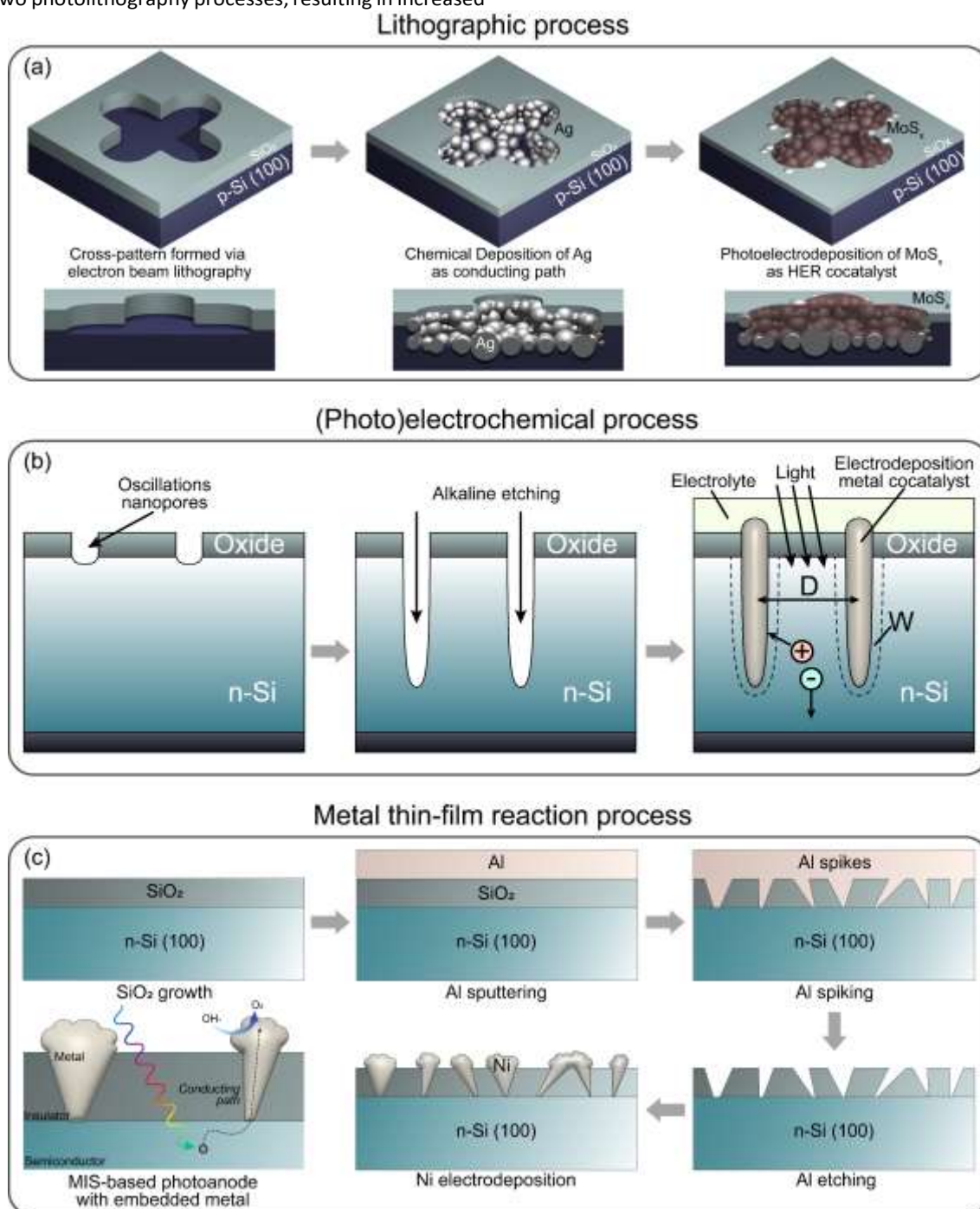

Fig. 24 Different methods of fabricating conductive pathways embedded in the insulator layers. (a) Schematic illustration of preparation procedures for the p-Si/SiOₓ/Ag/MoSₓ photocathode. The embedded cross-pattern in a 50 nm thick SiO₂ film was formed by electron beam stepper lithography. Reproduced from ref. 300 with permission from the American Chemical Society, copyright 2021. (b) Schematic illustration of preparation procedures for the nanoemitter photoelectrode. The oxide nanopores were formed by (photo)electrochemical current oscillations. Reproduced from ref. 304 with permission from the Elsevier, copyright 2008. (c) Schematic illustration of preparation procedures for the n-Si/SiO₂/Ni photoanode. The embedded metallic conduction paths were formed by thin-film reaction between Al and SiO₂ under the annealing temperatures of 450–600 °C. Reproduced from ref. 23 under the terms of the CC-BY 4.0 license, copyright 2021, The Authors, published by the Springer Nature.

costs and complexity. Ji et al. employed an external voltage to induce local dielectric breakdown within the MIS structure, resulting in the generation of embedded conductive channels.[22] Despite requiring a one-step photolithographic process, the method minimally impacted the insulator layer and displayed remarkable universality, successfully applying to insulator layers such as SiO_2, TiO_2, and Al_2O_3 without causing substantial damage.

Spontaneous segregation of metal dopants during deposition of a so-called vertically aligned nanocomposite (VAN) film by single-step PLD could yield embedded metal nanopillars within oxides matrix.[310,311] This bottom-up strategy circumvents the need for complex microfabrication or lithography processing, presenting a streamlined approach to creating embedded conduction pathways in insulator layers. Kawasaki et al. fabricated a photoanode featuring self-assembled Ir nanopillars embedded in a $SrTiO_3$ matrix substrate through precise control of the kinetics during PLD epitaxial film growth.[312] Tubular Schottky junctions surrounding the Ir nanopillars significantly enhanced carrier transport efficiency. The single-step fabrication process ensured mechanical robustness by preventing the introduction of contaminants or pinholes to the photoelectrode. Due to the significant difference in growth kinetics between metals and oxides, appropriate material combinations and parameter optimization are essential for rapid metal nucleation and coalescence into nanopillars, as opposed to the formation of isolated nanoparticles or the diffusion doping into the oxide matrix.[313] Despite limited reports on the VAN strategy for energy conversion devices, its distinctive nanostructure promises substantial utility in optimizing MIS photoelectrodes.

Given the divergent electrical properties and band structures of the components within MIS photoelectrodes, targeted interfacial regulation strategies are critical for effective band alignment and carrier migration. This section elucidates four kinds of carrier-transfer mechanisms in MIS photoelectrodes, intertwined with design principles for regulating heterogeneous interfaces. Advanced characterization techniques are pivotal for dissecting carrier dynamic behaviours and chemical states of photoelectrodes. Traditional characterization techniques are usually completed in a vacuum state and often fall short in capturing the real-time interactions of MIS photoelectrodes. Thus, the evolution toward in-situ characterization is imperative for a nuanced understanding of carrier-transport mechanisms within MIS photoelectrodes.

7. Derivative Configurations of MIS Photoelectrodes

Despite significant progress in the field of PEC water splitting over the past 50 years, numerous challenges remain before this technology can truly be commercialized. Most reported photoelectrodes have geometric areas below 50 cm^2, which is significantly smaller than the area required for large-scale applications (~1 m^2).[314] Although photoelectrode materials have been optimized at the laboratory scale, scaling up the photoelectrode area to meet commercial demands without
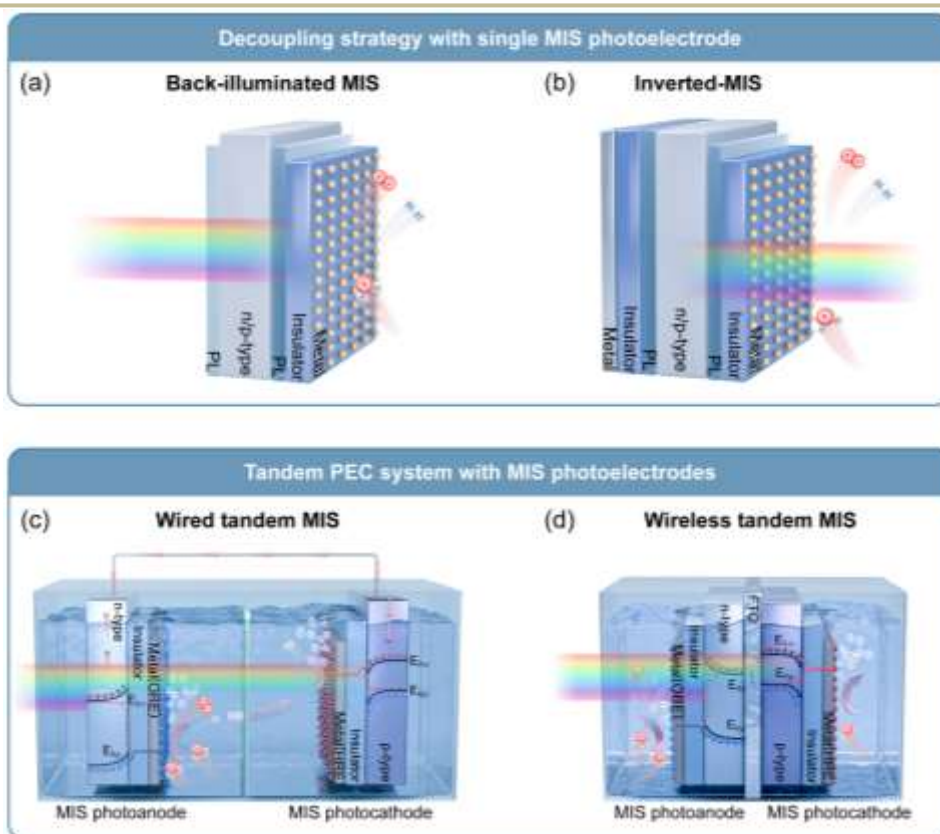
Fig. 25 Schematic illustration of derivative MIS configurations for PEC water splitting. Single MIS photoelectrodes: (a) Back-illuminated MIS photoelectrode configuration; (b) Inverted-MIS photoelectrode configuration. (PL represents an ultra-thin passivation layer.) Tandem MIS photoelectrodes: (c) Wired tandem PEC system with MIS photoelectrodes; (d) Wireless monolithic tandem PEC system with MIS photoelectrodes.

compromising performance remains a challenge. Simply increasing the PEC device area does not effectively enhance hydrogen production and may even decrease conversion efficiency.[315,316] Moreover, the stability of PEC systems is crucial for industrialization. Techno-economic analyses suggest that photoelectrodes need a service life of several years (typically 10-20 years) for cost-competitive PEC hydrogen production.[14] However, most studies have only examined the stability of photoelectrodes for a few hundred hours, far from the required service life for commercialization. To address these challenges, it is essential to optimize photoelectrode design from the perspective of configuration and system integration, building upon material development. MIS photoelectrodes, which achieve efficient light absorption, charge separation, and interface catalysis in a single device, are expected to be a breakthrough in promoting the large-scale application of PEC water splitting.

Previous chapters have detailed the key components and carrier-transfer mechanisms of MIS photoelectrodes. However, in the process of developing large-scale PEC water splitting systems, investigating isolated material components is no longer sufficient to solve the many technical challenges faced. Therefore, it is highly necessary and significant to develop innovative MIS photoelectrode configurations that effectively couple different functional modules such as light-absorbing layers, protective layers, and catalytic layer to construct efficient and stable PEC conversion systems. This approach not only improves the performance of photoelectrodes but also lays the foundation for building integrated PEC water splitting devices. Traditional MIS structures have limitations in achieving ideal light absorption, carrier collection, and catalytic processes due to the parasitic light absorption effect of the metal layer, the inability to effectively couple different light-absorbing materials, and the limited spectral response range of a single semiconductor material. To overcome these challenges, researchers have proposed a series of derivative photoelectrode configurations based on the MIS structure. These novel photoelectrode structures exhibit excellent PEC conversion performance and provide new solutions for constructing high-quality PEC water splitting systems. This section focuses on introducing two types of derivative MIS photoelectrode configurations: single MIS photoelectrodes (Fig. 25a, b) and tandem MIS photoelectrodes (Fig. 25c, d). The working principles, structural features, and recent research progress of each configuration will be discussed, summarizing the advantages of these novel structures in addressing the limitations of traditional MIS photoelectrodes. This content aims to provide a novel and holistic perspective on the future development direction of MIS photoelectrodes.

7.1 Single MIS photoelectrodes

Currently, most MIS photoelectrodes integrate key functions such as light absorption, surface protection, and catalytic reactions on the same side of the device, leading to overutilization of that side while the back side is only used for electrical connections and remains underutilized.[208] This single-sided utilization design mode causes the photoelectrode to undertake too many functions on one side, which not only increases the difficulty of device optimization but also results in efficiency losses. Furthermore, the metal layer used as a cocatalyst can cause parasitic light absorption and reflection, reducing the light intensity incident on the semiconductor and affecting the generation of photogenerated carriers. Labrador et al. studied the influence of Pt nanoparticle loading on the performance of p-Si MIS photocathodes.[317] Excessive Pt loading can lead to parasitic light absorption, reducing the light intensity incident on the Si. This highlights the critical importance of optimizing the catalyst loading to balance light absorption capacity and catalytic activity. The high-power density and omnidirectional light-harvesting capabilities of bifacial photovoltaic technology can provide new inspiration designing novel MIS photoelectrode structures to solve the aforementioned problems.[318] By simultaneously absorbing direct and ambient reflected light, the power output of bifacial cells can be increased by 50% compared to single-sided cells.[319] Researchers have proposed innovative configurations of MIS photoelectrodes such as back-illuminated (Fig. 25a) and inverted MIS photoelectrodes (Fig. 25b). By rationally designing the photoelectrode structure to spatially decouple light absorption and catalytic reaction sites, the parasitic absorption of the cocatalyst can be reduced, and the utilization of both sides of the device can be maximized to enhance light-capturing capabilities.

Due to the inherent opacity of the semiconductor layer and the limited minority carrier diffusion length, efficiently collecting photogenerated carriers and transporting them to the catalytic sites to participate in reactions is one of the primary challenges faced by back-illuminated MIS photoelectrodes. Bae et al. reported, for the first time, the photoelectrochemical performance of a p^+pn^+ silicon photoelectrode under back-illumination conditions.[269] By systematically investigating the influence of silicon thickness on the performance of back-illuminated photoelectrodes, they found that as the silicon thickness decreased from 350 μm to 50 μm, the photocurrent density of the electrode increased from 6.2 mA cm^{-2} to 17.0 mA cm^{-2}. This improvement is mainly attributed to the increased ratio of minority carrier diffusion length to device thickness (L_e/L) as a result of silicon thinning, which favors the collection of photogenerated charge carriers. This work systematically investigates the influence of light-absorbing layer thickness on the carrier collection efficiency in back-illuminated MIS photoelectrodes, providing theoretical guidance for subsequent device optimization. However, while excessive thinning of the silicon can improve carrier collection efficiency, it leads to absorption losses of long-wavelength light

and increases the complexity of device fabrication. Hence, further enhancing the carrier collection efficiency of back-illuminated MIS photoelectrodes without sacrificing light absorption capability is a noteworthy issue. Fu et al. proposed an innovative interdigitated back-buried junction (BBJ) structure to improve carrier collection efficiency in back-illuminated MIS photoelectrodes (Fig. 26a).[320] The back side of the n-Si substrate featured alternating p^+ and n^+ doped regions,
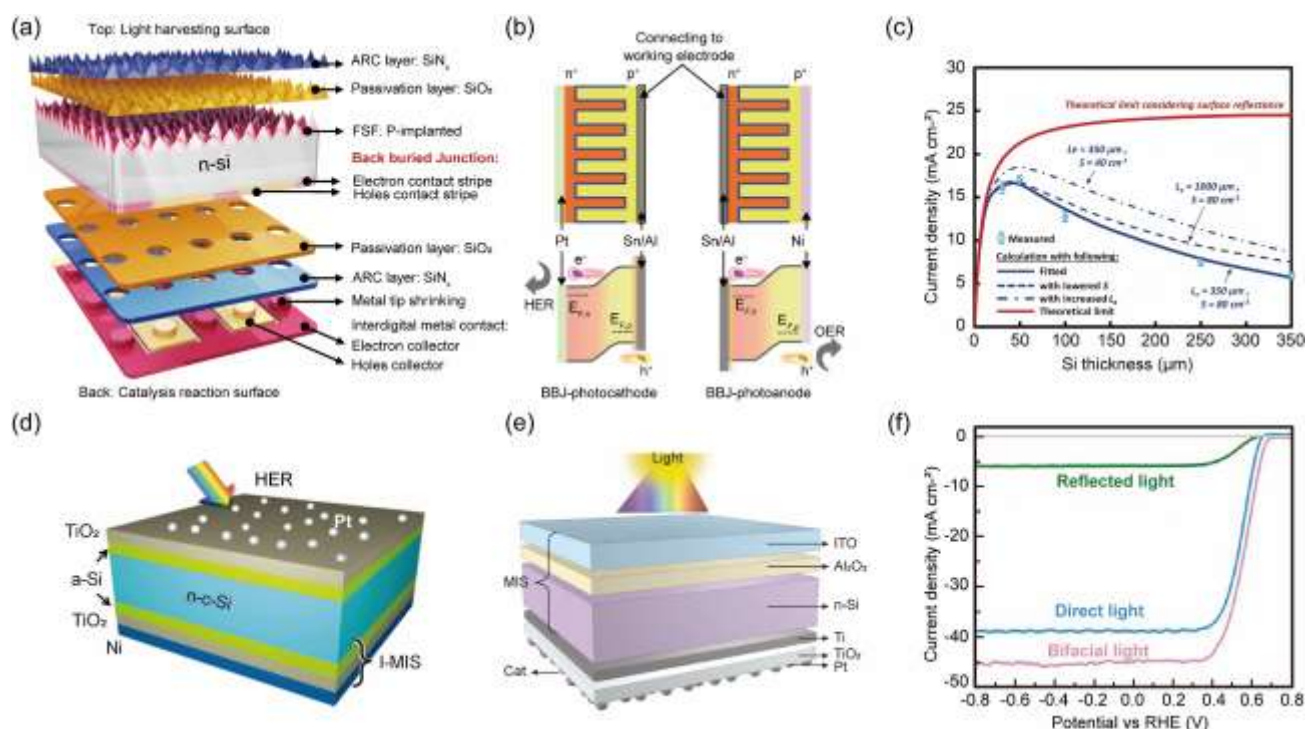

Fig. 26 Derivative configurations of single MIS photoelectrodes. (a) Schematic of the components, (b) Schematic illustration of band diagrams of the back-illuminated MIS photoelectrodes with interdigitated BBJ structure. Reproduced from ref. 320 under the terms of the CC-BY 4.0 license, copyright 2023, The Authors, published by the Springer Nature. (c) Dependence of theoretical photocurrent density limits on silicon thickness: comparing curves at fixed and increased carrier diffusion length (L_e) and surface recombination velocity (S). Reproduced from ref. 269 with permission from the Royal Society of Chemistry, copyright 2015. (d) Schematic illustration of the configuration of the Si I-MIS photocathode. Reproduced from ref. 172 with permission from the Royal Society of Chemistry, copyright 2020. (e) Schematic illustration of the configuration of the illumination-reaction decoupled n-Si MIS photocathode (ITO/Al$_2$O$_3$/n-Si/Ti/TiO$_2$/Pt). Reproduced from ref. 52 under the terms of the CC-BY 4.0 license, copyright 2020, The Authors, published by Oxford University Press on behalf of China Science Publishing & Media Ltd. (f) Comparison of J-V curves for double-side Si photocathode under bifacial, direct, and reflected light illumination. Reproduced from ref. 173 with permission from the John Wiley and Sons, copyright 2020.

which served as hole and electron collection terminals, respectively. Electrodes were directly connected to these doped regions, enabling efficient carrier extraction from the back side. The front side incorporated micron-sized pyramida structures to enhance light absorption, and light doping on the pyramid surface formed a front surface field, suppressing surface recombination. This planar structure design separates front light absorption and back catalytic reaction, allowing for the optimization of back-side carrier collection and electrocatalytic performance without affecting incident light. The working principle of the BBJ structure is illustrated in Fig. 26b. Incident light enters photoelectrodes from the opposing side of the BBJ structure, generating electron-hole pairs in the absorber layer (n-Si). The built-in electric field induced by the back-surface BBJ drives the separation and collection of electrons and holes by their respective emitter regions. The collected carriers are then transferred to the electrolyte

through the grid electrodes on the back side, participating in hydrogen and oxygen evolution reactions. The back-illuminated Si photoelectrode based on this BBJ structure achieves a photocurrent density of 40.51 mA cm^{-2}, approaching the theoretical limit of single-junction Si.[321] Moreover, the BBJ structure is readily integrated into a monolithic device. By connecting three BBJ units in series, the authors obtained an open-circuit voltage of 1.83 V, achieving unassisted overall water splitting with a STH conversion efficiency of 15.62%. In Bae et al.'s study, they also found that surface recombination velocity begins to dominate the carrier recombination loss when the L_e/L exceeds 2.[269] This implies that once the L_e reaches a certain value relative to the absorber thickness, further efforts to reduce the thickness of the silicon substrate yield diminishing returns. Instead, surface passivation emerges as a more critical factor in suppressing carrier recombination. Fig. 26c further highlights the significance of surface passivation by comparing

devices with different L_e and surface recombination velocity (S) values. It is clear that reducing S is more effective in enhancing device performance than increasing L_e. Therefore, suppressing surface recombination should be a key focus in device optimization, as it can lead to substantial improvements in carrier collection and overall performance. The insights gained from Bae et al.'s study provide a foundation for exploring novel configurations of MIS photoelectrodes that aim to effectively reduce surface recombination losses.

Previous studies by Bae et al. and Fu et al. aimed to enhance charge separation efficiency in back-illuminated MIS photoelectrodes by introducing p-n homojunctions at the rear side. However, this approach requires high-temperature, high-energy, and highly toxic ion implantation or thermal diffusion processes,[322,323] compromising the advantage of facile MIS structure fabrication. As mentioned earlier, effective suppression of surface recombination can provide more opportunities for the optimization of MIS structure. The Gong group recently proposed a bifacial amorphous silicon (a-Si) passivation strategy, depositing thin layers (5 nm) of intrinsic a-Si on both sides of the silicon substrate to passivate surface dangling bonds.[52,172,173] This approach significantly increased the minority carrier lifetime to 3050 μs and the diffusion length to 1940 μm,[173] enabling the development of innovative MIS photoelectrode configurations. Liu et al. introduced an inverted MIS (I-MIS) photoelectrode structure, depositing a 100 nm thick Ni layer on the rear side of n-Si to form a uniform Schottky junction and enhance photovoltage, while Pt nanoparticles were deposited on the front side as the HER catalyst (Fig. 26d).[172] The I-MIS structure exploits the MIS heterojunction's band bending capability to achieve a uniform depletion region distribution while avoiding parasitic light absorption by thick metal layers. The resulting n-Si I-MIS photocathode achieved an onset potential of 0.62 V (vs. RHE), an ABPE of 12.66%, and stability exceeding 100 hours. However, due to the opacity of Ni, the catalytic reaction sites remained on the same side as the light absorption region. Wang et al. further improved the I-MIS structure by replacing metallic Ni with transparent and conductive indium tin oxide (ITO), achieving complete spatial decoupling of light absorption and catalytic reaction sites (Fig. 26e).[52] ITO has a work function difference of ~0.8 eV relative to n-Si, enabling the formation of a substantial Schottky barrier, while its excellent optical transparency ensures light transmittance above 90% even at a thickness of 46 nm. This "killing two birds with one stone" device exhibited an onset potential of 0.57 V (vs. RHE), a photocurrent density of 39 mA cm^{-2}, an ABPE of 10.26%, and stability exceeding 300 hours. Moreover, Liu et al. designed a double-sided light-absorbing silicon photocathode, with the front side absorbing direct light and the back side absorbing scattered light from the ground, to further enhance light-capturing capability.[173] Under simulated practical application conditions with double-sided illumination, this photoelectrode achieved a high saturated photocurrent of 45.5 mA cm^{-2} and an ABPE of 17.9%, surpassing single-sided illumination devices (Fig. 26f). This biomimetic double-sided power generation design provides a new approach for improving the efficiency of silicon-based photoelectrodes in

practical applications. In summary, the Gong group has focused on structural innovation and interface optimization of silicon-based MIS photoelectrodes. The bifacial a-Si passivation strategy increased the minority carrier diffusion length to 1940 μm, providing a foundation for designing novel configurations of MIS photoelectrodes. The I-MIS structure minimizes parasitic absorption of the catalyst while obtaining a uniform depletion region, and the double-sided light-receiving strategy enhances light-capturing capability. These advancements demonstrate the potential for designing high-performance MIS photoelectrodes for PEC water splitting applications.

7.2 Tandem MIS photoelectrodes

Single light-absorbing layer MIS photoelectrodes have made progress in band structure design, light absorption regulation, and surface recombination suppression.[1,27] However, they still face limitations in achieving unbiased PEC water splitting. Single MIS photoelectrodes often encounter a trade-off between photovoltage and photocurrent. Wide-bandgap semiconductors usually achieve higher photovoltage but lower saturation current, while narrow-bandgap semiconductors can obtain higher saturation current but insufficient photovoltage to meet the thermodynamic potential required for water splitting.[324] Constructing tandem PEC configurations has become a feasible and attractive approach to overcome the limitations of single photoelectrodes and achieve unbiased PEC water splitting. Tandem PEC cells can be classified into two main categories: photoelectrode-photovoltaic (PEC-PV) tandem cells and photoanode-photocathode (PEC-PEC) tandem cells. PEC-PV tandem cells combine a photoelectrode with a PV cell, utilizing the PV module to provide additional photovoltage. The PEC-PV tandem cells have achieved the high PEC conversion efficiencies to date;[314] however, they often experience optical and electrical coupling losses between the PV and photoelectrode components, and the system is relatively complex. In contrast, PEC-PEC tandem cells consist of two semiconductor photoelectrodes with different bandgaps connected in series, which is more advantageous for reducing costs and system complexity. Tandem photoelectrode structures consist of two or more semiconductor light-absorbing layers with different bandgaps connected in series, significantly extending the absorption range of solar spectrum. Furthermore, tandem photoelectrodes are not restricted by the flatband potential requirement of simultaneously straddling the thermodynamic potentials of hydrogen and oxygen evolution reactions. Theoretical calculations show that a PEC tandem cell with an optimal bandgap combination of 1.60 eV and 0.95 eV can achieve a maximum STH efficiency of 29.7%,[325] surpassing the theoretical efficiency limit of single photoelectrodes. Consequently, PEC tandem cells are widely recognized as an important development direction for achieving highly efficient next-generation solar water splitting technology.As this article focuses on the application of MIS photoelectrodes in PEC water splitting, the following section will primarily discuss PEC-PEC tandem cells. The PEC-PEC tandem MIS photoelectrodes primarily include two configurations: wired (Fig. 25c) and wireless (Fig. 25d). In the wired configuration, two

independently prepared photoelectrodes are connected in series through a wire, with the wide-bandgap semiconductor placed in front of the narrow-bandgap semiconductor to improve the overall light absorption efficiency of the PEC system. The wireless configuration involves growing the photoanode and photocathode materials back-to-back on the same substrate, connected by a transparent conductive layer, forming a monolithically integrated device. Although the compact monolithic configuration is more challenging in terms of fabrication process, it can significantly reduce system complexity and is more conducive to practical applications. The wired configuration has advantages in experimental research and assembly debugging, while the wireless configuration is more favorable for the development of highly integrated PEC water splitting systems.[326]

Silicon, with a bandgap of 1.12 eV, is an excellent candidate for the bottom light absorber in a tandem cell. Its bandgap is close to the optimal value for the small bandgap absorber, and it has been highly optimized for photovoltaic applications.[325] Metal oxide semiconductors, on the other hand, are promising candidates for the top wide-bandgap light absorber in a tandem PEC device. Their key advantages include earth abundance, low cost, low toxicity, facile synthesis, tunable compositions, and relatively high aqueous stability. By coupling Si as the bottom photoelectrode with wide-bandgap metal oxide materials, the limitations of single light-absorbing materials can be effectively overcome, leading to simultaneous enhancements in STH conversion efficiency and reductions in device cost. Surface passivation remains a key factor in further improving the performance of tandem PEC devices. Moon et al. proposed a passivation solution using a tunnel oxide passivated contact (TOPCon) structure.[327] The ultrathin SiO_2 tunnel layer significantly reduces surface carrier recombination rates, while the doped polycrystalline silicon layer forms an ohmic contact between SiO_2 and the metal, resulting in excellent carrier collection efficiency. Additionally, the SiO_2 layer and polycrystalline silicon layer serve as effective diffusion barrier layers and impurity absorption layers, greatly enhancing the thermal stability of the device during high-temperature fabrication processes and preventing the diffusion of metals into Si. The study found that TOPCon-based Si photoelectrodes can generate photovoltages of 640-650 mV, regardless of the electrolyte being acidic, neutral, or alkaline. Moreover, the TOPCon structure demonstrates excellent thermal stability, with no significant performance degradation after high-temperature treatment at 600°C for 1 hour in air. This thermal stability enables compatibility with the deposition of wide-bandgap metal oxide top cells, which often require high temperatures. The authors preliminarily demonstrated an earth-abundant tandem PEC water splitting device by coupling the $BiVO_4/SnO_2/NiFe$ photoanode with the TOPCon Si photocathode (Fig. 27a). The initial photocurrent density of the tandem device reached 0.2 mA cm^{-2} under 1 sun illumination. Apart from the commonly used tandem PEC cells consisting of two separate photoelectrodes, integrated tandem heterojunction photoelectrodes, which combine two semiconductors into a single device, offer increased flexibility in

design and scalability.[328,329] However, Si/metal oxide integrated tandem photoelectrodes have typically demonstrated low STH efficiencies due to the poor electrical properties and short carrier diffusion lengths of metal oxides, as well as severe interfacial recombination caused by defect states at the Si/metal oxide interface.[74,330] To achieve high-efficiency integrated tandem photoelectrodes, two key challenges must be addressed: (1) ensuring high-quality contact between Si and metal oxide to enhance interfacial carrier transport, and (2) suppressing interfacial defect states to reduce carrier recombination. Wang et al. tackled these challenges by introducing an MIS heterojunction consisting of Al_2O_3 and ITO between n-Si and $BiVO_4$ (Fig. 27b).[331] The ITO layer forms a Schottky junction with n-Si, increasing band bending, while also forming an ohmic contact with $BiVO_4$ to promote electron transport. This simultaneously widens the band offsets at both the n-Si/ITO and ITO/$BiVO_4$ interfaces, maximizing the photovoltage output. The Al_2O_3 layer, acting as a tunneling insulator layer, effectively passivates defects at the n-Si/ITO interface, suppressing carrier recombination while ensuring electron tunneling transport. This elegantly resolves the trade-off between interfacial band alignment and passivation. Benefiting from the synergistic effect of the Al_2O_3/ITO bilayer heterojunction, the n-Si/Al_2O_3/ITO/$BiVO_4$ photoanode, compared to the n-Si/$BiVO_4$ photoanode without the MIS heterojunction, exhibited a 1000 mV increase in photovoltage and a significant improvement in interfacial carrier separation efficiency from 0.4% to 66.7%. When coupled with a Pt cathode, the device achieved a steady-state STH efficiency of 0.62% without external bias and demonstrated stable operation for 1045 hours. Recently, Jung et al. proposed a multi-coordinated interface engineering strategy to enhance the performance of Si/$BiVO_4$ integrated tandem photoelectrodes.[332] They employed the previously introduced TOPCon structure as the Si bottom cell and incorporated a Ta-doped SnO_2 (TTO) composite layer between the n-Si and $BiVO_4$, along with an SnO_2 hole-blocking layer. As shown in Fig. 27c, the SiO_2 passivation layer and doped polysilicon contact layer in the TOPCon structure minimize interface recombination, achieving a photovoltage output as high as 590 mV. Meanwhile, the SnO_2 hole-blocking layer forms a large band offset with $BiVO_4$, suppressing the transport of photogenerated holes towards Si. Furthermore, the excellent thermal stability of TOPCon structure allows the photoelectrode to withstand temperatures up to 500°C during the $BiVO_4$ deposition process. Benefiting from these synergistic effects, the Si/$BiVO_4$ integrated tandem photoanode achieved a photocurrent of 1.4 mA cm^{-2} (1.72% STH efficiency).

Monolithically integrated wireless tandem photoelectrodes offer an attractive new paradigm for developing efficient, compact, and flexible PEC water-splitting systems.[333] These devices ingeniously combine photocathode and photoanode materials into a single unit, eliminating the need for complex external connections and packaging associated with discrete devices, resulting in a more compact and lightweight PEC system.[334] Notably, the monolithic integrated wireless structure can significantly reduce optical and ohmic losses.[335] By confining the illumination path within the thin, single-piece device, light

scattering and parasitic absorption are minimized. Furthermore, the monolithic structure eliminates interfacial contact resistance between discrete devices, allowing photogenerated charge carriers to be collected with minimal transport distance in the thickness direction of the device,

thereby reducing ohmic losses. These unique advantages make monolithically integrated wireless tandem photoelectrodes highly promising for realizing mobile and large-scale artificial leaves. Recent research efforts have successfully demonstrated high-efficiency
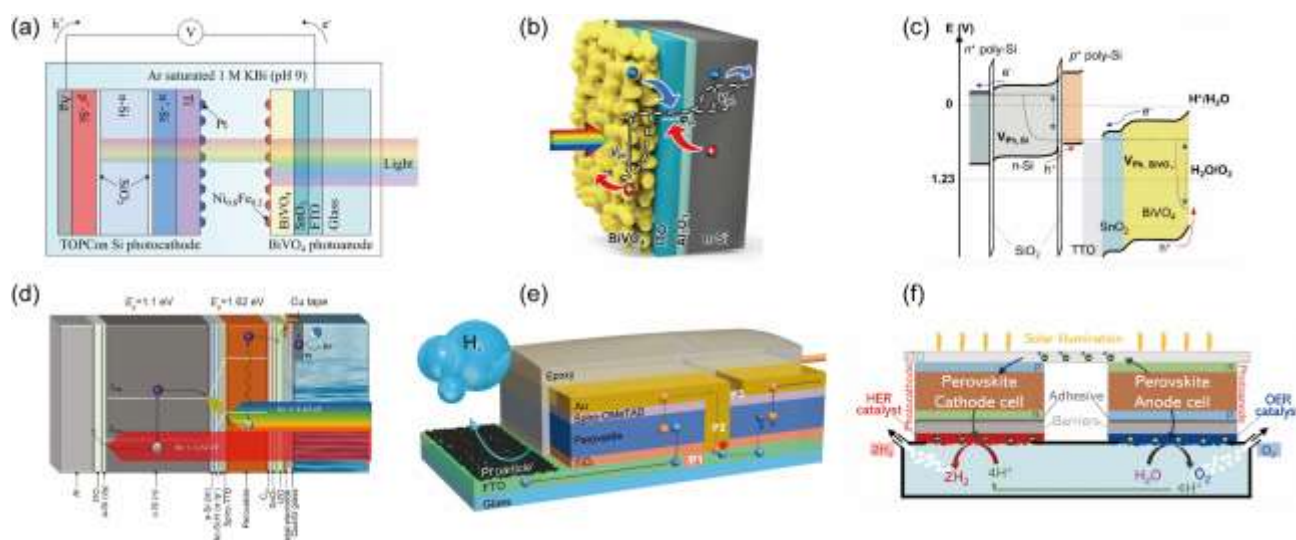

Fig. 27 Derivative configurations of tandem MIS photoelectrodes. (a) The wired tandem PEC cell was constructed using a $BiVO_4$ photoanode as the top cell and a TOPCon Si photocathode as the bottom cell. Reproduced from ref. 327 with permission from the Royal Society of Chemistry, copyright 2023. (b) Schematic illustration of the configuration of the n-Si/Al_2O_3/ITO/$BiVO_4$ integrated tandem photoanode. Reproduced from ref. 331 under the terms of the CC-BY 4.0 license, copyright 2023, The Authors, published by the Royal Society of Chemistry. (c) Schematic illustration of band diagrams of the BVO/SnO_2/TTO/TOPCon Si integrated tandem photoanode. Reproduced from ref. 332 with permission from the John Wiley and Sons, copyright 2020. (d) Schematic illustration of the configuration of the Pt/quartz glass/perovskite/silicon tandem photocathode for water splitting. Reproduced from ref. 340 with permission from the John Wiley and Sons, copyright 2021. (e) Schematic illustration of the configuration of the optically parallel and electrically series-connected dual perovskite module photocathode. Reproduced from ref. 338 with permission from the John Wiley and Sons, copyright 2023. (f) Schematic illustration of the configuration of CAB-protected perovskite tandem photocathode and photoanode in co-planar series. Reproduced from ref. 339 under the terms of the CC-BY 4.0 license, copyright 2023, The Authors, published by the Springer Nature.

monolithically integrated wireless PEC cells based on Si or metal oxides coupled with perovskites using low-cost, scalable deposition techniques, achieving efficient PEC water splitting without external bias.[336-340] Halide perovskite materials exhibit tremendous potential for application in the field of photoelectrochemistry due to their exceptional optoelectronic properties. By tuning the composition of perovskite materials, their band structure can be continuously adjusted over a wide range (1.4-3.0 eV).[341,342] Seger et al. showed that the optimal bandgap combination for a dual-absorber PEC water-splitting device is around 1.0 eV and 1.7 eV.[343] Perovskite materials can cover this bandgap range to achieve efficient unassisted PEC water splitting. However, the sensitivity of perovskite materials to water, which can lead to decomposition in aqueous electrolytes, limits their direct application in PEC water splitting. To improve the stability of perovskite-based photoelectrodes, researchers have developed various encapsulation and protection strategies, which can be mainly divided into two categories: depositing protective layers on the perovskite surface and employing additional physical barrier encapsulation.[339] The former includes sputtering catalytic

metals, surface hydrophobic treatment, and thin insulator layers;[122,124,344] the latter utilizes materials such as graphite epoxy resin and InBiSn alloys for physical encapsulation.[123,345] Wang et al. employed quartz glass as a protective layer, which not only prevents the corrosion of the perovskite light-absorbing layer by the electrolyte but also minimizes incident light loss.[340] The tandem photoelectrode device with Si achieved a STH efficiency of 19.68% in acidic electrolyte and maintained stable performance for 20 hours without noticeable degradation, demonstrating excellent efficiency and stability (Fig. 27d). Monolithically integrated wireless tandem PEC cells have attracted significant attention due to their unique design, but their highly integrated nature also poses several challenges. Compared to traditional wired PEC cells, wireless tandem photoelectrodes suffer from internal contact losses and longer ionic conduction distances.[346] To fully exploit the advantages of monolithically integrated wireless tandem photoelectrodes, optimization of device structures and internal components is imperative. Park et al. proposed a series of innovative structural design strategies to address the efficiency and stability issues of monolithically integrated wireless tandem PEC cells (Fig.

27e).[338] They employed a spatially decoupled configuration, separating the perovskite light-absorbing layer from the Pt catalyst, which effectively protected the perovskite using epoxy resin while enhancing light absorption efficiency, achieving stability exceeding 85 hours. Furthermore, the optically parallel and electrically series-connected dual PV module photocathode, fabricated via laser scribing, generated sufficiently high photovoltage and photocurrent density, resulting in an applied bias photoconversion efficiency of 13.5%. Finally, by directly integrating the NiFe catalyst onto the dual PV module, a wireless artificial leaf configuration with single-sided HER/OER catalysts was constructed, shortening charge carrier transport pathways and preventing ionic detour issues, ultimately achieving a STH efficiency of about 11%. Fehr et al. developed a lossless anticorrosion barrier called the conductive adhesive-barrier (CAB), which consists of an inert, impermeable conductive material and a conductive adhesive.[339] The entire barrier-catalyst assembly can be fabricated independently and then transferred onto the perovskite light-absorbing layer via a dry process, significantly reducing damage to the perovskite during device fabrication. The CAB effectively protects the perovskite light-absorbing layer and transport layers from corrosive electrolytes while minimally impacting the transport of photogenerated charge carriers. Utilizing the CAB structure, a co-planar series-connected tandem photocathode-photoanode configuration (as shown in Fig. 27f) for monolithic wireless water-splitting devices was designed. They electrically connected the CAB-protected perovskite photocathode and photoanode in series and arranged them on the same plane for illumination, generating sufficiently high photovoltage to drive the overall water-splitting reaction while maintaining high photocurrent density. With a total absorber area of 0.24 cm², the device achieved a solar-to-hydrogen efficiency of 13.4% and remained stable for 5 hours. Wireless tandem photoelectrodes unlock a new realm of possibilities for PEC water splitting, with their potential applications extending far beyond artificial leaves to complex and diverse fields such as in vivo optoelectronic modulation. Recent studies have demonstrated the potential of wireless optoelectronic devices for neuromodulation, showcasing their ability to efficiently and selectively stimulate peripheral nerve activity without the need for genetic modifications.[347,348] However, the highly integrated nature of wireless tandem photoelectrodes also presents challenges, such as internal contact losses, longer ionic conduction distances, and difficulties in precise characterization. To fully harness the potential of wireless devices in PEC water splitting, further research is needed to optimize device structures and internal components.

The development of derivative MIS photoelectrode configurations, including back-illuminated MIS photoelectrodes, inverted MIS photoelectrodes, tandem MIS photoelectrodes, and monolithically integrated wireless MIS photoelectrodes, is vital for advancing PEC water splitting technology towards practical applications. These innovative configurations tackle the limitations of traditional MIS structures by effectively coupling different functional modules, minimizing optical and ohmic losses, and mitigating recombination losses. By exploring novel device architectures, interface engineering strategies, and materials combinations, researchers have demonstrated enhanced performance, stability, and scalability in these derivative MIS photoelectrodes. Future research should prioritize optimizing device structures, enhancing interfacial properties, and establishing reliable characterization methods to fully realize the potential of these photoelectrode configurations and expedite the commercialization of PEC water splitting systems.

8. Conclusions and outlooks

Highly efficient, durable, and cost-effective PEC solar-to-fuel energy conversion systems offer a transformative avenue for shifting energy consumption patterns. Since the initial revelation of photoelectrochemical water splitting on semiconductor electrodes,[12] researchers have embarked on a trajectory of diversifying photoelectrode structural strategies to counteract challenges in efficiency and stability,[28] including surface modification,[349] semiconductor-semiconductor heterostructures,[350] metal-semiconductor heterostructures,[351] and multi-layered heterostructures, etc. Among these strategies, the MIS heterostructure has gained prominence within the field of PEC energy conversion, owing to its facile fabrication process and the synergistic interplay among its three functional layers. This review provides a comprehensive overview of the constituent materials, fabrication methodologies, interfacial regulation strategies, design principles, carrier-transfer mechanisms and innovative derivative configurations of MIS photoelectrodes for PEC water splitting. Semiconductor light-absorbing layers constitute the pivotal component of MIS photoelectrodes that propel the PEC energy conversion process. Various types of semiconductors are employed to fabricate MIS photoelectrodes, from traditional PV-grade materials known for efficient charge transport and narrow band gaps, to metal oxides that are resource-abundant and cost-effective, as well as emerging semiconductors featuring structural diversity and high light absorption coefficients. The inherent limitations of each semiconductor would influence the performance of MIS photoelectrodes, such as the narrow band gap of traditional semiconductors, the low carrier mobility within metal oxides, and heterogeneous integration issues in emerging semiconductors. Surface engineering and tandem configuration engineering are prevalent strategies for enhancing light absorption efficiency and photovoltage. Semiconductor photoelectrodes frequently encounter chemical, electrochemical, and photoelectrochemical corrosion mechanisms within the corrosive electrolytes during operation. This exposure can result in substantial electrode deterioration, potentially undermining the robustness of PEC systems, particularly for susceptible semiconductor materials. The insulator protective layer in MIS photoelectrodes could not only prevent the semiconductor from directly contacting the corrosive electrolyte but also address Fermi-level pinning by passivating interfacial surface states to facilitate minority carrier transfer. The candidate materials for the insulator layer

predominantly encompass wide-bandgap oxides (such as TiO_x, ZrO_x, HfO_x, AlO_x, GaO_x, SiO_x, etc.) as well as organic polymers like organosilane. Diverse thin film deposition technologies have been employed to create high-quality insulator layers, broadly categorized as vacuum deposition and non-vacuum deposition technologies. Vacuum deposition technologies, such as physical vapor deposition and chemical vapor deposition, offer precise control over film characteristics and are suited for large-scale production. Non-vacuum technologies, such as (photo)electrochemical deposition, droplet deposition, and solvothermal deposition, circumvent the need for expensive equipment and ultra-clean experimental environments. The choice of optimal film deposition technique depends on the insulator material properties and the performance requisites of the MIS photoelectrode. Bare semiconductor materials often struggle with slow redox kinetics and carrier recombination, requiring significant bias voltage for PEC water splitting. The metal-based cocatalyst layer minimizes the PEC reaction kinetic barriers and improves carrier separation. The burgeoning advancements in electrocatalytic water splitting have spurred the investigation of electrocatalytic water splitting mechanisms on metallic surfaces and the expansion of the electrocatalyst repertoire for this process. Consequently, the cocatalysts employed in MIS photoelectrodes have undergone a rapid development, transitioning from precious metal cocatalysts to earth-abundant transition metal cocatalysts, and further evolving towards molecular and single-atom cocatalysts with superior atomic utilization efficiency. MIS photoelectrode performance hinges not on the exceptional attributes of any singular functional layer, but mandates a synergic collaboration among all three functional layers to attain energy level alignment that reduces the energy loss during carrier transport across the heterointerfaces. Therefore, we have systematically elucidated the carrier-transfer mechanisms of MIS photoelectrodes for the first time, encompassing the tunneling effect, the conduction/valence band, the constructed defect states or intermediate bands, and the embedded conduction pathways. Furthermore, we have also introduced energy band regulation strategies within the mechanism section that include the incorporation of buried junctions within the semiconductor layer and adjustments to insulator layer properties and metal work function. Finally, we discuss innovative MIS photoelectrode configurations that effectively couple light-absorbing layers, protective layers, and catalytic layers to address the limitations of traditional MIS structures. The focus is on two primary categories of derivative MIS photoelectrode configurations: single MIS photoelectrodes, including back-illuminated and inverted MIS photoelectrodes, and tandem MIS photoelectrodes, comprising wired and wireless configurations. These advanced designs aim to minimize optical and ohmic losses, mitigate recombination losses, and ultimately achieve enhanced performance, long-term stability, and potential for scalability. Although initially conceptualized by Green in the 1970s,[15,16] the utilization of MIS heterostructures for PEC energy conversion has primarily gained attention over the last decade. Notwithstanding, substantial challenges endure in the

pursuit of developing efficient and durable MIS photoelectrodes (Fig. 28).

First, the central goal of MIS photoelectrode research is discovering novel materials for its three functional layers. Currently, most research papers rely heavily on the traditional trial-and-error approach for the advancement of novel MIS photoelectrodes. However, this traditional approach necessitates substantial time and labor investments, and struggles with data reproducibility due to manual testing. The advancement of computer hardware and artificial intelligence algorithms has accelerated the utilization of computational high-throughput screening and machine learning techniques which offer distinct advantages in predicting material properties within extensive parameter spaces, thereby expediting material discovery in materials science and biomedicine.[352,353] While initial strides have been taken in material systems exhibiting discernible correlations between macroscopic functionalities and atomic-scale attributes,[354-356] the advancement of experimental and computational high-throughput screening for MIS photoelectrode development remains in the blank stage. This is attributed not only to the complex interface issues of multiple functional layers within MIS photoelectrodes but also to the imperative consideration of the interactions between the localized electrolyte microenvironment and the photoelectrodes.[13] However, the advent of high-throughput PEC measurements and automated experimental platforms has ushered in a pivotal era,[357,358] furnishing the essential foundation for generating consistent training datasets to create precise and dependable machine learning models for the high-throughput screening of MIS photoelectrodes.

Second, developing advanced characterization methodologies enables unravelling the working mechanisms of PEC systems. Ex-situ characterization methods, such as electrochemical impedance spectroscopy and transient photophysical analysis,[359] can accurately monitor the dynamic processes of photogenerated carrier excitation, transfer, and recombination.[27] Nevertheless, ex-situ methods typically demand vacuum environments and lack the capacity to capture real-time dynamic behaviors of photoelectrodes during PEC operations. In contrast, in-situ characterization approaches performed under electrochemical circumstances, including in-situ spectroscopy, in-situ mass spectrometry, and in-situ microscopy,[360] could elucidate the electrochemical reaction mechanisms of PEC conversion reactions and photoelectrode corrosion reactions,[285,361] occurring at the photoelectrode/electrolyte interface.

Third, the development of MIS photoelectrodes for the sustainable production of high-value chemicals. Despite significant advancements in MIS photoelectrodes for PEC water splitting, producing high-value chemicals is becoming a key research focus to improve the economic competitiveness of this technology. Two main strategies have emerged to achieve this goal: 1) utilizing the hydrogen generated at the photocathode for in situ hydrogenation reactions, such as the hydrogenation of itaconic acid to produce valuable chemicals methyl succinic acid,[362,363] and 2) replacing the kinetically sluggish OER with

more facile oxidation reactions to enhance conversion efficiency, such as the oxidation of 5-hydroxymethylfuran-2-carbaldehyde, glucose, lignocellulose, or glycerol.[261,364,365] Furthermore, the coupling of CO_2 reduction with plastic waste valorization is emerging as a promising research direction for establishing a sustainable carbon cycle.[366,367] As research in this field progresses, it is expected that MIS photoelectrodes will play a crucial role in the transition towards a more sustainable and net-zero-carbon circular economy.
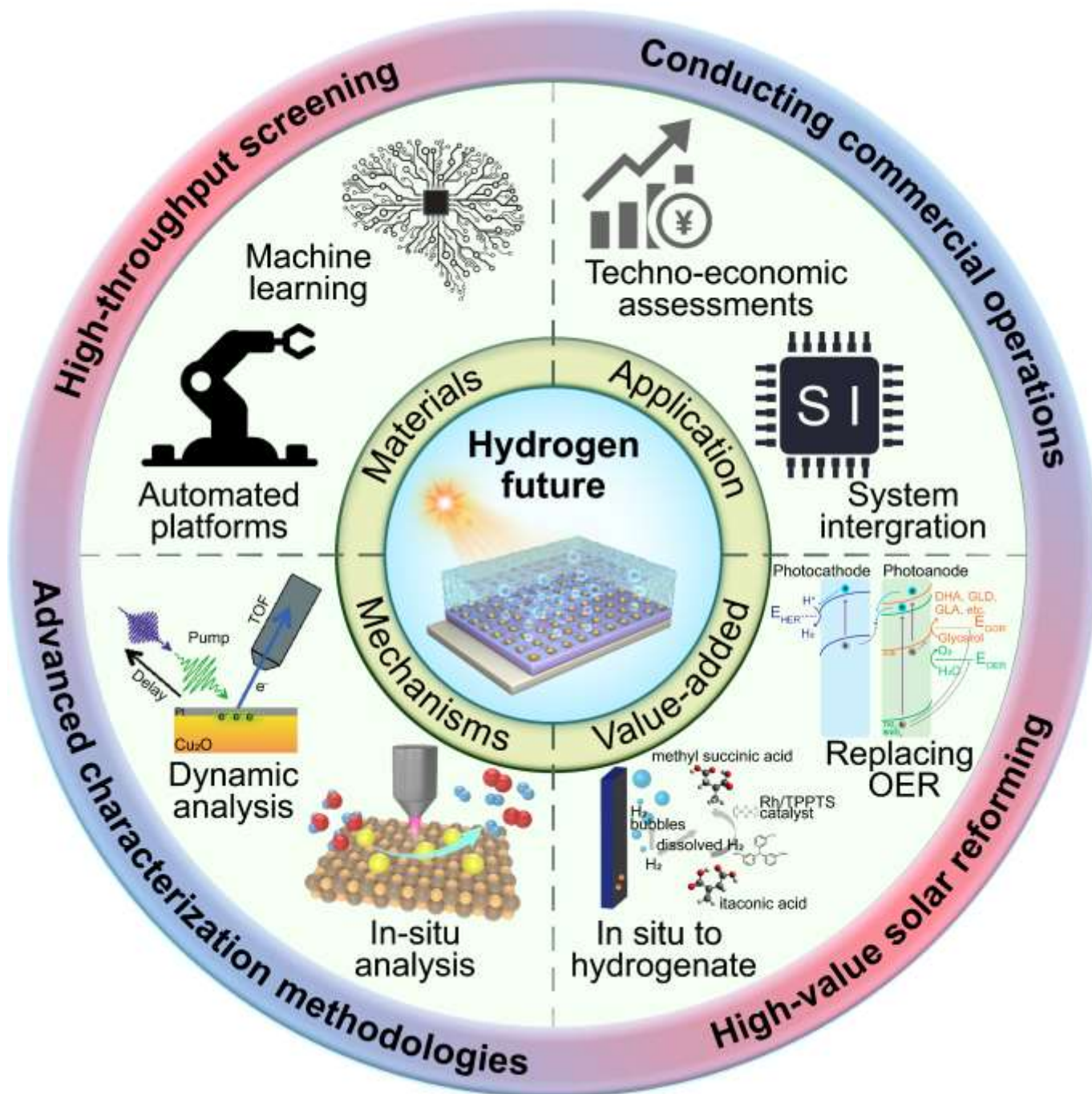

Fig. 28 Future challenges and research directions for MIS photoelectrodes. Reproduced from ref. 359 under the terms of the CC-BY 4.0 license, copyright 2019, The Authors, published by the Springer Nature; ref 363 under the terms of the CC-BY 4.0 license, copyright 2023, The Authors, published by the Springer Nature; ref 365 with permission from the American Chemical Society, copyright 2023.

Fourth, formulating comprehensive techno-economic assessments (TEA) of MIS photoelectrodes for PEC water splitting is essential to bridge the gap between laboratory-scale experiments and industrial-scale implementation, pinpointing

necessary technological advancements and setting tangible, cost-effective targets. As the transition from a carbon cycle to a hydrogen energy cycle gains momentum, understanding the economic scale and environmental impact of hydrogen energy becomes increasingly critical. In 2022, the worldwide consumption of hydrogen rose to 95 million tons, marking a nearly 3% year-on-year increase,[11] which highlighted hydrogen's vast potential as a carbon-free energy carrier. However, current low-emission hydrogen production constitutes less than 1% of global hydrogen production.[11] The average emissions intensity of global hydrogen production was approximately 12-13 kg CO_2-eq (kg H_2)$^{-1}$ in 2021, which, according to the IEA Net Zero by 2050 Scenario, is expected to decrease to 6-7 kg CO_2-eq (kg H_2)$^{-1}$ by 2030.[368] These trends underscore the urgent need for developing low-emission hydrogen production methods, such as PEC water splitting, to meet the ambitious goal of abating seven gigatons of CO_2 emissions annually through clean hydrogen by 2050.[369] These TEA tools provide a framework for economic modelling of various low-emission hydrogen production processes, highlighting the critical parameters affecting the levelized cost of hydrogen. Specifically for PEC systems, TEA literatures have identified key performance indicators such as STH efficiency, solar concentration factor, cell cost, and cell lifetime.[13,370,371] Addressing these parameters is vital for advancing PEC technology towards economic viability and large-scale adoption.

Although current photoelectrodes demonstrate high STH efficiency (> 10%) and excellent stability (~500 h) through multi-junction structures and innovative protection strategies,[164,372,373] the cost of hydrogen production via PEC approach (~10 USD kg^{-1}) remains substantially higher than that produced from traditional fossil fuel methods (~1.5 USD kg^{-1}).[374] To transition from research to real-world application, a two-fold strategy is imperative. First, continued research must focus on enhancing the efficiency and reducing the cost of PEC systems. Concurrently, it is crucial to cultivate a robust market demand for low-emission hydrogen. This involves not just technological advancements but also a paradigm shift in industry practices, integrating hydrogen fuel cells,[375] transport,[376] and preparation of high value-added chemicals,[363] etc. The large-scale implementation of a green hydrogen economy represents a global energy revolution, which calls for interdisciplinary cooperation, aligning the efforts of countries, governments, industries, and private sectors to create favorable policies and infrastructures. In this transformative era, MIS photoelectrodes for PEC water splitting stand at the forefront, embodying a pivotal technology that bridges current capabilities with ecological and energy demands in the future.

Conflicts of interest

There are no conflicts to declare.

Acknowledgements

References

1. Z. Luo, T. Wang and J. Gong, *Chem. Soc. Rev.*, 2019, **48**, 2158-2181.
2. A. Turner John, *Science*, 2004, **305**, 972-974.
3. S. Sharma and S. K. Ghoshal, *Renewable Sustainable Energy Rev.*, 2015, **43**, 1151-1158.
4. A. de Vries, *Joule*, 2023, **7**, 2191-2194.
5. L. Chen, G. Msigwa, M. Yang, A. I. Osman, S. Fawzy, D. W. Rooney and P.-S. Yap, *Environ. Chem. Lett.*, 2022, **20**, 2277-2310.
6. Z. Liu, Z. Deng, G. He, H. Wang, X. Zhang, J. Lin, Y. Qi and X. Liang, *Nat. Rev. Earth Environ.*, 2022, **3**, 141-155.
7. M. Hosenuzzaman, N. A. Rahim, J. Selvaraj, M. Hasanuzzaman, A. B. M. A. Malek and A. Nahar, *Renewable Sustainable Energy Rev.*, 2015, **41**, 284-297.
8. W. Seboldt, *Acta Astronaut.*, 2004, **55**, 389-399.
9. R. Shah, N. Mithulananthan, R. C. Bansal and V. K. Ramachandaramurthy, *Renewable Sustainable Energy Rev.*, 2015, **41**, 1423-1436.
10. G. Notton, M.-L. Nivet, C. Voyant, C. Paoli, C. Darras, F. Motte and A. Fouilloy, *Renewable and Sustainable Energy Rev.*, 2018, **87**, 96-105.
11. IEA (2023), Global Hydrogen Review 2023, IEA, Paris https://www.iea.org/reports/global-hydrogen-review-2023, License: CC BY 4.0
12. A. Fujishima and K. Honda, *Nature*, 1972, **238**, 37-38.
13. G. Segev, J. Kibsgaard, C. Hahn, Z. J. Xu, W.-H. Cheng, T. G. Deutsch, C. Xiang, J. Z. Zhang, L. Hammarström, D. G. Nocera, A. Z. Weber, P. Agbo, T. Hisatomi, F. E. Osterloh, K. Domen, F. F. Abdi, S. Haussener, D. J. Miller, S. Ardo, P. C. McIntyre, T. Hannappel, S. Hu, H. Atwater, J. M. Gregoire, M. Z. Ertem, I. D. Sharp, K.-S. Choi, J. S. Lee, O. Ishitani, J. W. Ager, R. R. Prabhakar, A. T. Bell, S. W. Boettcher, K. Vincent, K. Takanabe, V. Artero, R. Napier, B. R. Cuenya, M. T. M. Koper, R. Van De Krol and F. Houle, *J. Phys. D: Appl. Phys.*, 2022, **55**, 323003.
14. J. Schneidewind, *Adv. Energy Mater.*, 2022, **12**, 2200342.
15. M. Green and J. Shewchun, *Solid-State Electron.*, 1974, **17**, 349-365.
16. M. Green, F. King and J. Shewchun, *Solid-State Electron.*, 1974, **17**, 551-561.
17. Y. W. Chen, J. D. Prange, S. Duhnen, Y. Park, M. Gunji, C. E. D. Chidsey and P. C. McIntyre, *Nat. Mater.*, 2011, **10**, 539-544.
18. S. Hu, M. R. Shaner, J. A. Beardslee, M. Lichterman, B. S. Brunschwig and N. S. Lewis, *Science*, 2014, **344**, 1005-1009.

19. D. V. Esposito, I. Levin, T. P. Moffat and A. A. Talin, *Nat. Mater.*, 2013, **12**, 562-568.

20. M. J. Kenney, M. Gong, Y. G. Li, J. Z. Wu, J. Feng, M. Lanza and H. J. Dai, *Science*, 2013, **342**, 836-840.

21. L. Ji, M. D. McDaniel, S. J. Wang, A. B. Posadas, X. H. Li, H. Y. Huang, J. C. Lee, A. A. Demkov, A. J. Bard, J. G. Ekerdt and E. T. Yu, *Nat. Nanotechnol.*, 2015, **10**, 84-90.

22. L. Ji, H.-Y. Hsu, X. Li, K. Huang, Y. Zhang, J. C. Lee, A. J. Bard and E. T. Yu, *Nat. Mater.*, 2017, **16**, 127-131.

23. S. Lee, L. Ji, A. C. De Palma and E. T. Yu, *Nat. Commun.*, 2021, **12**.

24. M. Thangamuthu, Q. Ruan, P. O. Ohemeng, B. Luo, D. Jing, R. Godin and J. Tang, *Chem. Rev.*, 2022, **122**, 11778-11829.

25. B. Zhang and L. Sun, *Chem. Soc. Rev.*, 2019, **48**, 2216-2264.

26. C. Gao, J. Low, R. Long, T. Kong, J. Zhu and Y. Xiong, *Chem. Rev.*, 2020, **120**, 12175-12216.

27. W. Yang, R. R. Prabhakar, J. Tan, S. D. Tilley and J. Moon, *Chem. Soc. Rev.*, 2019, **48**, 4979-5015.

28. J. Zheng, H. Zhou, Y. Zou, R. Wang, Y. Lyu, S. P. Jiang and S. Wang, *Energy Environ. Sci.*, 2019, **12**, 2345-2374.

29. D. Bae, B. Seger, P. C. K. Vesborg, O. Hansen and I. Chorkendorff, *Chem. Soc. Rev.*, 2017, **46**, 1933-1954.

30. J. Shewchun, R. Singh and M. A. Green, *J. Appl. Phys.*, 1977, **48**, 765-770.

31. F. P. García de Arquer, A. Mihi, D. Kufer and G. Konstantatos, *ACS Nano*, 2013, **7**, 3581-3588.

32. Z. Zhang and J. T. Yates, *Chem. Rev.*, 2012, **112**, 5520-5551.

33. C. Cheng, W. Zhang, X. Chen, S. Peng and Y. Li, *Energy Sci. Eng.*, 2022, **10**, 1526-1543.

34. A. R. Fareza, F. A. A. Nugroho, F. F. Abdi and V. Fauzia, *J. Mater. Chem. A*, 2022, **10**, 8656-8686.

35. P. Kumar and A. Kumar, *Hydrogen Generation Via Photoelectrochemical Splitting of Water*, eds. L. M. T. Martínez, O. V. Kharissova and B. I. Kharisov, Springer Nature Switzerland AG: Cham, Switzerland, 2017.

36. H.-C. Fu, P. Varadhan, M.-L. Tsai, W. Li, Q. Ding, C.-H. Lin, M. Bonifazi, A. Fratalocchi, S. Jin and J.-H. He, *Nano Energy*, 2020, **70**, 104478.

37. D. Kang, J. L. Young, H. Lim, W. E. Klein, H. Chen, Y. Xi, B. Gai, T. G. Deutsch and J. Yoon, *Nat. Energy*, 2017, **2**, 17043.

38. H. Neergaard Waltenburg and J. Yates, *Chem. Rev.*, 1995, **95**, 1589-1673.

39. F. Corsetti and A. A. Mostofi, *Phys. Rev. B*, 2011, **84**, 035209.

40. P. Rinke, A. Janotti, M. Scheffler and C. G. Van de Walle, *Phys. Rev. Lett.*, 2009, **102**, 026402.

41. I. Chatratin, F. P. Sabino, P. Reunchan, S. Limpijumnong, J. B. Varley, C. G. Van de Walle and A. Janotti, *Phys. Rev. Mater.*, 2019, **3**, 074604.

42. S. A. Lee, S. Choi, C. Kim, J. W. Yang, S. Y. Kim and H. W. Jang, *ACS Mater. Lett.*, 2020, **2**, 107-126.

43. J. Noffsinger, E. Kioupakis, C. G. Van de Walle, S. G. Louie and M. L. Cohen, *Phys. Rev. Lett.*, 2012, **108**, 167402.

44. A. Jena, C.-J. Chen, H. Chang, S.-F. Hu and R.-S. Liu, *J. Mater. Chem. A*, 2021, **9**, 3767-3785.

45. E. C. Garnett and P. Yang, *J. Am. Chem. Soc.*, 2008, **130**, 9224-9225.

46. M. D. Kelzenberg, S. W. Boettcher, J. A. Petykiewicz, D. B. Turner-Evans, M. C. Putnam, E. L. Warren, J. M. Spurgeon, R. M. Briggs, N. S. Lewis and H. A. Atwater, *Nat. Mater.*, 2010, **9**, 239-244.

47. H. Zhang, Q. Ding, D. He, H. Liu, W. Liu, Z. Li, B. Yang, X. Zhang, L. Lei and S. Jin, *Energy Environ. Sci.*, 2016, **9**, 3113-3119.

48. C.-K. Ku, P.-H. Wu, C.-C. Chung, C.-C. Chen, K.-J. Tsai, H.-M. Chen, Y.-C. Chang, C.-H. Chuang, C.-Y. Wei, C.-Y. Wen, T.-Y. Lin, H.-L. Chen, Y.-S. Wang, Z.-Y. Lee, J.-R. Chang, C.-W. Luo, D.-Y. Wang, B. J. Hwang and C.-W. Chen, *Adv. Energy Mater.*, 2019, **9**, 1901022.

49. W. Vijselaar, R. M. Tiggelaar, H. Gardeniers and J. Huskens, *ACS Energy Lett.*, 2018, **3**, 1086-1092.

50. Y. Yu, Z. Zhang, X. Yin, A. Kvit, Q. Liao, Z. Kang, X. Yan, Y. Zhang and X. Wang, *Nat. Energy*, 2017, **2**, 17045.

51. I. Oh, J. Kye and S. Hwang, *Nano Letters*, 2012, **12**, 298-302.

52. S. J. Wang, T. Wang, B. Liu, H. M. Li, S. J. Feng and J. L. Gong, *Natl. Sci. Rev.*, 2021, **8**, nwaa293.

53. R. Elbersen, W. Vijselaar, R. M. Tiggelaar, H. Gardeniers and J. Huskens, *Adv. Energy Mater.*, 2016, **6**, 1501728.

54. R. Elbersen, R. M. Tiggelaar, A. Milbrat, G. Mul, H. Gardeniers and J. Huskens, *Adv. Energy Mater.*, 2015, **5**, 1401745.

55. W. Vijselaar, P. Westerik, J. Veerbeek, R. M. Tiggelaar, E. Berenschot, N. R. Tas, H. Gardeniers and J. Huskens, *Nat. Energy*, 2018, **3**, 185-192.

56. Z. Huang, N. Geyer, P. Werner, J. de Boor and U. Gösele, *Adv. Mater.*, 2011, **23**, 285-308.

57. X. Li, *Curr. Opin. Solid State Mater. Sci.*, 2012, **16**, 71-81.

58. J. Oh, T. G. Deutsch, H.-C. Yuan and H. M. Branz, *Energy Environ. Sci.*, 2011, **4**, 1690-1694.

59. S. W. Boettcher, J. M. Spurgeon, M. C. Putnam, E. L. Warren, D. B. Turner-Evans, M. D. Kelzenberg, J. R. Maiolo, H. A. Atwater and N. S. Lewis, *Science*, 2010, **327**, 185-187.

60. S. W. Boettcher, E. L. Warren, M. C. Putnam, E. A. Santori, D. Turner-Evans, M. D. Kelzenberg, M. G. Walter, J. R. McKone, B. S. Brunschwig, H. A. Atwater and N. S. Lewis, *J. Am. Chem. Soc.*, 2011, **133**, 1216-1219.

61. M. R. Shaner, S. Hu, K. Sun and N. S. Lewis, *Energy Environ. Sci.*, 2015, **8**, 203-207.

62. J. R. McKone, E. L. Warren, M. J. Bierman, S. W. Boettcher, B. S. Brunschwig, N. S. Lewis and H. B. Gray, *Energy Environ. Sci.*, 2011, **4**, 3573-3583.

63. M. R. Shaner, J. R. McKone, H. B. Gray and N. S. Lewis, *Energy Environ. Sci.*, 2015, **8**, 2977-2984.

64. E. L. Warren, J. R. McKone, H. A. Atwater, H. B. Gray and N. S. Lewis, *Energy Environ. Sci.*, 2012, **5**, 9653-9661.

65. H. A. Atwater and A. Polman, *Nat. Mater.*, 2010, **9**, 205-213.

66. S. C. Warren and E. Thimsen, *Energy Environ. Sci.*, 2012, **5**, 5133-5146.

67. M. Ali, F. Zhou, K. Chen, C. Kotzur, C. Xiao, L. Bourgeois, X. Zhang and D. R. MacFarlane, *Nat. Commun.*, 2016, **7**, 11335.

68. D. M. Andoshe, S. Choi, Y.-S. Shim, S. H. Lee, Y. Kim, C. W. Moon, D. H. Kim, S. Y. Lee, T. Kim, H. K. Park, M. G. Lee, J.-M. Jeon, K. T. Nam, M. Kim, J. K. Kim, J. Oh and H. W. Jang, *J. Mater. Chem. A*, 2016, **4**, 9477-9485.

69. B. Shan, S. Vanka, T.-T. Li, L. Troian-Gautier, M. K. Brennaman, Z. Mi and T. J. Meyer, *Nat. Energy*, 2019, **4**, 290-299.

70. M. F. Weber and M. J. Dignam, *Int. J. Hydrogen Energy*, 1986, **11**, 225-232.

71. K. T. Fountaine, H. J. Lewerenz and H. A. Atwater, *Nat. Commun.*, 2016, **7**, 13706.

72. L. C. Seitz, Z. Chen, A. J. Forman, B. A. Pinaud, J. D. Benck and T. F. Jaramillo, *ChemSusChem*, 2014, **7**, 1372-1385.

73. J. Liu, H. Zhao, Z. Wang, T. Hannappel, U. I. Kramm, B. J. M. Etzold and Y. Lei, *Sol. RRL*, 2022, **6**, 2200181.

74. P. Chakthranont, T. R. Hellstern, J. M. McEnaney and T. F. Jaramillo, *Adv. Energy Mater.*, 2017, **7**, 1701515.

75. G. Fiori, F. Bonaccorso, G. Iannaccone, T. Palacios, D. Neumaier, A. Seabaugh, S. K. Banerjee and L. Colombo, *Nat. Nanotechnol.*,

2014, **9**, 768-779.

76. M. Faraji, M. Yousefi, S. Yousefzadeh, M. Zirak, N. Naseri, T. H. Jeon, W. Choi and A. Z. Moshfegh, *Energy Environ. Sci.*, 2019, **12**, 59-95.

77. D. Deng, K. S. Novoselov, Q. Fu, N. Zheng, Z. Tian and X. Bao, *Nat. Nanotechnol.*, 2016, **11**, 218-230.

78. C. Li, Q. Cao, F. Wang, Y. Xiao, Y. Li, J.-J. Delaunay and H. Zhu, *Chem. Soc. Rev.*, 2018, **47**, 4981-5037.

79. S. E. Jun, J. K. Lee and H. W. Jang, *Energy Adv.*, 2023, **2**, 34-53.

80. K. C. Kwon, S. Choi, K. Hong, C. W. Moon, Y.-S. Shim, D. H. Kim, T. Kim, W. Sohn, J.-M. Jeon, C.-H. Lee, K. T. Nam, S. Han, S. Y. Kim and H. W. Jang, *Energy Environ. Sci.*, 2016, **9**, 2240-2248.

81. F. Tian, Z. Pang, S. Hu, X. Zhang, F. Wang, W. Nie, X. Xia, G. Li, H.-Y. Hsu, Q. Xu, X. Zou, L. Ji and X. Lu, *Research*, 2023, **6**, 0142.

82. X. Liang, S. Bai, X. Wang, X. Dai, F. Gao, B. Sun, Z. Ning, Z. Ye and Y. Jin, *Chem. Soc. Rev.*, 2017, **46**, 1730-1759.

83. M. A. Gaikwad, U. P. Suryawanshi, U. V. Ghorpade, J. S. Jang, M. P. Suryawanshi and J. H. Kim, *Small*, 2022, **18**, 2105084.

84. J.-B. Pan, S. Shen, L. Chen, C.-T. Au and S.-F. Yin, *Adv. Funct. Mater.*, 2021, **31**, 2104269.

85. A. Walsh, Y. Yan, M. N. Huda, M. M. Al-Jassim and S.-H. Wei, *Chem. Mater.*, 2009, **21**, 547-551.

86. M. Ziwritsch, S. Müller, H. Hempel, T. Unold, F. F. Abdi, R. van de Krol, D. Friedrich and R. Eichberger, *ACS Energy Lett.*, 2016, **1**, 888-894.

87. A. J. E. Rettie, H. C. Lee, L. G. Marshall, J.-F. Lin, C. Capan, J. Lindemuth, J. S. McCloy, J. Zhou, A. J. Bard and C. B. Mullins, *J. Am. Chem. Soc.*, 2013, **135**, 11389-11396.

88. J. H. Kim and J. S. Lee, *Adv. Mater.*, 2019, **31**, 1806938.

89. Y. Uemura, D. Kido, A. Koide, Y. Wakisaka, Y. Niwa, S. Nozawa, K. Ichiyanagi, R. Fukaya, S.-i. Adachi, T. Katayama, T. Togashi, S. Owada, M. Yabashi, K. Hatada, A. Iwase, A. Kudo, S. Takakusagi, T. Yokoyama and K. Asakura, *Chem. Commun.*, 2017, **53**, 7314-7317.

90. F. F. Abdi, T. J. Savenije, M. M. May, B. Dam and R. van de Krol, *J. Phys. Chem. Lett.*, 2013, **4**, 2752-2757.

91. K. K. Dey, S. Gahlawat and P. P. Ingole, *J. Mater. Chem. A*, 2019, **7**, 21207-21221.

92. H. Lu, V. Andrei, K. J. Jenkinson, A. Regoutz, N. Li, C. E. Creissen, A. E. H. Wheatley, H. Hao, E. Reisner, D. S. Wright and S. D. Pike, *Adv. Mater.*, 2018, **30**, 1804033.

93. B. Weng, C. R. Grice, J. Ge, T. Poudel, X. Deng and Y. Yan, *Adv. Energy Mater.*, 2018, **8**, 1701655.

94. B. Zhang, X. Huang, Y. Zhang, G. Lu, L. Chou and Y. Bi, *Angew. Chem., Int. Ed.*, 2020, **59**, 18990-18995.

95. Y. Pihosh, I. Turkevych, K. Mawatari, J. Uemura, Y. Kazoe, S. Kosar, K. Makita, T. Sugaya, T. Matsui, D. Fujita, M. Tosa, M. Kondo and T. Kitamori, *Sci. Rep.*, 2015, **5**, 11141.

96. J. W. Yang, I. J. Park, S. A. Lee, M. G. Lee, T. H. Lee, H. Park, C. Kim, J. Park, J. Moon, J. Y. Kim and H. W. Jang, *Appl. Catal., B*, 2021, **293**, 120217.

97. J. Liang, X. Du, C. Gibson, X. W. Du and S. Z. Qiao, *Adv. Mater.*, 2013, **25**, 6226-6231.

98. Y. Yang, S. Niu, D. Han, T. Liu, G. Wang and Y. Li, *Adv. Energy Mater.*, 2017, **7**, 1700555.

99. S. Chen and L.-W. Wang, *Chem. Mater.*, 2012, **24**, 3659-3666.

100. D. Lee, A. Kvit and K.-S. Choi, *Chem. Mater.*, 2018, **30**, 4704-4712.

101. S. R. Sitaaraman, A. Nirmala Grace and R. Sellappan, *RSC Adv.*, 2022, **12**, 31380-31391.

102. S. Bai, H. Chu, X. Xiang, R. Luo, J. He and A. Chen, *Chem. Eng. J.*, 2018, **350**, 148-156.

103. Q. Qin, Q. Cai, W. Hong, C. Jian and W. Liu, *Chem. Eng. J.*, 2020, **402**, 126227.

104. P. Lianos, *Appl. Catal., B*, 2017, **210**, 235-254.

105. Z. Li, W. Luo, M. Zhang, J. Feng and Z. Zou, *Energy Environ. Sci.*, 2013, **6**, 347-370.

106. Y. Lin, G. Yuan, S. Sheehan, S. Zhou and D. Wang, *Energy Environ. Sci.*, 2011, **4**, 4862-4869.

107. J. Li, H. Chen, C. A. Triana and G. R. Patzke, *Angew. Chem., Int. Ed.*, 2021, **60**, 18380-18396.

108. I. S. Cho, H. S. Han, M. Logar, J. Park and X. Zheng, *Adv. Energy Mater.*, 2016, **6**, 1501840.

109. D. Kang, T. W. Kim, S. R. Kubota, A. C. Cardiel, H. G. Cha and K.-S. Choi, *Chem. Rev.*, 2015, **115**, 12839-12887.

110. I. V. Bagal, N. R. Chodankar, M. A. Hassan, A. Waseem, M. A. Johar, D.-H. Kim and S.-W. Ryu, *Int. J. Hydrogen Energy*, 2019, **44**, 21351-21378.

111. C. L. Li, J. F. He, Y. Q. Xiao, Y. B. Li and J. J. Delaunay, *Energy Environ. Sci.*, 2020, **13**, 3269-3306.

112. F. Nandjou and S. Haussener, *ChemSusChem*, 2019, **12**, 1984-1994.

113. A. Paracchino, V. Laporte, K. Sivula, M. Grätzel and E. Thimsen, *Nat. Mater.*, 2011, **10**, 456-461.

114. A. Paracchino, N. Mathews, T. Hisatomi, M. Stefik, S. D. Tilley and M. Grätzel, *Energy Environ. Sci.*, 2012, **5**, 8673-8681.

115. A. Kojima, K. Teshima, Y. Shirai and T. Miyasaka, *J. Am. Chem. Soc.*, 2009, **131**, 6050-6051.

116. J. Jeong, M. Kim, J. Seo, H. Lu, P. Ahlawat, A. Mishra, Y. Yang, M. A. Hope, F. T. Eickemeyer, M. Kim, Y. J. Yoon, I. W. Choi, B. P. Darwich, S. J. Choi, Y. Jo, J. H. Lee, B. Walker, S. M. Zakeeruddin, L. Emsley, U. Rothlisberger, A. Hagfeldt, D. S. Kim, M. Grätzel and J. Y. Kim, *Nature*, 2021, **592**, 381-385.

117. J. J. Yoo, G. Seo, M. R. Chua, T. G. Park, Y. Lu, F. Rotermund, Y.-K. Kim, C. S. Moon, N. J. Jeon, J.-P. Correa-Baena, V. Bulović, S. S. Shin, M. G. Bawendi and J. Seo, *Nature*, 2021, **590**, 587-593.

118. H. Min, D. Y. Lee, J. Kim, G. Kim, K. S. Lee, J. Kim, M. J. Paik, Y. K. Kim, K. S. Kim, M. G. Kim, T. J. Shin and S. Il Seok, *Nature*, 2021, **598**, 444-450.

119. R. T. Wang, A. F. Xu, J. Y. Chen, L. W. Yang, G. Xu, V. Jarvis and J. F. Britten, *J. Phys. Chem. Lett.*, 2019, **10**, 7245-7250.

120. J. Zhao, B. Cai, Z. Luo, Y. Dong, Y. Zhang, H. Xu, B. Hong, Y. Yang, L. Li, W. Zhang and C. Gao, *Sci. Rep.*, 2016, **6**, 21976.

121. H. Wang, X. Wang, H. Zhang, W. Ma, L. Wang and X. Zong, *Nano Energy*, 2020, **71**, 104647.

122. P. Da, M. Cha, L. Sun, Y. Wu, Z.-S. Wang and G. Zheng, *Nano Lett.*, 2015, **15**, 3452-3457.

123. M. Crespo-Quesada, L. M. Pazos-Outón, J. Warnan, M. F. Kuehnel, R. H. Friend and E. Reisner, *Nat. Commun.*, 2016, **7**, 12555.

124. I. S. Kim, M. J. Pellin and A. B. F. Martinson, *ACS Energy Lett.*, 2019, **4**, 293-298.

125. J.-H. Kim, S. Seo, J.-H. Lee, H. Choi, S. Kim, G. Piao, Y. R. Kim, B. Park, J. Lee, Y. Jung, H. Park, S. Lee and K. Lee, *Adv. Funct. Mater.*, 2021, **31**, 2008277.

126. A. Facchetti, *Chem. Mater.*, 2011, **23**, 733-758.

127. J. Song, H. Lee, E. G. Jeong, K. C. Choi and S. Yoo, *Adv. Mater.*, 2020, **32**, 1907539.

128. D. Yang and D. Ma, *Adv. Opt. Mater.*, 2019, **7**, 1800522.

129. H.-H. Cho, L. Yao, J.-H. Yum, Y. Liu, F. Boudoire, R. A. Wells, N. Guijarro, A. Sekar and K. Sivula, *Nat. Catal.*, 2021, **4**, 431-438.

130. L. Lu, T. Zheng, Q. Wu, A. M. Schneider, D. Zhao and L. Yu, *Chem. Rev.*, 2015, **115**, 12666-12731.

131. X. Wang, K. Maeda, A. Thomas, K. Takanabe, G. Xin, J. M.

Carlsson, K. Domen and M. Antonietti, *Nat. Mater.*, 2009, **8**, 76-80.

132. S. Bi, C. Yang, W. Zhang, J. Xu, L. Liu, D. Wu, X. Wang, Y. Han, Q. Liang and F. Zhang, *Nat. Commun.*, 2019, **10**, 2467.

133. N. Karjule, J. Barrio, L. Xing, M. Volokh and M. Shalom, *Nano Lett.*, 2020, **20**, 4618-4624.

134. Q. Wang, J. Sun and D. Wei, *Chin. J. Chem.*, 2022, **40**, 1359-1385.

135. H. Wang, Z. Zeng, P. Xu, L. Li, G. Zeng, R. Xiao, Z. Tang, D. Huang, L. Tang, C. Lai, D. Jiang, Y. Liu, H. Yi, L. Qin, S. Ye, X. Ren and W. Tang, *Chem. Soc. Rev.*, 2019, **48**, 488-516.

136. C. Ros, T. Andreu and J. R. Morante, *J. Mater. Chem. A*, 2020, **8**, 10625-10669.

137. R. C. Kainthla, B. Zelenay and J. O. M. Bockris, *J. Electrochem. Soc.*, 1986, **133**, 248-253.

138. J.-X. Jian, M.-M. Yao, J.-X. Liao, M.-H. Zhou, Y.-J. Chen, M.-X. Deng, Y.-M. Huang, C.-P. Liu and Q.-X. Tong, *Catal. Sci. Technol.*, 2022, **12**, 5640-5648

139. J. M. Bolts, A. B. Bocarsly, M. C. Palazzotto, E. G. Walton, N. S. Lewis and M. S. Wrighton, *J. Am. Chem. Soc.*, 1979, **101**, 1378-1385.

140. K. T. Wong and N. S. Lewis, *Acc. Chem. Res.*, 2014, **47**, 3037-3044.

141. B. Fabre, *Chem. Rev.*, 2016, **116**, 4808-4849.

142. Z. Wang, H. Zhu, W. Tu, X. Zhu, Y. Yao, Y. Zhou and Z. Zou, *Adv. Sci*, 2022, **9**, 2103744.

143. A. J. Bard, A. B. Bocarsly, F. R. F. Fan, E. G. Walton and M. S. Wrighton, *J. Am. Chem. Soc.*, 1980, **102**, 3671-3677.

144. J. R. Hemmerling, A. Mathur and S. Linic, *Acc. Chem. Res.*, 2021, **54**, 1992-2002.

145. S. Hu, N. S. Lewis, J. W. Ager, J. Yang, J. R. McKone and N. C. Strandwitz, *J. Phys. Chem. C*, 2015, **119**, 24201-24228.

146. B. Mei, T. Pedersen, P. Malacrida, D. Bae, R. Frydendal, O. Hansen, P. C. K. Vesborg, B. Seger and I. Chorkendorff, *J. Phys. Chem. C*, 2015, **119**, 15019-15027.

147. C. Ros, T. Andreu, M. D. Hernández-Alonso, G. Penelas-Pérez, J. Arbiol and J. R. Morante, *ACS Appl. Mater. Interfaces*, 2017, **9**, 17932-17941.

148. A. G. Scheuermann and P. C. McIntyre, *J. Phys. Chem. Lett.*, 2016, **7**, 2867-2878.

149. Q. Cai, W. Hong, C. Jian, J. Li and W. Liu, *ACS Catal.*, 2018, **8**, 9238-9244.

150. J. Quinn, J. Hemmerling and S. Linic, *ACS Catal.*, 2018, **8**, 8545-8552.

151. D. Zhang, W. Liang, A. Sharma, J. D. Butson, A. G. Saraswathyvilasam, F. J. Beck, K. R. Catchpole and S. Karuturi, *Appl. Phys. Lett.*, 2021, **119**, 193901.

152. I. A. Digdaya, G. W. P. Adhyaksa, B. J. Trzesniewski, E. C. Garnett and W. A. Smith, *Nat. Commun.*, 2017, **8**.

153. C. Li, T. Hisatomi, O. Watanabe, M. Nakabayashi, N. Shibata, K. Domen and J.-J. Delaunay, *Energy Environ. Sci.*, 2015, **8**, 1493-1500.

154. L. Steier, I. Herraiz-Cardona, S. Gimenez, F. Fabregat-Santiago, J. Bisquert, S. D. Tilley and M. Grätzel, *Adv. Funct. Mater.*, 2014, **24**, 7681-7688.

155. R. Noufi, A. J. Frank and A. J. Nozik, *J. Am. Chem. Soc.*, 1981, **103**, 1849-1850.

156. R. Noufi, A. J. Nozik, J. White and L. F. Warren, *J. Electrochem. Soc.*, 1982, **129**, 2261-2265.

157. G. Horowitz and F. Garnier, *J. Electrochem. Soc.*, 1985, **132**, 634-637.

158. M. J. Sailor, F. L. Klavetter, R. H. Grubbs and N. S. Lewis, *Nature*, 1990, **346**, 155-157.

159. C. Yu, M. Cao, Z. Dong, K. Li, C. Yu, J. Wang and L. Jiang, *Adv. Funct. Mater.*, 2016, **26**, 6830-6835.

160. P. Zhang, J. Zhang, Z. Xue, J. Wang and L. Jiang, *Mater. Horiz.*, 2017, **4**, 665-672.

161. G. Liu, W. S. Y. Wong, M. Kraft, J. W. Ager, D. Vollmer and R. Xu, *Chem. Soc. Rev.*, 2021, **50**, 10674-10699.

162. B. Wu, T. Wang, B. Liu, H. Li, Y. Wang, S. Wang, L. Zhang, S. Jiang, C. Pei and J. Gong, *Nat. Commun.*, 2022, **13**, 4460.

163. H. C. Rojas, S. Bellani, F. Fumagalli, G. Tullii, S. Leonardi, M. T. Mayer, M. Schreier, M. Grätzel, G. Lanzani, F. Di Fonzo and M. R. Antognazza, *Energy Environ. Sci.*, 2016, **9**, 3710-3723.

164. J. Tan, B. Kang, K. Kim, D. Kang, H. Lee, S. Ma, G. Jang, H. Lee and J. Moon, *Nat. Energy*, 2022, **7**, 537-547.

165. B. Kang, J. Tan, K. Kim, D. Kang, H. Lee, S. Ma, Y. S. Park, J. Yun, S. Lee, C. U. Lee, G. Jang, J. Lee, J. Moon and H. Lee, *Nat. Commun.*, 2024, **15**, 1495.

166. D. Jeon, J. Park, C. Shin, H. Kim, J.-W. Jang, D. W. Lee and J. Ryu, *Sci. Adv.*, **6**, eaaz3944.

167. R. Wick-Joliat, T. Musso, R. R. Prabhakar, J. Löckinger, S. Siol, W. Cui, L. Sévery, T. Moehl, J. Suh, J. Hutter, M. Iannuzzi and S. D. Tilley, *Energy Environ. Sci.*, 2019, **12**, 1901-1909.

168. W. Siripala, A. Ivanovskaya, T. F. Jaramillo, S.-H. Baeck and E. W. McFarland, *Sol. Energy Mater. Sol. Cells*, 2003, **77**, 229-237.

169. J. Park, W. Yang, Y. Oh, J. Tan, H. Lee, R. Boppella and J. Moon, *ACS Energy Lett.*, 2019, **4**, 517-526.

170. A. G. Scheuermann, J. P. Lawrence, K. W. Kemp, T. Ito, A. Walsh, C. E. D. Chidsey, P. K. Hurley and P. C. McIntyre, *Nat. Mater.*, 2016, **15**, 99-105.

171. J. Cheng, L. Wu and J. Luo, *Nat. Commun.*, 2023, **14**, 7228.

172. B. Liu, S. Feng, L. Yang, C. Li, Z. Luo, T. Wang and J. Gong, *Energy Environ. Sci.*, 2020, **13**, 221-228.

173. B. Liu, S. Wang, S. Feng, H. Li, L. Yang, T. Wang and J. Gong, *Adv. Funct. Mater.*, 2021, **31**, 2007222.

174. H. J. Fu, P. Buabthong, Z. P. Ifkovits, W. Yu, B. S. Brunschwig and N. S. Lewis, *Energy Environ. Sci.*, 2022, **15**, 334-345.

175. Y. Li, X. Zhong, K. Luo and Z. Shao, *J. Mater. Chem. A*, 2019, **7**, 15593-15598.

176. R. Gottesman, A. Song, I. Levine, M. Krause, A. T. M. N. Islam, D. Abou-Ras, T. Dittrich, R. van de Krol and A. Chemseddine, *Adv. Funct. Mater.*, 2020, **30**, 1910832.

177. R. Wang, X. Li, L. Wang, X. Zhao, G. Yang, A. Li, C. Wu, Q. Shen, Y. Zhou and Z. Zou, *Nanoscale*, 2018, **10**, 19621-19627.

178. D. Zhang, H. Li, A. Riaz, A. Sharma, W. Liang, Y. Wang, H. Chen, K. Vora, D. Yan, Z. Su, A. Tricoli, C. Zhao, F. J. Beck, K. Reuter, K. Catchpole and S. Karuturi, *Energy Environ. Sci.*, 2022, **15**, 185-195.

179. B. Seger, T. Pedersen, A. B. Laursen, P. C. K. Vesborg, O. Hansen and I. Chorkendorff, *J. Am. Chem. Soc.*, 2013, **135**, 1057-1064.

180. S. M. Thalluri, L. C. Bai, C. C. Lv, Z. P. Huang, X. L. Hu and L. F. Liu, *Adv. Sci*, 2020, **7**.

181. M. J. Tsai, A. L. Fahrenbruch and R. H. Bube, *J. Appl. Phys.*, 2008, **51**, 2696-2705.

182. C. U. Maier, M. Specht and G. Bilger, *Int. J. Hydrogen Energy*, 1996, **21**, 859-864.

183. D. Bae, S. Shayestehaminzadeh, E. B. Thorsteinsson, T. Pedersen, O. Hansen, B. Seger, P. C. K. Vesborg, S. Ólafsson and I. Chorkendorff, *Sol. Energy Mater. Sol. Cells*, 2016, **144**, 758-765.

184. K. Sarakinos, J. Alami and S. Konstantinidis, *Surf. Coat. Technol.*, 2010, **204**, 1661-1684.

185. K. Jeong, P. R. Deshmukh, J. Park, Y. Sohn and W. G. Shin, *ACS Sustainable Chem. Eng.*, 2018, **6**, 6518-6526.

186. Z. Li and Z. Zhang, *Nano Research*, 2018, **11**, 1530-1540.

187. Y. Li, J.-G. Wang, Y. Fan, H. Sun, W. Hua, H. Liu and B. Wei, *Appl. Catal., B*, 2019, **246**, 21-29.

188. T. Kääriäinen, D. Cameron, M.-L. Kääriäinen and A. Sherman, *Atomic layer deposition: principles, characteristics, and nanotechnology applications*, John Wiley & Sons, New York, 2013.

189. S. M. George, *Chem. Rev.*, 2010, **110**, 111-131.

190. S. Swaminathan, Y. Oshima, M. A. Kelly and P. C. McIntyre, *Appl. Phys. Lett.*, 2009, **95**.

191. W. A. Smith, I. D. Sharp, N. C. Strandwitz and J. Bisquert, *Energy Environ. Sci.*, 2015, **8**, 2851-2862.

192. A. Kudo and Y. Miseki, *Chem. Soc. Rev.*, 2009, **38**, 253-278.

193. X. Shen, T. Zhao, H. Su, M. Yang, J. Chen, Y. Liu, R. Yanagi, D. Solanki and S. Hu, *Adv. Energy Mater.*, 2022, **12**, 2201314.

194. C. Zhang, Y. Li, H. Li, Q. Zhang and J. Lu, *J. Mater. Chem. C*, 2021, **9**, 374-394.

195. A. Azarpira, T. Schedel-Niedrig, H. J. Lewerenz and M. Lublow, *Adv. Energy Mater.*, 2016, **6**, 1502314.

196. X. Zou, L. Ji, J. Ge, D. R. Sadoway, E. T. Yu and A. J. Bard, *Nat. Commun.*, 2019, **10**, 5772.

197. M. Crespo-Quesada and E. Reisner, *Energy Environ. Sci.*, 2017, **10**, 1116-1127.

198. N. Li, P. D. Matthews, H.-K. Luo and D. S. Wright, *Chem. Commun.*, 2016, **52**, 11180-11190.

199. Y.-H. Lai, D. W. Palm and E. Reisner, *Adv. Energy Mater.*, 2015, **5**, 1501668.

200. N. S. Lewis, *Inorg. Chem.*, 2005, **44**, 6900-6911.

201. R. Tang, S. Zhou, Z. Zhang, R. Zheng and J. Huang, *Adv. Mater.*, 2021, **33**, 2005389.

202. F. Li, L. Cheng, J. Fan and Q. Xiang, *J. Mater. Chem. A*, 2021, **9**, 23765-23782.

203. A. Kubacka, M. Fernández-García and G. Colón, *Chem. Rev.*, 2012, **112**, 1555-1614.

204. D. Wang, R. Li, J. Zhu, J. Shi, J. Han, X. Zong and C. Li, *J. Phys. Chem. C*, 2012, **116**, 5082-5089.

205. Y. Ma, F. Le Formal, A. Kafizas, S. R. Pendlebury and J. R. Durrant, *J. Mater. Chem. A*, 2015, **3**, 20649-20657.

206. M. Barroso, A. J. Cowan, S. R. Pendlebury, M. Grätzel, D. R. Klug and J. R. Durrant, *J. Am. Chem. Soc.*, 2011, **133**, 14868-14871.

207. Z. W. Seh, J. Kibsgaard, C. F. Dickens, I. Chorkendorff, J. K. Nørskov and T. F. Jaramillo, *Science*, 2017, **355**, 6321, DOI: 10.1126/science.aad4998.

208. M. G. Walter, E. L. Warren, J. R. McKone, S. W. Boettcher, Q. Mi, E. A. Santori and N. S. Lewis, *Chem. Rev.*, 2010, **110**, 6446-6473.

209. M. Fang, G. Dong, R. Wei and J. C. Ho, *Adv. Energy Mater.*, 2017, **7**, 1700559.

210. C. G. Morales-Guio, L.-A. Stern and X. Hu, *Chem. Soc. Rev.*, 2014, **43**, 6555-6569.

211. J. K. Nørskov, T. Bligaard, A. Logadottir, J. R. Kitchin, J. G. Chen, S. Pandelov and U. Stimming, *J. Electrochem. Soc.*, 2005, **152**, J23.

212. M. G. Kast, L. J. Enman, N. J. Gurnon, A. Nadarajah and S. W. Boettcher, *ACS Appl. Mater. Interfaces*, 2014, **6**, 22830-22837.

213. M. H. Lee, K. Takei, J. Zhang, R. Kapadia, M. Zheng, Y.-Z. Chen, J. Nah, T. S. Matthews, Y.-L. Chueh, J. W. Ager and A. Javey, *Angew. Chem., Int. Ed.*, 2012, **51**, 10760-10764.

214. J. Y. Zheng, Y. H. Lyu, R. L. Wang, C. Xie, H. J. Zhou, S. P. Jiang and S. Y. Wang, *Nat. Commun.*, 2018, **9**.

215. N. P. Dasgupta, C. Liu, S. Andrews, F. B. Prinz and P. Yang, *J. Am. Chem. Soc.*, 2013, **135**, 12932-12935.

216. D. Li, J. Shi and C. Li, *Small*, 2018, **14**, 1704179.

217. H. Sun, Z. Yan, F. Liu, W. Xu, F. Cheng and J. Chen, *Adv. Mater.*, 2020, **32**, 1806326.

218. I. A. Raj and K. I. Vasu, *J. Appl. Electrochem.*, 1990, **20**, 32-38.

219. J. G. Highfield, E. Claude and K. Oguro, *Electrochim. Acta*, 1999, **44**, 2805-2814.

220. Y. Lin, C. Battaglia, M. Boccard, M. Hettick, Z. Yu, C. Ballif, J. W. Ager and A. Javey, *Nano Lett.*, 2013, **13**, 5615-5618.

221. R. Subbaraman, D. Tripkovic, D. Strmcnik, K.-C. Chang, M. Uchimura, A. P. Paulikas, V. Stamenkovic and N. M. Markovic, *Science*, 2011, **334**, 1256-1260.

222. M. Zeng and Y. Li, *J. Mater. Chem. A*, 2015, **3**, 14942-14962.

223. A. Govind Rajan, J. M. P. Martirez and E. A. Carter, *ACS Catal.*, 2020, **10**, 11177-11234.

224. I. A. Digdaya, P. P. Rodriguez, M. Ma, G. W. P. Adhyaksa, E. C. Garnett, A. H. M. Smets and W. A. Smith, *J. Mater. Chem. A*, 2016, **4**, 6842-6852.

225. B. Hinnemann, P. G. Moses, J. Bonde, K. P. Jørgensen, J. H. Nielsen, S. Horch, I. Chorkendorff and J. K. Nørskov, *J. Am. Chem. Soc.*, 2005, **127**, 5308-5309.

226. F. Jaramillo Thomas, P. Jørgensen Kristina, J. Bonde, H. Nielsen Jane, S. Horch and I. Chorkendorff, *Science*, 2007, **317**, 100-102.

227. C. G. Morales-Guio, S. D. Tilley, H. Vrubel, M. Grätzel and X. Hu, *Nat. Commun.*, 2014, **5**, 3059.

228. D. W. Shaffer, Y. Xie and J. J. Concepcion, *Chem. Soc. Rev.*, 2017, **46**, 6170-6193.

229. J. H. Montoya, L. C. Seitz, P. Chakthranont, A. Vojvodic, T. F. Jaramillo and J. K. Nørskov, *Nat. Mater.*, 2017, **16**, 70-81.

230. Y.-C. Zhang, C. Han, J. Gao, L. Pan, J. Wu, X.-D. Zhu and J.-J. Zou, *ACS Catal.*, 2021, **11**, 12485-12509.

231. I. C. Man, H.-Y. Su, F. Calle-Vallejo, H. A. Hansen, J. I. Martínez, N. G. Inoglu, J. Kitchin, T. F. Jaramillo, J. K. Nørskov and J. Rossmeisl, *ChemCatChem*, 2011, **3**, 1159-1165.

232. X.-P. Zhang, A. Chandra, Y.-M. Lee, R. Cao, K. Ray and W. Nam, *Chem. Soc. Rev.*, 2021, **50**, 4804-4811.

233. O. L. Hendricks, A. G. Scheuermann, M. Schmidt, P. K. Hurley, P. C. McIntyre and C. E. D. Chidsey, *ACS Appl. Mater. Interfaces*, 2016, **8**, 23763-23773.

234. O. L. Hendricks, R. Tang-Kong, A. S. Babadi, P. C. McIntyre and C. E. D. Chidsey, *Chem. Mater.*, 2019, **31**, 90-100.

235. Z. B. Luo, B. Liu, H. M. Li, X. X. Chang, W. J. Zhu, T. Wang and J. L. Gong, *Small Methods*, 2019, **3**.

236. G. Loget, *Curr. Opin. Colloid Interface Sci.*, 2019, **39**, 40-50.

237. K. Oh, C. Mériadec, B. Lassalle-Kaiser, V. Dorcet, B. Fabre, S. Ababou-Girard, L. Joanny, F. Gouttefangeas and G. Loget, *Energy Environ. Sci.*, 2018, **11**, 2590-2599.

238. S. A. Lee, T. H. Lee, C. Kim, M. G. Lee, M.-J. Choi, H. Park, S. Choi, J. Oh and H. W. Jang, *ACS Catal.*, 2018, **8**, 7261-7269.

239. G. Loget, C. Mériadec, V. Dorcet, B. Fabre, A. Vacher, S. Fryars and S. Ababou-Girard, *Nat. Commun.*, 2019, **10**, 3522.

240. X. Yu, P. Yang, S. Chen, M. Zhang and G. Shi, *Adv. Energy Mater.*, 2017, **7**, 1601805.

241. C. L. Li, M. R. Huang, Y. J. Zhong, L. Zhang, Y. Q. Xiao and H. W. Zhu, *Chem. Mater.*, 2019, **31**, 171-178.

242. B. Guo, A. Batool, G. Xie, R. Boddula, L. Tian, S. U. Jan and J. R. Gong, *Nano Lett.*, 2018, **18**, 1516-1521.

243. S. A. Lee, J. W. Yang, T. H. Lee, I. J. Park, C. Kim, S. H. Hong, H. Lee, S. Choi, J. Moon, S. Y. Kim, J. Y. Kim and H. W. Jang, *Appl. Catal., B*, 2022, **317**, 121765.

244. D. González-Flores, I. Sánchez, I. Zaharieva, K. Klingan, J. Heidkamp, P. Chernev, P. W. Menezes, M. Driess, H. Dau and M. L. Montero, *Angew. Chem., Int. Ed.*, 2015, **54**, 2472-2476.

245. J. Yang, J. K. Cooper, F. M. Toma, Karl A. Walczak, M. Favaro, Jeffrey W. Beeman, Lucas H. Hess, C. Wang, C. Zhu, S. Gul, J.

Yano, C. Kisielowski, A. Schwartzberg and Ian D. Sharp, *Nat. Mater.*, 2017, **16**, 335-341.

246. E. A. Reyes Cruz, D. Nishiori, B. L. Wadsworth, N. P. Nguyen, L. K. Hensleigh, D. Khusnutdinova, A. M. Beiler and G. F. Moore, *Chem. Rev.*, 2022, **122**, 16051-16109.

247. M. Wang, Y. Yang, J. Shen, J. Jiang and L. Sun, *Sustainable Energy Fuels*, 2017, **1**, 1641-1663.

248. K. E. Dalle, J. Warnan, J. J. Leung, B. Reuillard, I. S. Karmel and E. Reisner, *Chem. Rev.*, 2019, **119**, 2752-2875.

249. F. J. Niu, D. G. Wang, F. Li, Y. M. Liu, S. H. Shen and T. J. Meyer, *Adv. Energy Mater.*, 2020, **10**, 1900399.

250. J. Seo, R. T. Pekarek and M. J. Rose, *Chem. Commun.*, 2015, **51**, 13264-13267.

251. J. Gu, Y. Yan, J. L. Young, K. X. Steirer, N. R. Neale and J. A. Turner, *Nat. Mater.*, 2016, **15**, 456-460.

252. J. J. Leung, J. Warnan, D. H. Nam, J. Z. Zhang, J. Willkomm and E. Reisner, *Chem. Sci.*, 2017, **8**, 5172-5180.

253. B. Shan, M. K. Brennaman, L. Troian-Gautier, Y. Liu, A. Nayak, C. M. Klug, T.-T. Li, R. M. Bullock and T. J. Meyer, *J. Am. Chem. Soc.*, 2019, **141**, 10390-10398.

254. N. Kornienko, J. Z. Zhang, K. K. Sakimoto, P. Yang and E. Reisner, *Nat. Nanotechnol.*, 2018, **13**, 890-899.

255. A. Wang, J. Li and T. Zhang, *Nat. Rev. Chem.*, 2018, **2**, 65-81.

256. J. Wu, L. Xiong, B. Zhao, M. Liu and L. Huang, *Small Methods*, 2020, **4**, 1900540.

257. X.-F. Yang, A. Wang, B. Qiao, J. Li, J. Liu and T. Zhang, *Acc. Chem. Res.*, 2013, **46**, 1740-1748.

258. D. Liu, X. Wan, T. Kong, W. Han and Y. Xiong, *J. Mater. Chem. A*, 2022, **10**, 5878-5888.

259. C. Cui, M. Heggen, W.-D. Zabka, W. Cui, J. Osterwalder, B. Probst and R. Alberto, *Nat. Commun.*, 2017, **8**, 1341.

260. V. Ramalingam, P. Varadhan, H.-C. Fu, H. Kim, D. Zhang, S. Chen, L. Song, D. Ma, Y. Wang, H. N. Alshareef and J.-H. He, *Adv. Mater.*, 2019, **31**, 1903841.

261. Z. Tian, Y. Da, M. Wang, X. Dou, X. Cui, J. Chen, R. Jiang, S. Xi, B. Cui, Y. Luo, H. Yang, Y. Long, Y. Xiao and W. Chen, *Nat. Commun.*, 2023, **14**, 142.

262. R. Long, Y. Li, Y. Liu, S. Chen, X. Zheng, C. Gao, C. He, N. Chen, Z. Qi, L. Song, J. Jiang, J. Zhu and Y. Xiong, *J. Am. Chem. Soc.*, 2017, **139**, 4486-4492.

263. S. E. Jun, Y.-H. Kim, J. Kim, W. S. Cheon, S. Choi, J. Yang, H. Park, H. Lee, S. H. Park, K. C. Kwon, J. Moon, S.-H. Kim and H. W. Jang, *Nat. Commun.*, 2023, **14**, 609.

264. X. Shen, R. Yanagi, D. Solanki, H. Su, Z. Li, C.-X. Xiang and S. Hu, *Front. Energy Res.*, 2022, **9**, 799776.

265. J. Hemmerling, J. Quinn and S. Linic, *Adv. Energy Mater.*, 2020, **10**, 1903354.

266. I. A. Digdaya, B. J. Trześniewski, G. W. P. Adhyaksa, E. C. Garnett and W. A. Smith, *J. Phys. Chem. C*, 2018, **122**, 5462-5471.

267. S. Zafar, Q. Liu and E. A. Irene, *J. Vac. Sci. Technol., A*, 1995, **13**, 47-53.

268. B. Seger, T. Pedersen, A. B. Laursen, P. C. K. Vesborg, O. Hansen and I. Chorkendorff, *J. Am. Chem. Soc.*, 2013, **135**, 1057-1064.

269. D. Bae, T. Pedersen, B. Seger, M. Malizia, A. Kuznetsov, O. Hansen, I. Chorkendorff and P. C. K. Vesborg, *Energy Environ. Sci.*, 2015, **8**, 650-660.

270. R. Woods-Robinson, Y. Han, H. Zhang, T. Ablekim, I. Khan, K. A. Persson and A. Zakutayev, *Chem. Rev.*, 2020, **120**, 4007-4055.

271. M. T. Greiner, M. G. Helander, W.-M. Tang, Z.-B. Wang, J. Qiu and Z.-H. Lu, *Nat. Mater.*, 2012, **11**, 76-81.

272. Z. Wang, P. K. Nayak, J. A. Caraveo-Frescas and H. N. Alshareef, *Adv. Mater.*, 2016, **28**, 3831-3892.

273. G. Campet, C. Puprichitkun and Z. W. Sun, *J. Electroanal. Chem. Interfacial Electrochem.*, 1989, **269**, 435-445.

274. S. Cao, Z. Kang, Y. Yu, J. Du, L. German, J. Li, X. Yan, X. Wang and Y. Zhang, *Adv. Energy Mater.*, 2020, **10**, 1902985.

275. M. Muscetta, R. Andreozzi, L. Clarizia, I. Di Somma and R. Marotta, *Int. J. Hydrogen Energy*, 2020, **45**, 28531-28552.

276. R. E. Brandt, M. Young, H. H. Park, A. Dameron, D. Chua, Y. S. Lee, G. Teeter, R. G. Gordon and T. Buonassisi, *Appl. Phys. Lett.*, 2014, **105**, 263901.

277. P. Dai, W. Li, J. Xie, Y. He, J. Thorne, G. McMahon, J. Zhan and D. Wang, *Angew. Chem., Int. Ed.*, 2014, **53**, 13493-13497.

278. L. Pan, J. H. Kim, M. T. Mayer, M.-K. Son, A. Ummadisingu, J. S. Lee, A. Hagfeldt, J. Luo and M. Grätzel, *Nat. Catal.*, 2018, 1, 412-420.

279. Q. Chen, C. Wang, Y. Li and L. Chen, *J. Am. Chem. Soc.*, 2020, **142**, 18281-18292.

280. H. Ma, H.-L. Yip, F. Huang and A. K.-Y. Jen, 2010, **20**, 1371-1388.

281. J. Yun, J. Tan, Y.-K. Jung, W. Yang, H. Lee, S. Ma, Y. S. Park, C. U. Lee, W. Niu, J. Lee, K. Kim, S. D. Tilley, A. Walsh and J. Moon, *ACS Energy Lett.*, 2022, **7**, 1392-1402.

282. J.-D. Rochaix, *Biochim. Biophys. Acta, Bioenerg.*, 2011, **1807**, 375-383.

283. C. Liu, F. Li, L. Wang, Z. Li, Y. Zhao, Y. Li, W. Li, Z. Zhao, K. Fan, F. Li and L. Sun, *Fundam. Res.*, 2022, DOI: 10.1016/j.fmre.2022.03.013.

284. L. Kornblum, D. P. Fenning, J. Faucher, J. Hwang, A. Boni, M. G. Han, M. D. Morales-Acosta, Y. Zhu, E. I. Altman, M. L. Lee, C. H. Ahn, F. J. Walker and Y. Shao-Horn, *Energy Environ. Sci.*, 2017, **10**, 377-382.

285. K. Sun, F. H. Saadi, M. F. Lichterman, W. G. Hale, H.-P. Wang, X. Zhou, N. T. Plymale, S. T. Omelchenko, J.-H. He, K. M. Papadantonakis, B. S. Brunschwig and N. S. Lewis, *Proc. Natl. Acad. Sci. U. S. A.*, 2015, **112**, 3612-3617.

286. T. Moehl, J. Suh, L. Sévery, R. Wick-Joliat and S. D. Tilley, *ACS Appl. Mater. Interfaces*, 2017, **9**, 43614-43622.

287. M. F. Lichterman, A. I. Carim, M. T. McDowell, S. Hu, H. B. Gray, B. S. Brunschwig and N. S. Lewis, *Energy Environ. Sci.*, 2014, **7**, 3334-3337.

288. E. Verlage, S. Hu, R. Liu, R. J. R. Jones, K. Sun, C. Xiang, N. S. Lewis and H. A. Atwater, *Energy Environ. Sci.*, 2015, **8**, 3166-3172.

289. P. Nunez, M. H. Richter, B. D. Piercy, C. W. Roske, M. Cabán-Acevedo, M. D. Losego, S. J. Konezny, D. J. Fermin, S. Hu, B. S. Brunschwig and N. S. Lewis, *J. Phys. Chem. C*, 2019, **123**, 20116-20129.

290. S. Wendt, P. T. Sprunger, E. Lira, G. K. H. Madsen, Z. Li, J. Ø. Hansen, J. Matthiesen, A. Blekinge-Rasmussen, E. Lægsgaard, B. Hammer and F. Besenbacher, *Science*, 2008, **320**, 1755-1759.

291. S. Hu, M. H. Richter, M. F. Lichterman, J. Beardslee, T. Mayer, B. S. Brunschwig and N. S. Lewis, *J. Phys. Chem. C*, 2016, **120**, 3117-3129.

292. M. F. Lichterman, S. Hu, M. H. Richter, E. J. Crumlin, S. Axnanda, M. Favaro, W. Drisdell, Z. Hussain, T. Mayer, B. S. Brunschwig, N. S. Lewis, Z. Liu and H.-J. Lewerenz, *Energy Environ. Sci.*, 2015, **8**, 2409-2416.

293. M. H. Richter, W.-H. Cheng, E. J. Crumlin, W. S. Drisdell, H. A. Atwater, D. Schmeißer, N. S. Lewis and B. S. Brunschwig, *Chem. Mater.*, 2021, **33**, 1265-1275.

294. M. T. McDowell, M. F. Lichterman, A. I. Carim, R. Liu, S. Hu, B. S. Brunschwig and N. S. Lewis, *ACS Appl. Mater. Interfaces*, 2015, **7**, 15189-15199.

295. C.-H. Chuang, Y.-Y. Lai, C.-H. Hou and Y.-J. Cheng, *ACS Appl.*

Energy Mater., 2020, **3**, 3902-3908.

296. Z. Ni, S. Xu, H. Jiao, H. Gu, C. Fei and J. Huang, 2022, **8**, eabq8345.

297. H. Li, T. Wang, S. Liu, Z. Luo, L. Li, H. Wang, Z.-J. Zhao and J. Gong, *Angew. Chem., Int. Ed.*, 2021, **60**, 4034-4037.

298. G. Siddiqi, Z. Luo, Y. Xie, Z. Pan, Q. Zhu, J. A. Röhr, J. J. Cha and S. Hu, *ACS Appl. Mater. Interfaces*, 2018, **10**, 18805-18815.

299. T. Dullweber and J. Schmidt, *IEEE Journal of Photovoltaics*, 2016, **6**, 1366-1381.

300. D. Seo, J. T. Kim, D.-W. Hwang, D. Y. Kim, S. Y. Lim and T. D. Chung, *ACS Appl. Mater. Interfaces*, 2021, **13**, 46499-46506.

301. P. Kleimann, X. Badel and J. Linnros, *Appl. Phys. Lett.*, 2005, **86**.

302. H. J. Lewerenz, *Electrochim. Acta*, 2011, **56**, 10713-10725.

303. H. J. Lewerenz, A. G. Muñoz, K. Skorupska, T. Stempel, H. W. Klemm, M. Kanis and M. Lublow, *J. Electroanal. Chem.*, 2010, **646**, 85-90.

304. H. J. Lewerenz, M. Aggour, T. Stempel, M. Lublow, J. Grzanna and K. Skorupska, *J. Electroanal. Chem.*, 2008, **619-620**, 137-142.

305. R. Forbes and S. Zukotynski, *J. Electrochem. Soc.*, 1989, **136**, 736.

306. A. Bierhals, A. G. Aberle and R. Hezel, *J. Appl. Phys.*, 1998, **83**, 1371-1378.

307. A. W. Y. Ho and S. R. Wenham, *Prog. Photovoltaics*, 2004, **12**, 297-308.

308. A. W. Y. Ho and S. R. Wenham, *Sol. Energy Mater. Sol. Cells*, 2007, **91**, 1234-1242.

309. S. Oh and J. Oh, *J. Phys. Chem. C*, 2016, **120**, 133-141.

310. M. Lippmaa, S. Kawasaki, R. Takahashi and T. Yamamoto, *MRS Bull.*, 2021, **46**, 142-151.

311. J. Huang, W. Li, H. Yang and J. L. MacManus-Driscoll, *MRS Bull.*, 2021, **46**, 159-167.

312. S. Kawasaki, R. Takahashi, T. Yamamoto, M. Kobayashi, H. Kumigashira, J. Yoshinobu, F. Komori, A. Kudo and M. Lippmaa, *Nat. Commun.*, 2016, **7**, 11818.

313. J. Huang, Z. Qi, L. Li, H. Wang, S. Xue, B. Zhang, X. Zhang and H. Wang, *Nanoscale*, 2018, **10**, 17182-17188.

314. A. Vilanova, P. Dias, T. Lopes and A. Mendes, *Chem. Soc. Rev.*, 2024, **53**, 2388-2434.

315. A. Hankin, F. E. Bedoya-Lora, C. K. Ong, J. C. Alexander, F. Petter and G. H. Kelsall, *Energy Environ. Sci.*, 2017, **10**, 346-360.

316. A. Vilanova, T. Lopes and A. Mendes, *J. Power Sources*, 2018, **398**, 224-232.

317. N. Y. Labrador, X. X. Li, Y. K. Liu, H. Y. Tan, R. Y. Wang, J. T. Koberstein, T. P. Moffat and D. V. Esposito, *Nano Lett.*, 2016, **16**, 6452-6459.

318. W. Gu, T. Ma, S. Ahmed, Y. Zhang and J. Peng, *Energy Convers. Manage.*, 2020, **223**, 113283.

319. A. Cuevas, A. Luque, J. Eguren and J. del Alamo, *Sol. Energy*, 1982, **29**, 419-420.

320. H.-C. Fu, P. Varadhan, C.-H. Lin and J.-H. He, *Nat. Commun.*, 2020, **11**, 3930.

321. T. Yao, R. Chen, J. Li, J. Han, W. Qin, H. Wang, J. Shi, F. Fan and C. Li, *J. Am. Chem. Soc.*, 2016, **138**, 13664-13672.

322. R. R. Hernandez, S. B. Easter, M. L. Murphy-Mariscal, F. T. Maestre, M. Tavassoli, E. B. Allen, C. W. Barrows, J. Belnap, R. Ochoa-Hueso, S. Ravi and M. F. Allen, *Renewable Sustainable Energy Rev.*, 2014, **29**, 766-779.

323. Y. Tang, C. Zhou, W. Wang, Y. Zhao, S. Zhou, J. Fei and H. Cao, *Sol. Energy*, 2013, **95**, 265-270.

324. B. Liu, S. Wang, G. Zhang, Z. Gong, B. Wu, T. Wang and J. Gong, *Chem. Soc. Rev.*, 2023, **52**, 4644-4671.

325. S. Hu, C. Xiang, S. Haussener, A. D. Berger and N. S. Lewis, *Energy Environ. Sci.*, 2013, **6**, 2984-2993.

326. M. Ahmed and I. Dincer, *Int. J. Hydrogen Energy*, 2019, **44**, 2474-2507.

327. C. Moon, F. M. Alves Martinho, G. Jung, J. Koh, A. Assar, S.-W. Nam, S. Canulescu and B. Shin, *J. Mater. Chem. A*, 2023, **11**, 4194-4204.

328. D. G. Nocera, *Acc. Chem. Res.*, 2012, **45**, 767-776.

329. S. Haussener, C. Xiang, J. M. Spurgeon, S. Ardo, N. S. Lewis and A. Z. Weber, *Energy Environ. Sci.*, 2012, **5**, 9922-9935.

330. I. Y. Ahmet, S. Berglund, A. Chemseddine, P. Bogdanoff, R. F. Präg, F. F. Abdi and R. van de Krol, *Adv. Energy Sustainability Res.*, 2020, **1**, 2000037.

331. S. Wang, S. Feng, B. Liu, Z. Gong, T. Wang and J. Gong, *Chem. Sci.*, 2023, **14**, 2192-2199.

332. G. Jung, C. Moon, F. Martinho, Y. Jung, J. Chu, H. Park, A. Hajijafarassar, R. Nielsen, J. Schou, J. Park, P. C. K. Vesborg, O. Hansen, Y. S. Lee, S. Canulescu and B. Shin, *Adv. Energy Mater.*, 2023, **13**, 2301235.

333. J. Newman, *J. Electrochem. Soc.*, 2013, **160**, F309.

334. K. S. Joya, Y. F. Joya, K. Ocakoglu and R. van de Krol, *Angew. Chem., Int. Ed.*, 2013, **52**, 10426-10437.

335. C. Moon, B. Seger, P. C. K. Vesborg, O. Hansen and I. Chorkendorff, *Cell Rep. Phys. Sci.*, 2020, **1**, 100261.

336. G. Yang, W. Yang, H. Gu, Y. Fu, B. Wang, H. Cai, J. Xia, N. Zhang, C. Liang, G. Xing, S. Yang, Y. Chen and W. Huang, *Adv. Mater.*, 2023, **35**, 2300383.

337. V. Andrei, R. L. Z. Hoye, M. Crespo-Quesada, M. Bajada, S. Ahmad, M. De Volder, R. Friend and E. Reisner, *Adv. Energy Mater.*, 2018, **8**, 1801403.

338. J. Park, J. Lee, H. Lee, H. Im, S. Moon, C.-S. Jeong, W. Yang and J. Moon, *Small*, 2023, **19**, 2300174.

339. A. M. K. Fehr, A. Agrawal, F. Mandani, C. L. Conrad, Q. Jiang, S. Y. Park, O. Alley, B. Li, S. Sidhik, I. Metcalf, C. Botello, J. L. Young, J. Even, J. C. Blancon, T. G. Deutsch, K. Zhu, S. Albrecht, F. M. Toma, M. Wong and A. D. Mohite, *Nat. Commun.*, 2023, **14**, 3797.

340. M. Wang, B. Shi, Q. Zhang, X. Li, S. Pan, Y. Zhao and X. Zhang, *Sol. RRL*, 2022, **6**, 2100748.

341. H. Yang, Y. Liu, Y. Ding, F. Li, L. Wang, B. Cai, F. Zhang, T. Liu, G. Boschloo, E. M. J. Johansson and L. Sun, *Nat. Commun.*, 2023, **14**, 5486.

342. Z. Song, C. Li, L. Chen, K. Dolia, S. Fu, N. Sun, Y. Li, K. Wyatt, J. L. Young, T. G. Deutsch and Y. Yan, *ACS Energy Lett.*, 2023, **8**, 2611-2619.

343. B. Seger, I. E. Castelli, P. C. K. Vesborg, K. W. Jacobsen, O. Hansen and I. Chorkendorff, *Energy Environ. Sci.*, 2014, **7**, 2397-2413.

344. C. Wang, S. Yang, X. Chen, T. Wen and H. G. Yang, *J. Mater. Chem. A*, 2017, **5**, 910-913.

345. C. Pornrungroj, V. Andrei, M. Rahaman, C. Uswachoke, H. J. Joyce, D. S. Wright and E. Reisner, *Adv. Funct. Mater.*, 2021, **31**, 2008182.

346. S. Y. Reece, J. A. Hamel, K. Sung, T. D. Jarvi, A. J. Esswein, J. J. H. Pijpers and D. G. Nocera, *Science*, 2011, **334**, 645-648.

347. S. Micera and E. Redolfi Riva, *Nat. Mater.*, 2022, **21**, 614-616.

348. P. Li, J. Zhang, H. Hayashi, J. Yue, W. Li, C. Yang, C. Sun, J. Shi, J. Huberman-Shlaes, N. Hibino and B. Tian, *Nature*, 2024, **626**, 990-998.

349. M. J. Shearer, W. Li, J. G. Foster, M. J. Stolt, R. J. Hamers and S. Jin, *ACS Energy Lett.*, 2019, **4**, 102-109.

350. J. Liang, H. Tan, M. Liu, B. Liu, N. Wang, Q. Zhang, Y. Zhao, A. H. M. Smets, M. Zeman and X. Zhang, *J. Mater. Chem. A*, 2016, **4**, 16841-16848.

351. P. A. Kempler, M. A. Gonzalez, K. M. Papadantonakis and N. S.

Lewis, *ACS Energy Lett.*, 2018, **3**, 612-617.

352. K. T. Butler, D. W. Davies, H. Cartwright, O. Isayev and A. Walsh, *Nature*, 2018, **559**, 547-555.

353. J. Vamathevan, D. Clark, P. Czodrowski, I. Dunham, E. Ferran, G. Lee, B. Li, A. Madabhushi, P. Shah, M. Spitzer and S. Zhao, *Nat. Rev. Drug Discovery*, 2019, **18**, 463-477.

354. M. Zhong, K. Tran, Y. Min, C. Wang, Z. Wang, C.-T. Dinh, P. De Luna, Z. Yu, A. S. Rasouli, P. Brodersen, S. Sun, O. Voznyy, C.-S. Tan, M. Askerka, F. Che, M. Liu, A. Seifitokaldani, Y. Pang, S.-C. Lo, A. Ip, Z. Ulissi and E. H. Sargent, *Nature*, 2020, **581**, 178-183.

355. A. Nandy, C. Duan, M. G. Taylor, F. Liu, A. H. Steeves and H. J. Kulik, *Chem. Rev.*, 2021, **121**, 9927-10000.

356. A. Mahmood and J.-L. Wang, *Energy Environ. Sci.*, 2021, **14**, 90-105.

357. X. Wang, P. Huo, Y. Liu, Y. Xiang, C. Jia and Z. Yan, *Appl. Catal., A*, 2021, **616**, 118073.

358. B. Burger, P. M. Maffettone, V. V. Gusev, C. M. Aitchison, Y. Bai, X. Wang, X. Li, B. M. Alston, B. Li, R. Clowes, N. Rankin, B. Harris, R. S. Sprick and A. I. Cooper, *Nature*, 2020, **583**, 237-241.

359. M. Borgwardt, S. T. Omelchenko, M. Favaro, P. Plate, C. Höhn, D. Abou-Ras, K. Schwarzburg, R. van de Krol, H. A. Atwater, N. S. Lewis, R. Eichberger and D. Friedrich, *Nat. Commun.*, 2019, **10**, 2106.

360. S. Pishgar, S. Gulati, J. M. Strain, Y. Liang, M. C. Mulvehill and J. M. Spurgeon, *Small Methods*, 2021, **5**, 2100322.

361. S. Pishgar, J. M. Strain, S. Gulati, G. Sumanasekera, G. Gupta and J. M. Spurgeon, *J. Mater. Chem. A*, 2019, **7**, 25377-25388.

362. X. Zhang, M. Schwarze, R. Schomäcker, R. van de Krol and F. F. Abdi, *Nat. Commun.*, 2023, **14**, 991.

363. K. Obata, M. Schwarze, T. A. Thiel, X. Zhang, B. Radhakrishnan, I. Y. Ahmet, R. van de Krol, R. Schomäcker and F. F. Abdi, *Nat. Commun.*, 2023, **14**, 6017.

364. C. R. Lhermitte and K. Sivula, *ACS Catal.*, 2019, **9**, 2007-2017.

365. J.-A. Lin, I. Roh and P. Yang, *J. Am. Chem. Soc.*, 2023, **145**, 12987-12991.

366. 365. S. Bhattacharjee, M. Rahaman, V. Andrei, M. Miller, S. Rodríguez-Jiménez, E. Lam, C. Pornrungroj and E. Reisner, *Nat. Synth.*, 2023, **2**, 182-192.

367. 366. S. Bhattacharjee, S. Linley and E. Reisner, *Nat. Rev. Chem.*, 2024, **8**, 87-105.

368. IEA (2023), Towards hydrogen definitions based on their emissions intensity, IEA, Paris https://www.iea.org/reports/towards-hydrogen-definitions-based-on-their-emissions-intensity, License: CC BY 4.0

369. Hydrogen for net-zero: A critical cost-competitive energy vector, Hydrogen Council and McKinsey, November 2021.

370. S. Ardo, D. Fernandez Rivas, M. A. Modestino, V. Schulze Greiving, F. F. Abdi, E. Alarcon Llado, V. Artero, K. Ayers, C. Battaglia, J.-P. Becker, D. Bederak, A. Berger, F. Buda, E. Chinello, B. Dam, V. Di Palma, T. Edvinsson, K. Fujii, H. Gardeniers, H. Geerlings, S. M. H. Hashemi, S. Haussener, F. Houle, J. Huskens, B. D. James, K. Konrad, A. Kudo, P. P. Kunturu, D. Lohse, B. Mei, E. L. Miller, G. F. Moore, J. Muller, K. L. Orchard, T. E. Rosser, F. H. Saadi, J.-W. Schüttauf, B. Seger, S. W. Sheehan, W. A. Smith, J. Spurgeon, M. H. Tang, R. van de Krol, P. C. K. Vesborg and P. Westerik, *Energy Environ. Sci.*, 2018, **11**, 2768-2783.

371. M. R. Shaner, H. A. Atwater, N. S. Lewis and E. W. McFarland, *Energy Environ. Sci.*, 2016, **9**, 2354-2371.

372. J. L. Young, M. A. Steiner, H. Döscher, R. M. France, J. A. Turner and Todd G. Deutsch, *Nat. Energy* 2017, **2**, 17028.

373. M. M. May, H.-J. Lewerenz, D. Lackner, F. Dimroth and T. Hannappel, *Nat. Commun.*, 2015, **6**, 8286.

374. T. Grube, J. Reul, M. Reuß, S. Calnan, N. Monnerie, R. Schlatmann, C. Sattler, M. Robinius and D. Stolten, *Sustainable Energy Fuels*, 2020, **4**, 5818-5834.

375. A. Landman, H. Dotan, G. E. Shter, M. Wullenkord, A. Houaijia, A. Maljusch, G. S. Grader and A. Rothschild, *Nat. Mater.*, 2017, **16**, 646-651.

376. J. H. Kim, D. Hansora, P. Sharma, J.-W. Jang and J. S. Lee, *Chem. Soc. Rev.*, 2019, **48**, 1908-1971.